Modelling of Gas Transport in Porous Zeolite-Modified Discriminating Gas sensors

Sheena J B Dungey

This thesis is submitted in partial fulfilment of the requirements for the Degree of Doctor of Philosophy

November 2010

University College London
Chemistry Department

I, Sheena Joanna Dungey, confirm that the work presented in this thesis is my own. Where information has been derived from other sources, I confirm that this has been indicated in the thesis.

Abstract

The ability to distinguish effectively between a range of gases in a reliable, repeatable manner is of major interest with both scientific and commercial relevance. Semiconducting metal oxide gas sensors have a long life-span, are inexpensive and are highly sensitive; however, they are generally found to lack a desired level of selectivity. One highly viable approach for enhancing the selective power of such devices is the addition of a *transformation* layer. This will typically be a micro- or meso-porous, solid which will act to transform the analyte gas stream by some means. Here the use of zeolite compounds for this purpose is investigated.

Different theoretical models are used to probe the dependency of the response of a porous metal oxide sensor on the transport properties of gas through the device, including through an additional zeolite layer. Through the use of a force-field based method, shape and size selective adsorption is predicted and used to justify experimental results of zeolite modified sensors, for example, the reduction of response to linear hydrocarbons as the chain-length is increased. However, the limit of such calculations is also realised such that this approach is unlikely to provide an adequate predictive tool for selecting a suitable zeolite for a particular gas sensing task.

Following this, a model based on the method of diffusion eigenstates has been developed to calculate bulk effective diffusivities and rate constants for porous systems representing both the sensor and zeolite porous layers. The effective properties are found to depend strongly on the microstructure, the partitioning between phases and diffusion coefficients of the different phases. The effective parameters are then interpreted in terms of sensor response by solving the one-dimensional diffusion-reaction equation for a simple two-layered macroscopic geometry. The method of finite differences is used to find the concentration profile which generates a response on interaction with an electric field established between two electrodes. The concentration profile and hence the response depends on the balance of diffusion and reaction of the analyte gas within both the sensor and zeolite layers. It is shown how the response can be explored to expose such differences by firstly looking at both the steady state response and response time and also by varying the positioning of the electrodes used to measure the response. Good correlation with experimental response data is demonstrated, supporting the importance of the diffusion-reaction properties modelled to the sensing mechanism, and the potential of developing a predictive tool based on the models presented is discussed.

Acknowledgements

I would firstly like to thank Dr. Dewi. W. Lewis for his supervision over the course of my PhD and for giving me the opportunity to participate in this research project. I have greatly valued his input and support of my work and his guidance throughout.

I have also greatly appreciated working with fellow PhD student Ayo Afonja and consider the opportunity to work closely with colleagues of different disciplines as a highly valuable aspect of this project.

My thanks are also given to Dr. Russell Binnions and Prof. Ivan Parkins for their help and guidance and to Prof. David. E. Williams for his direction and enthusiasm of the work I have carried out as well as his great insight generally into the project.

Finally I would like to thank dearly my family and friends for their support throughout.

Table of Contents

1. Introduction to solid state gas sensors and the use of zeolite layers for enhancing selectivity

1.1 Introduction

1.2 Modelling the sensor system

1.2.1 Primary considerations

1.2.2 Gas-metal oxide interaction models – relating gas concentration to local conductivity

1.2.3 Conductivity models – relating sensor response to local conductivity

1.2.4 Concentration variation

1.2.5 Sensor arrays

1.3 Zeolites and their application to gas sensing:

1.3.1 An overview

1.3.2 Zeolites for gas sensing

1.3.3 Transport through the zeolite layer

1.4 Summary

1.5 Thesis overview

2. Adsorption of gases in zeolites.

2.1 Introduction

2.2 Computational models for gas adsorption in zeolites

2.3 Force-field simulation details

2.3.1 Overview

2.3.2 Structure preparation

2.3.3 Infinite dilution calculations

2.3.4 Higher loadings

2.4 Results of descriptor and force-field calculations

2.4.1 Zeolite and sorbate classifications

2.4.2 Binding Energies – infinite dilution

2.4.3 Higher loadings

2.4.4 Summary of force-field results

2.5 DFT Calculations

2.5.1 Simulation details

2.5.2 Results of DFT calculations
2.5.3 Summary of DFT results
2.6 Comparison with experimental data.
2.6.1 Linear hydrocarbons
2.6.2 CO, NO_2 and ethanol
2.6.3 Isopropanol and ethanol
2.7 Conclusions

3. Diffusion and reaction in porous media.
3.1 Introduction
3.2 Diffusion in zeolites
3.2.1 Introduction to diffusion theory
3.2.2 Methods for studying diffusion in zeolites
3.3 Overview: A model for diffusion and reaction in composite media
3.3.1 Key aspects of the Bergman-Dunn model
3.3.2 Finding diffusion eigenstates
3.4 Theory
3.3.1 The diffusion equation in terms of chemical potential
3.3.2 Use of a periodic microstructure
3.3.3 The eigenvalue equation
3.3.4 Extension of model to include interface reaction
3.5 Computational Procedure
3.5.1 System of two penetrable phases with phase-dependent reactions
3.5.2 System of impenetrable obstacles with a surface reaction
3.6 Results
3.6.1 Modelling the sensor layer
3.6.2 Modelling the zeolite layer
3.7 Conclusions

4. Macroscopic modelling
4.1 Introduction
4.2 Theory
4.2.1 Model Overview
4.2.2 Calculating the response I

4.2.3 Calculating the electric field
4.2.4 Calculating the response II
4.2.5 Calculating the concentration
4.2.6 Outline of computational procedure
4.3 Results
4.3.1 Discussion of model accuracy
4.3.2 Single phase sensor
4.3.3 Inclusion of a zeolite over-layer
4.4 Conclusions

5. Correlation of results from diffusion models with experiment
5.1 Introduction
5.2 Response of CTO-SOLGEL sensors to fragrance molecules
5.3 Response of wide and narrow gap electrode sensors to alcohols and linear paraffins
5.4 Response of single electrode, zeolite-modified sensors to ethanol and carbon monoxide
5.5 Response of zeolite-modified sensors to methane and ethanol
5.6 Conclusions

6. Conclusions and future directions

Table of Key Symbols (ordered as they first appear)

G	Fractional change in sensor resistance (R) given by $G = (R-R_0)/R$ where R_0 is the baseline resistance of the sensor. G could also be the fractional change in conductance. In chapter 4, however, the fraction response change is referred to as $\frac{G(\tau)-G_0}{G_0}$ for conductance.
A_g	Sensor sensitivity.
C	Concentration – often taken to be a function of three-dimensional space ($\vec{r}$) and time (t) as introduced below.
β	Response exponent.
ϕ	Porosity i.e. the pore-space fraction of the total volume of porous solid.
σ	Conductivity.
$\vec{r}$	Three-dimensional space vector.
t	Time.
D	Diffusivity.
k	Rate constant.
D_e	Effective diffusivity (of composite material approximated by an effective medium).
D_p	Pore diffusivity i.e. within the bulk-phase pore fluid.
Si/Al	Ratio of silicon to aluminium atoms comprising a given zeolite framework.
E_{be}	The binding energy of the gas within the zeolite framework i.e. $E_{be} = (E_z + E_g) - E_{z+g}$ where E_z and E_g are the energies of the zeolite and gas systems respectively and E_{z+g} is the energy of the combined system.
$G(\vec{r},\vec{r}',t)$	The diffusion propagator – equivalent, in the context of the discussion in chapter 3, to the concentration. It can be distinguished from the sensor response, G, as it is always a function of two position vectors and of time which is never true of the sensor response.
ρ	Reaction rate of reaction occurring at surface of impenetrable particle (of metal oxide) surface. (This is for chapter 3 only)
λ	Eigenvalues of the concentration solution.
$\phi_\lambda(\vec{r})$	(space dependent) Eigenfunctions of the concentration solution.
$\mu(\vec{r},t)$	Chemical potential.
$n_\mu(\vec{r})$	The thermodynamic derivative equal to $\frac{\partial C}{\partial \mu}$.
$\vec{g}$	The truncated set of reciprocal lattice vectors
$\vec{q}$	A wave-vector in the 1st Brillouin zone – used in evaluation of effective diffusivity.

$\theta_1(\vec{r}) = 1 - \theta_2(\vec{r})$	Indicator functions of the two phases comprising a two phase composite medium – defined by the relation shown. In integral form this becomes geometry input $\theta^{(2)}_{g-g'}$.
z	Partition function $z = \frac{n_{\mu 2}}{n_{\mu 1}}$.
$K(\vec{g})$	Geometry input for impenetrable obstacles system.
N_g	Number of reciprocal lattice vectors used for the calculation.
$G_{av}(t)$	Average concentration over total number of grid points and normalised to the average concentration where no reaction occurs.
D_s, D_z	The bulk effective diffusivities calculated for the sensor (s) and zeolite (z) systems respectively.
k_e	Effective rate constant.
C_0	The gas concentration incident upon the sensor layer surface (for macroscopic model)
h_s, h_z	Thickness of the sensor (s) and zeolite (z) layers comprising the macroscopic sensor.
b	Electrode length.
w	Electrode width.
d	Electrode separation. Typically expressed as d/h_s.
i	Current through sensor layer. Typically given as a function of time: $i(t)$.
V	Fixed applied voltage.
E	Electric field established within the sensor layer.
ρ	Resistivity (This is for chapter 4 only).
τ	Dimensionless time as $D_s t/ h_s^2$.
T_s	Time constant equal to h_s^2 /D_s.
Γ	Dimensionless concentration as C/ C_0.
K_s	Dimensionless rate constant for reaction occurring in the sensor layer as $k_s T_s$.
K_z	Dimensionless rate constant for reaction occurring in the zeolite layer as $(k_z/k_s)K_s = k_z T_s$.
R_{ag}	The ratio of sensitivities of the sensor to product and reactant $R_{ag} = A_{gp}/A_{gr}$.
ΔX	Space step for finite difference / Euler calculation.
$\Delta\tau$	Time step for finite difference / Euler calculation.
λ	Accuracy condition for finite difference / Euler computation: $\lambda \le \frac{1}{2}$ where $\lambda = \frac{\Delta\tau}{\Delta X^2}$

Table of Equations

$$G = A_g C_g^{\beta}$$ Equation 1.1

$$\frac{\partial C(\vec{r},t)}{\partial t} = \nabla \cdot (D(\vec{r},t)\nabla C(\vec{r},t)) - k(\vec{r},t)C(\vec{r},t)^{\gamma}$$ Equation 1.2

$$D_e / D_p = \phi\delta / \tau$$ Equation 1.3

$$E_{be} = (E_z + E_g) - E_{z+g}$$ Equation 2.1

$$q_{zg} = H_g - H_z$$ Equation 2.2

$$E[\rho] = T[\rho] + U[\rho] + E_{xc}[\rho]$$ Equation 2.3

$$J = -D_t \nabla C$$ Equation 3.1

$$< \bar{r}(t) >= 6D_s t$$ Equation 3.2

$$\frac{\partial C(\vec{r},t)}{\partial t} = \nabla \cdot (D(\vec{r},t)\nabla C(\vec{r},t)) - k(\vec{r})C(\vec{r},t)$$ Equation 3.3

$$C(\vec{r},t) = \phi_\lambda(\vec{r})e^{-\lambda t}$$ Equation 3.4

$$C(\vec{r},\vec{r}',t) = \sum_\lambda e^{-\lambda t}\phi_\lambda(\vec{r})\phi_\lambda^*(\vec{r}')$$ Equation 3.5

$$n_\mu(\vec{r})\frac{\partial \mu(\vec{r},t)}{\partial t} = \nabla \cdot \left[D(\vec{r},t)n_\mu(\vec{r})\nabla\mu(\vec{r},t)\right] - k(\vec{r})n_\mu(\vec{r})\mu(\vec{r},t)$$ Equation 3.6

$$\phi_\lambda(\vec{r}) \to \phi(\vec{r})_{n\vec{q}}\, e^{i\vec{q}\cdot\vec{r}}$$
$$\lambda \to \lambda_{n\vec{q}}$$ Equation 3.7

$$\varphi_{n\vec{q}}(\vec{r}) = \sum_g \tilde{\phi}_{n\vec{q}}(\vec{g})e^{i\vec{g}\cdot\vec{r}}$$ Equation 3.8

$$\lambda_{n\vec{q}}\hat{W}\tilde{\phi}_{n\vec{q}} = \hat{\Gamma}\tilde{\phi}_{n\vec{q}}$$ Equation 3.9

$$-\lambda n_\mu(\vec{r})\phi_\lambda(\vec{r}) = \nabla[D(\vec{r})n_\mu(\vec{r})\nabla\phi_\lambda(\vec{r})] - k(\vec{r})n_\mu(\vec{r})\phi_\lambda(\vec{r})$$ Equation 3.10

$$-\lambda W(\vec{r})\varphi_\lambda(\vec{r}) = D_2\nabla\cdot[U(\vec{r})\nabla\phi_\lambda(\vec{r})] - k_2 X(\vec{r})\phi_\lambda(\vec{r})$$ Equation 3.11

$$\lambda_{nq}\sum_{g'} W_{gg'}\tilde{\phi}_{nq}(\vec{g}') = \sum_{g'}\Gamma_{gg'}\tilde{\phi}_{nq}(\vec{g}')$$ Equation 3.12

$$\Gamma_{gg'}(\vec{q}) = D_1(\vec{g}+\vec{q})\cdot(\vec{g}'+\vec{q})(\delta_{gg'} - u\theta^{(2)}_{g-g'}) + k_1(\delta_{gg'} - x\theta^{(2)}_{g-g'})$$ Equation 3.13

$$V_{nm}(\vec{q}) = 4\sum_g\sum_{g'}\tilde{\varphi}^*_{nq}(\vec{g})K(\vec{g}-\vec{g}')\tilde{\phi}_{mq}(g')$$ Equation 3.14

$$\theta_g^{(2)}(\vec{g}) = \frac{1}{V_a}\int_{V_a} dV\theta_2(\vec{r})e^{-ig\cdot r} \qquad \text{Equation 3.15}$$

$$\lambda_{nq}(\hat{R}\tilde{\phi}_{nq}) = D_p\hat{\Lambda}(\hat{R}\tilde{\phi}_{nq}) \qquad \text{Equation 3.16}$$

$$i(t) = \mu_e eb\int_0^{h_s} nEdx \qquad \text{Equation 4.1}$$

$$\Delta G(\tau) = \frac{\sigma_0 A_g b}{V}\int_0^1 \Gamma(X,\tau)EdX \qquad \text{Equation 4.2}$$

$$\frac{[G(\tau)-G_0]}{G_0} = A_g\frac{\int_0^1 \Gamma(X,\tau)/\sqrt{((X-1)^2+d^2/4h_s^2)}dX}{\ln[1+\sqrt{(1+d^2/4h_s^2)}/[d/2h_s]]} \qquad \text{Equation 4.3}$$

$$\frac{G(\tau)-G_0}{G_0} = A_g\frac{\int_0^1 \Gamma(X,\tau)dX/\sqrt{[X^2+d^2/4h_s^2][M^2X^2+d^2/4h_s^2])}}{\int_0^1 dX/\sqrt{([X^2+d^2/4h_s^2][M^2X^2+d^2/4h_s^2])}} \qquad \text{Equation 4.4}$$

$$\frac{\partial C_r(\vec{x},t)}{\partial t} = D_r\frac{\partial^2 C_r(\vec{x},t)}{\partial x^2} - k_r C_r(\vec{x},t) \qquad \text{Equation 4.5 (a)}$$

$$\frac{\partial C_p(\vec{x},t)}{\partial t} = D_p\frac{\partial^2 C_p(\vec{x},t)}{\partial x^2} + k_r C_r(\vec{x},t) \qquad \text{Equation 4.5 (b)}$$

$$\frac{\partial \Gamma_r}{\partial \tau} = \frac{\partial^2\Gamma_r}{\partial X^2} - K_s\Gamma_r; \quad \frac{\partial\Gamma_p}{\partial\tau} = \frac{D_{sp}}{D_{sr}}\frac{\partial^2\Gamma_p}{\partial X^2} - K_s\Gamma_p \qquad \text{Equation 4.6}$$

$$\Gamma(X) = \frac{\cosh((h_s - X)\sqrt{K_s})}{\cosh(\sqrt{K_s})} \qquad \text{Equation 4.7}$$

$$\Gamma_i(T+\delta T) = \Gamma_i(T) + \lambda(\Gamma_{i-1}(T) - 2\Gamma_i(T) + \Gamma_{i+1}(T) \qquad \text{Equation 4.8}$$

$$\lambda \le \frac{1}{2} \text{ where } \lambda = \frac{\Delta T}{\Delta X^2} \qquad \text{Equation 4.9}$$

Chapter 1: Introduction to solid state gas sensors and the use of zeolite layers for enhancing selectivity

(1.1) Introduction

Gas sensing technologies rely on some interaction occurring between gas molecules and the sensing material and that this chemical information can be translated into a measurable output. Whilst two molecules may be distinct in many respects, such as size, shape and composition, information is inevitably lost on measurement.

Solid state metal oxide sensors respond in the presence of a gas with a change in conductivity due to the change of electron density, initiated at the surface of the device, as the composition of the environment surrounding the sensor surface is altered [1]. In itself, this is not sufficient to ensure a useful level of discrimination and versatility for different separation tasks, especially as the concentration and background environment of the gas of interest may be largely unknown. For example, in [2] it is demonstrated that Pd-doped tin oxide sensors are sensitive to both paraffins and alcohols but that discriminating between the two proves difficult.

The need for repeatability presents another major challenge, the response is found to be highly sensitive to, often only slight, variations in experimental conditions and the fabrication process. For example, the presence of water vapour is shown to have both reversible and irreversible effects on the response of tungsten trioxide to ozone [3], the latter case being an example of the wider problem of poisoning of the device surface by certain species, leading to a change in the base sensitivity.

However, the dependency of response on the fabrication and operation can in fact be exploited advantageously in terms of the potential discriminating power of metal oxides [4]. The way in which the response varies, say with an increase in average particle size of the sensitive material or operating temperature, depends in turn on the properties of the gas. Additionally it is possible to modify the nature of the gas stream interacting with the sensor directly by use of a "transformation element" – essentially some distinct material element that will modify the gas stream by promoting a reaction or via diffusional control. In [2], they show that the discrimination between paraffins and alcohols, not possible with the control SnO_2 sensor, can be achieved using a zeolite overlayer.

With the ability to optimise the sensing device via its structural properties and also with the use of several sensors, which may have partial selectivity, together in an array, there is enormous potential for the use of metal oxides as tuneable, selective devices. However further understanding is required of the different factors influencing response and their interdependencies which are, at least, known to be complex.

Here, the fundamentals of sensor response are introduced and observations of the different dependencies are reviewed along with key theoretical models – with the aim of putting the current work into context. In particular, the use of a zeolite transformation-layer is considered.

(1.2) Modelling the sensor system

(1.2.1) Primary considerations

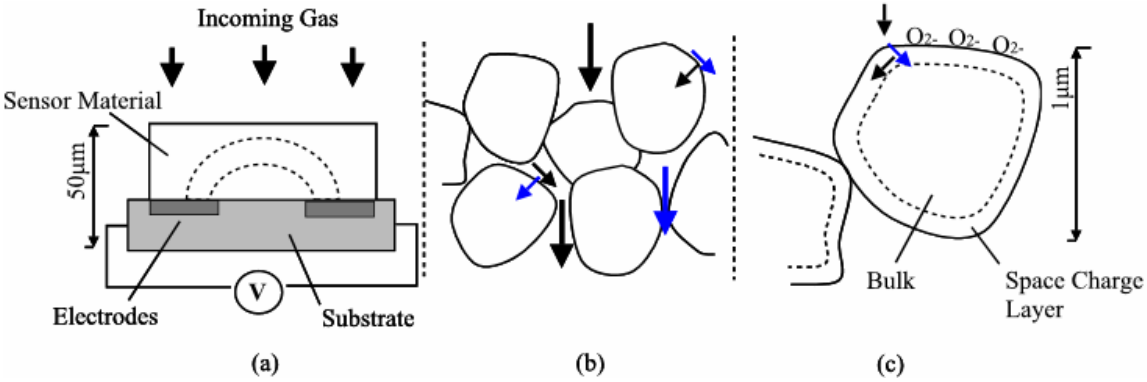

Figure 1.1: The sensing process on different scales. Average dimensions given.

Figure 1.1 illustrates different aspects of the gas sensing system on different length scales. The devices of interest here typically consist of a thick (10^1-10^2µm), porous film of semiconducting metal oxide positioned upon an insulating substrate and incorporated within an electrical circuit via the use of electrodes (figure 1.1(a)). The sensors used specifically for this investigation are prepared following the method of screen printing, a description of this technique, along with a more general discussion of sensor fabrication, is given in [5].

On subjecting the system to a change in its gaseous environment, ultimately the current that flows between the electrodes is modified giving a measurable change in the device resistance. This response change is a consequence of the interaction between gas and the solid oxide or ambient surface adsorbed oxygen (as depicted in figure 1.1(c)) and the resulting charge transfer therefore depends on the chemistry of the gas and the metal oxide e.g. stoichiometry, doping.

The response will also be dependent on the concentration of gas through the device which in turn depends on the gas diffusion, adsorption and desorption at the sensor surface and the occurrence of any catalysed reaction. The sensing layer presents a porous network (figure 1.1(b)) through which the gas must diffuse – the details of the microstructure – the porosity, tortuosity and particle size – strongly influencing the

transport and reaction properties of the gas. Also larger scale device geometry – device thickness and electrode separation – is important due to the formation of concentration gradients within the device.

Another consideration of the microstructure is the influence of geometrical properties of the porous network of crystallites on the device resistance – namely the size of particles (compared to the Debye length, i.e. the length over which the local electric field affects the distribution of free charge carriers) and the nature and number of the contacts between particles.

The empirical representation of sensor response is commonly taken as [6]:

$$G = A_g C_g^{\beta} \qquad \text{Equation 1.1}$$

where $G = (R - R_0)/R_0$, i.e. the fractional change in resistance, R, where R_0 is the baseline resistance i.e. in the absence of the target gas. Alternatively G could be the fractional change in conductance. C is the gas concentration (or target gas partial pressure). β, the response exponent, and A_g, the sensitivity, which depends on the gas and on the properties of the sensor discussed above.

The matter of determining β and A_g is a focus of the rest of this section.

(1.2.2) Gas-metal oxide interaction models – relating gas concentration to local conductivity

At the heart of the conductive response is, of course, the interaction between the gas and the sensor material. Whilst the precise details of mechanisms of different oxide-gas systems may be unknown, sensor behaviour can be more broadly characterised according to two different schemes [7]. Firstly the conduction may be modified by a change in the bulk oxygen content. In this case, the material is sensitive to changes in partial pressure of oxygen in the surrounding environment, a new equilibrium being reached between the ambient oxygen and the oxygen defects of the metal oxide, resulting in a change in conductivity. This is useful, for example, for combustion control systems [8] but the metal oxide will not be sensitive to small changes in other gases; which is what is required for the application discussed here. If however, the diffusion of the oxygen vacancies is sufficiently slow (which is, of course, somewhat dependent on operating temperature [9]), the charge transfer that occurs from the

interaction of gas at the surface becomes dominant in determining the conductivity of the device.

To date, the most widely investigated metal oxide for detection of trace gases is SnO_2, as used for the first commercial semiconducting sensor device – the Taguchi sensor [10]. SnO_2 is classed as an n-type material as are many of the other popular semiconducting sensing materials. N-type materials typically give an increase in conductance in response to a reducing gas and a decrease in conductance to an oxidising gas. Such behaviour is attributed to adsorbed oxygen on the sensor surface (providing there is oxygen in the surrounding environment) creating a charge (electron) depletion layer at the surface. A reducing gas therefore increases the conductivity by reacting with the adsorbed oxygen and hence injecting electrons into the conduction band [1,11]. How this then translates into an electrical signal of a given sensitivity (A_g) depends on electro-physical properties such as the material's band gap which in turn depends on details of composition of the metal oxide [12].

P-type materials, such as perovskites [13,14] or chromium titanate, $Cr_{2-x}Ti_xO_y$ (CTO) [15], have more recently become of interest for gas sensing. They are generally observed to have the opposite response behaviour to reducing and oxidising gases compared with n-type materials. An analogous model for p-type conductance change has been put forward, with some success [16,17], which assumes the formation of an accumulation layer of holes on the adsorption of ambient oxygen. However, it has been argued by Sahner and Moos [13] that the formation of an accumulation layer is actually implausible (at least when bulk conductivity is not negligible) and it is suggested that the bulk oxygen also interacts with the reducing gas. Results from their subsequent model correlated well with experimental response data of sensors (of different thicknesses and at different temperatures) to different hydrocarbons.
The classification of a sensor material as n- or p-type can, in fact, be considered as an operational characterisation, as there are instances when the same material may show n- and p-type behaviour depending on operational conditions such as gas concentration [18,19].

In any case, one can relate the local conductivity, σ, to the partial pressure of the target gas via the surface coverage, θ, of the target gas – a relationship which as a first approximation is commonly taken as $\sigma \propto \theta$ [20].

The surface coverage for metal oxides is typically described by a Langmuir or Freundlich isotherm model and an expression for θ can be given in terms of the rates of the different processes involving different species and their partial pressures, i.e. the formation of oxygen states on the surface and the subsequent reaction of the target gas [7]. More detailed isotherm models have also been considered, for example [21].

Following along these lines, values for β from equation 1.1 have been proposed based on the stoichiometry of the reactions that occur on the surface [22]. The charge state of chemisorbed oxygen will also clearly play a part – different possible forms having been investigated inconclusively [23,24,25]. Typically these types of arguments predict β of 1 or 0.5. In contrast, irrational values for β are often obtained experimentally [26,27].

The root of the discrepancy between the forms for β predicted from simple models and the experimentally observed values almost certainly will lie in the reality of the microstructure which, as was discussed above, influences the transport of gas through the pores of the metal oxide and the charge transfer between the crystallites.

Following the same types of argument, one can propose a condition for the sensitivity of the device based on the reaction kinetics i.e. the comparative rate of oxygen ion formation and rate of the reverse process and also the reaction rate of the target gas at the surface – which must be the dominant process. These are considered to be activated processes and hence the different rates (including diffusion rates of gas and charge carriers) are temperature dependent as reflected in the sensor response temperature dependency, generally observed to be of Arrhenius type [28]. Again, rates will also depend on the material properties that control the adsorption and desorption parameters and the catalytic activity and that can be modified by varying the surface composition of the metal oxide [12].

As with the response exponent, the sensitivity can vary greatly between preparations and again the reason for this is attributed to details of the microstructure that have so far not been considered in the rationale of sensor response. Issues of microstructure are now discussed.

(1.2.3) Conductivity models – relating sensor response to local conductivity

So far we have considered only the change in conductivity, due to the introduction of trace gases to the surrounding atmosphere, of the charge layer present due to atmospheric oxygen adsorption at the sensor surface. The simplest approach to finding the response, given the relation between local conductivity and gas concentration, is to assume that the change in conductance of the device, as a whole, is directly proportional to the microscopic conductivity change at the surface. However, if the grains are larger than the thickness of the charge layer, i.e. the Debye length of the solid, then the presence of two regions, surface and bulk, must be reflected in the formalism for conductance. One can hence extend the previous discussion to formulate surface-limited and barrier-limited models for conductance where "barrier" refers to the activation of electrons occurring across the surface-bulk barrier [7]. The effect of varying the particle size has been widely studied experimentally [29,30,31,32]. A key result is the steep increase in sensor sensitivity as the grain size decreases to dimensions of the Debye length, often referred to as the "dimension effect".

It is also necessary to consider the dimensions of the contacts between grains. Again there are the cases of contact dimensions being more or less than the Debye length and additionally there is a third possibility, the limiting case of the contact being narrow and short, when it may present a non-ohmic Schottky barrier. For example, in [33] a model is presented of metal oxide crystallites with depletion layer and bulk regions and grain contacts represented as Schottky type barriers. Through this model, for different gases, they derive different irrational response exponents that tend to rational limits as predicted from the reasoning in the previous section. However, this model assumes an ideal system of large grains.

Aside from a description of the connection itself, it is also necessary to address the question of connectivity as a property of the sensing layer as a whole. The sensor network can be thought of as a percolating system (percolation theory being the theory of connected bodies randomly positioned on a network [34]). The point at which long-range connectivity first occurs is known as the percolation threshold and is expected to present a detection threshold i.e. there must be sufficient connectivity for the structure to work as a gas sensor. This is typically observed as a threshold for concentration of the target gas as the presence of the gas may lower intergrain barriers, such that a conductive path between electrodes is established. This threshold can be varied by varying details of the microstructure such as porosity and particle size and the average

coordination number of the sensing layer [27,35,36]. In [27] and [36] a percolation approach is used to look specifically at the response form and again an irrational response exponent is predicted along with variable sensitivity, as is found experimentally, depending on details of the microstructure. A drawback is that these models don't account for the possibility of inaccessible regions of grains that might occur due to agglomeration during the sintering process. In fact one can think of the gas flow through the system as a second percolating system: the gas must be able to permeate the metal oxide sufficiently so that the critical concentration can be achieved.

Another network approach is to model gas sensitive and gas insensitive conductive regions of a metal oxide crystallite by a simple resistor circuit (assuming moderate overlap of particles with surface-trap limited behaviour) [37]. These can then be used as the domains of a random resistor network which represents the porous sensor network of porosity, ϕ. In this case the conductivity, σ, can be calculated using the Kirkpatrick formulation [34] which holds when the network is far from the percolation threshold (where σ_N is the conductivity of an individual network element):

$$\sigma = \sigma_N (1 - \frac{3}{2}\phi)$$

Different combinations are required to produce irrational response exponents depending on whether the system exhibits a resistance increase or decrease on introduction of the gas which can be justified by considering the different conduction models of n- and p-type materials as introduced in the previous section. Good agreement with experimental results has been shown for various systems [3,27,38] and again this approach offers valuable insight into the dependency of response sensitivity and the response exponent and on particle size, porosity, surface area. An important result is the correlation between the response exponent and the sensitivity that exists even though the individual quantities vary widely as the microstructure is modified.

What all of these models have in common is the conclusion that the conductive behaviour is highly dependent on the sensor microstructure – and that a (gas dependent) balance between optimising different aspects of the behaviour through fabrication choice needs to be realised in order to achieve a successful sensor design. For example, there is a need for compromise between an open microstructure – offering as large as

possible surface area for interaction with gas – and at the same time having a sufficiently connected microstructure. Also, whilst smaller particles will have a higher surface area favourable in terms of the dimension factor, these particles will then be more susceptible to sintering which would lead to low accessibility of the active surface. Additionally, aside from the conductive behaviour i.e. the transport of charge carriers, there is also issue of how the microstructure shapes the transport and reaction behaviour of the gas – this is now considered.

(1.2.4) Concentration variation

Clearly the concentration of gas reaching the internal surface of a porous sensor and the way it varies is going to play an essential part in determining the response of the sensor device. The occurrence of reactions catalysed upon the sensor surface, potentially to a product or products of very different sensitivity, results in a gradient in concentration through the device that depends on the balance between how quickly the gas penetrates into the porous layer and how quickly it reacts at the internal surface. As a result, the steady state response will be gas dependent in terms of its rate constant and diffusivity and additionally the transient behaviour of the device will also depend on these factors. That there is this second aspect to the sensor response, a dynamic characterisation, turns out to be highly important. The response time has shown to be dependent on the specific gas/sensor material combination whilst also being independent of concentration and arguably offers better repeatability than the steady state response [39]. However, the response time can be difficult to measure reliably due to possible occurrence of changes in operating conditions. Variable gas concentration is of course not the only contributor to the transient behaviour – one must also consider the transient behaviour of the charge carriers and their propagation through the complex microstructure, such as is described in the percolation model introduced above [36]. It is, however, generally regarded that gas transport is the limiting process here [27].

The issues of diffusion, reaction and diffusive-reactive balance have been duly noted both experimentally and theoretically – for example the response has been shown to vary with sensor layer thickness according to the ratio of kinetic and diffusive parameters [40]. In [41] it is shown that benzene and o-xylene give very similar steady state responses on Taguchi tin oxide sensors but that the response time is much greater for o-xylene such that it is possible to distinguish between them, thought to be due to

the comparatively slow diffusion of o-xylene and in [42] differences between H_2 and O_2 response are attributed to their diffusive behaviours through the porous layer.

Another realisation is the variation of response with electrode geometry [43,44] as varying the spacing between electrodes effectively changes the region of the sensor device that is analysed and hence offers a means of investigating the spatial variation of the concentration profile. Williams and Pratt [43] proposed the use of an array of electrodes on a single sensor element, equivalent to an array of sensor elements. It has been shown that such a device has the potential to determine parameters of the gas such as the rate constant (although the rate constant will also depend on properties of the sensor)[45], may be useful for the detection of device poisoning [46] and also that measurements on different electrode spacing could offer a more robust method of determining response times [43].

In modelling concentration variations, a standard approach to describing the diffusive system is to use Fick's laws [47,48]. In particular, Fick's second law describes the spatial and temporal variation of the concentration, *C*, where the gas diffuses with diffusivity, *D*, and can be easily adapted to include the occurrence of a reaction of rate constant *k* and order γ as given in equation 1.1. $\vec{r}$ is the position vector (in Cartesian space) and t denotes time.

$$\frac{\partial C(\vec{r},t)}{\partial t} = \nabla \cdot (D(\vec{r},t)\nabla C(\vec{r},t)) - k(\vec{r},t)C(\vec{r},t)^{\gamma} \qquad \text{Equation 1.2}$$

The following must then be accounted for:

1. A rate constant and order parameter must be provided for the reaction – note the "reaction" could describe an adsorptive process as is usually the case for conducting polymer models where reversible interaction of gas at the polymer surface is generally predicted. With metal oxides an irreversible reaction at the surface is more typical.
2. An appropriate measure of diffusivity for the gas is required.
3. The partial differential equation must be solved for appropriate boundary conditions.

To give a complete space and time dependent description of the reaction and diffusion parameters requires involved tensor representations. Hence, for the geometrically complex systems under consideration here, from a practical point of view, it is necessary to assume effective diffusivities and rate constants that are constant with

space and time – a justified approximation where the pores are fine to the extent that gradients do not form across them. Assuming an effective medium also simplifies the task of imposing boundary conditions as simpler ideal macroscopic geometries can be considered. Commonly the effective diffusivity, D_e, of a gas within a porous solid is written as [7,13]:

$$D_e / D_p = \phi\delta / \tau \qquad \text{Equation 1.3}$$

Where D_p is the diffusivity of the gas in the pore phase, ϕ is the porosity, δ is the constrictivity and τ is the tortuosity of the solid system.

Equation 1.2 can then be solved to obtain the concentration profile using numerical methods (and in some instances analytical methods) for solving partial differential equations. From this the response can be calculated, taking into consideration the issues that were introduced in sections 1.1.2 and section 1.1.3.

Diffusion and reaction in porous or composite environments, and the calculation and validity of effective quantities, are themes of discussion throughout the work presented in this thesis.

(1.2.5) Sensor arrays

Clearly there is the capacity to vary and control the response characteristics of a metal oxide sensor, be it through the fabrication procedure of the sensor layer, through choice of electrodes and their positioning or the thickness of the device or, as will be discussed in the next section, with the addition of an overlayer that will in some way modify the gas stream. The question is how to harness this potential to discriminate effectively which requires appropriate optimisation and interpretation of the sensor behaviour.

An approach to effectively harness available information is to combine single sensor elements (which may be two-phase, i.e. sensor and zeolite layers) in an array where, although elements may have low selectivity, the device as a whole will respond such that the desired selectivity can be achieved via the use of specific pattern recognition techniques. This is essentially the concept of the electronic noses (or e-nose) – an idea that first came into being in the 1960s, its place in science being consolidated in the 1980s. Here the definition is given as that of Gardner and Bartlett [49] as “an instrument, which comprises an array of electronic chemical sensors with partial specificity and an appropriate pattern-recognition system, capable of recognising

simple or complex odours" – and of course this can then be extended to refer to gases in general.

The electronic nose has been successfully developed for various tasks including simple organic vapours [39], perfumes [50] and numerous foodstuffs – for example tea (flavour identification) [51], coffee blend [52] and fruit (ripeness) [53]; several such applications are discussed in [54]. There has also been development into the use of the e-nose for the monitoring of environmental gases [55] and in the field of medical diagnostics [56] including the detection of infectious bacteria [57] and lung cancer [58]. Arrays using sensors with additional zeolite layer have also been reported [59].

In order to effectively interpret the response of an array of sensors one must apply multivariate pattern recognition methods, which exploit cross-correlations and map patterns in the data to class-memberships. Firstly a calibration step is performed in which a *knowledge base* is formed by mathematically characterising the response of the array of sensors to known gases. After calibration, the device can be used to identify a gas by predicting its class-membership – testing the array response to the unknown gas against the knowledge base. It is the process of feature extraction, known as supervised learning, that really determines the quality of the whole pattern recognition process, the main issue to be addressed being the appropriate sampling of the gaseous environment.

A powerful and hence commonly used method of feature extraction is principle component analysis (PCA). This method enables the reduction of the number of variables to a smaller set of uncorrelated principle components [60]. The principle components are ordered in terms of the amount of information they contain, or their relevance, and hence this method can be thought of as a way of removing irrelevant data from the complex data set. PCA is a linear method restricting it somewhat to small concentrations of the test gas for which this assumption is generally valid. A popular non-linear approach is to use an artificial neural network model [61] which more closely mimics the human olfaction system. PCA and neural network techniques are non-parametric methods – essentially meaning a probability distribution is not assumed making these methods more general in application than say parametric discriminant function analysis (DFA) which determines variables that can be used to discriminate between different groups to give an estimate of the class-membership or attributes of the pattern [52]. Often it is the case that more than one method is used.

In a second step of unsupervised learning, typically methods of cluster analysis are used where the patterns in the data set are recognised such that it can be divided into subsets based on class-membership and the gas is identified [60].

From a practical point of view the number of sensors in the array is limited as one must also consider power consumption and that the problem of response drift accumulates as the array size increases and hence optimum array design becomes the minimal array size possible capable of fulfilling a specific task, i.e. the aim is for maximum variance from minimal array size.

(1.3) Zeolites and their application to gas sensing:

(1.3.1) An overview

Zeolites are a class of highly porous materials with unique physical and chemical properties. They are comprised primarily of silicon, aluminium and oxygen in the form of tetrahedral units of $[SiO_4]^{4-}$ and $[AlO_4]^{5-}$. These then fit together to form the 3-dimensional structure of rings, pores and interlinking channels with each of the oxygens acting as a bridging atom between a silicon and either another silicon or an aluminium atom. There are, at present, nearly 200 known zeolitic frameworks [62] (either naturally occurring or produced synthetically) however only about 10% of these have really been explored for their scientific and commercial worth.

Large internal surface areas mean that surface adsorption and hence transition from gas to zeolite phase can be highly favourable. The pore and channel dimensions, comparable to typical molecular dimensions, vary amongst the many synthetic and naturally occurring zeolite compounds and this diversity, along with their ability to hold and exchange cations, underlies their suitability for a wide range of commercial uses. Commonly referred to as “molecular sieves” [63], the specific topology of the zeolite framework may restrict molecules of certain shape and size being adsorbed or favour the adsorption of one molecule over another. For example the strength of adsorption of linear hydrocarbons in the channels comprising zeolite ZSM-5 increases linearly with increasing chain length due to the increased interactions between sorbate and zeolite [64] and similarly a distinction can be made between branched and straight chain alkanes [65].

The presence of cations, which balance the charge of an aluminium containing unit, firstly alters the size of the pores and the volume accessible to the sorbed species. Secondly a zeolite with a low Si/Al ratio is described as being energetically heterogeneous which refers to the energetic variation of the binding sites available to molecules due to the presence of both silicon and aluminium sites - the high cation concentration associated with a low ratio providing a further contribution heterogeneity of the energy landscape. A low Si/Al ratio is indicative of a charge-polarised structure which will preferentially adsorb polar molecules. Clearly the polar nature of the zeolite will be sensitive to the number of cations present – also the resultant selectivity to different adsorbents is strongly dependent on the cation type as described by Pampai et. al. [66] who showed, using first principles simulation, that the presence of Li^+ ions within a zeolite framework will enhance the selective adsorption of nitrogen over oxygen to a greater degree than Na^+ ions (a result also observed experimentally). Hence a useful property of zeolites is that these ions can be exchanged (the Si/Al ratio may also be modified).

Ion sites within zeolites may also be sites of catalysis and zeolites are used as catalysts (typically acid catalysts where the cation is an H^+ ion) for a vast range of industrial applications [67]. Catalysis in zeolites is generally considered a highly challenging topic to probe though it is well known that shape and size selectivity is again of major importance in understanding the behaviour observed.

In summary, zeolites may exhibit selectivity to different gases in either or both of the following ways:

1. Physical selectivity: A closely fitting molecule-pore system may result in increased bonding and hence enhanced adsorption therefore increasing the probability of the molecule moving from the gas phase to sensor phase. The molecule may also be blocked completely from entering the zeolite framework.
2. Chemical selectivity: Certain functional groups may bind more strongly and a reaction may be catalysed within the zeolite such as to chemically transform the gas stream.

(1.3.2) Zeolites for gas sensing

There are several possible ways in which the selective properties of zeolite compounds can be utilised for the purpose of gas sensing as reported by Xu et. al [68]:

1. A gas sensing compound can be inserted inside the zeolite cage or channel.
2. Zeolites can be fixed on a quartz crystal microbalance to monitor the uptake of gas.
3. Changes in conductivity of the zeolite itself due to its selective adsorption and subsequent cation transport can be measured via impedance spectroscopy measurements.
4. A zeolite layer can be added to the sensor structure as a catalytic or size-restrictive filter layer.
5. Zeolite particles can be immersed within the sensor structure.

Here we consider the application of the zeolite as in 4 – performing a purely auxiliary role in transforming the test gas stream before it meets the metal oxide sensing layer. Zeolites have proved to be successful in enhancing sensor discrimination in this way, as has been previously mentioned in [2] they show that discrimination between low weight alcohols and alkanes is possible using a zeolite MFI or LTA overlayer where it was not possible with the control sensor. This is reasoned as being due to increased diffusion resistance with the addition of the zeolite layer which is counteracted by strong interactions of ethanol with the cation containing zeolite framework such that the response is not suppressed as with non-polar alkanes. Pariffin/alcohol distinction is also shown in [69] with the use of zeolite mordinite – that more ethanol is adsorbed in the zeolite, compared to n-hexane, is shown using chromatography. In [70] they show response of SnO_2 to a range of small molecules and how the response with either zeolite-A or silicalite gives enhancement, reduction or maintains the same response dependent on the particular gas/zeolite combination. They also discuss an increase in response time which is zeolite dependent occurring more for silicalite than zeolite-A.
In [71], active ZSM-5 is used to eliminate cross-inference of NO in the response of p-type perovskites to hydrocarbons. The zeolite layer enhances the response to alkanes, although this occurs to a lesser extent for unsaturated molecules, an effect explained in terms of a Fickian diffusion-reaction model, as discussed above. The catalytic activity is also exploited to show the possible discrimination along a series of alkanes of increasing chain length using a CTO sensor with a zeolite-Y cover layer doped with transition metal ions such as chromium, known for their catalytic properties [72] .
Ultimately the vast number of different types of zeolites and the possibility of engineering them to suit specific needs is highly advantageous for their use in gas sensing. There is much greater versatility available than with other possible filter

materials such as active carbon and mesoporous silica, and there is hence potential to tackle a much greater number of gas discrimination tasks. Zeolites are also much more robust than many other potential filter materials, typically being structurally stable to approximately 400-500°C

(1.3.3) Transport through the zeolite layer

A more detailed understanding of how the zeolite works as a transformation layer requires knowledge of the transport properties of gases through the zeolite film. As has been discussed for the sensing layer, transport through the porous zeolite is a consequence of different mechanisms including adsorption, diffusion and reaction, all strongly influenced by the confining porous framework. Here the situation is complicated further by the presence of two porous systems spanning different length-scales. The zeolite layer can be prepared by screen printing as with the sensor layer – it is noted that the quality of the zeolite layer has been observed to be important to the selectivity of the layer [70]. The zeolite film is porous following the sintering of the zeolite crystallites during the preparation of the film with pore sizes ranging between 0.5-2μm. The crystallites themselves are of course also porous, the pores being on the scale of molecular dimensions as discussed above.

So the matter is now more complex; not only as there are now two networks to consider, whose transport and reaction properties are interdependent, but also because the transport through the smaller system encounters constraints of microscopic dimensions leading to transport being much harder to model due to the requirement of a more detailed picture of the atomic environment.

For a freely diffusing gas, the variation in its concentration with space and time can be easily computed; the gas spreads out from a concentrated initial configuration following a standard Gaussian distribution function. Where there are barriers to diffusion and the gas is confined, the picture becomes far more complicated. The extent of the influence of confinement is clearly going to depend on the relative scales of the barrier dimensions and the molecular dimensions.

As barrier-particle collisions become more frequent than particle-particle collisions, the diffusion behaviour is described as being of the Knudsen regime for which for the diffusion coefficient, D_K, can be calculated following:

$$D_K = \frac{2r}{3}\sqrt{\frac{8RT}{\pi M}}$$

where r is the pore radius, T is the absolute temperature, R is the molar gas constant and M is the molar mass. The barrier can be thought of as a physical barrier – disrupting the mean free path.

For the microscopic zeolite pore system, the confining zeolite network presents a potential field with which the gas molecule constantly interacts and essentially the molecule hops from one adsorption site to another – one can think of the zeolite crystallite as a network of favourable energy locations separated by energetic barriers. Weisz [73] introduced this as the configuration diffusion model, comparable to the model for diffusion of molecules adsorbed onto surfaces. Compared to the Knudsen regime, here, much smaller changes in the confining environment will cause much greater changes in the diffusional behaviour. Xiao and Wei present a model for the configurational regime [74] where molecules are viewed as either retaining there gaseous character but being restricted from moving between sites by energy barriers presented by the confining channels or the gaseous nature is assumed lost and the molecule is considered to be harmonically bound at a site of minimum energy, vibrating with the solid lattice leading to its accumulation of energy. Essentially there is a transition from the Knudsen regime to solid regime where the "gas translation" model is an intermediary stage in terms of the effects of confinement.

There is a wealth of literature on the study of adsorption and diffusion of various gases within different zeolite frameworks encompassing many different approaches, in terms of both simulation and experiment. The calculation of adsorption enthalpies, as a starting point for understanding diffusion in zeolite, is the topic of chapter 2 and so some key trends are now discussed in terms of the data given in table 1.1.

As shown in table 1.1(a), the adsorption enthalpies of n-alkanes increase with chain length in all of the three zeolites considered. This increase does not, however, occur at the same rate for all three zeolites. Comparing the two data sets shown for the different alkane-zeolite pairings (where possible) demonstrates the dependency of the actual enthalpy value obtained on the choice of method, however, the same general trend is observed for each set, and this trend is something that is in fact widely observed. Another trend of interest is that varying the Si/Al ratio of silicalite, to form the structurally equivalent zeolite H-ZSM-5, has a much greater consequence for alcohol molecules compared to alkanes.

Table 1.1(b) gives the adsorption enthalpies for different isomers of pentane and octane. For each zeolite the enthalpy is seen to decrease as the amount of branching increases (again, a widely accepted result). The extent of this variation is again zeolite dependent, occurring to a greater degree for zeolite beta, the channel structure of which is markedly different to the zeolite Y cage structure.

Molecule	Zeolite (Si/Al ratio) Reference is [64] unless otherwise stated		
	Silicalite (purely siliceous)	H-ZSM-5 (Si/Al = 23)	Zeolite Y (Si/Al = 100)
Ethane	36.5	41.7	25.7
	29.0 [75]	37.5 [75]	21.3 [75]
Pentane	78.6	92.2	57.9
			48.0
Octane	118.5	130.8	67.6
			68.0
Methanol	65 [76]	115 [76]	
Ethanol	70 [76]	130 [76]	

(a)

Molecule	Zeolite (Si/Al ratio) Reference is [77]	
	Zeolite Y (Si/Al = 2.7)	Zeolite Beta (Si/Al = 12)
Pentane	39.4	53
2-methylbutane	39.2	51
Octane	57.5	82.9
2-methyleptane	57.2	81.2
2,2,4-trimethylpentane	56.8	73.4

(b)

Table 1.1: Adsorption enthalpies from literature

As has been discussed, there is a well verified trend for adsorption enthalpies of n-alkanes in zeolites (increasing as the chain length increases). The corresponding trend for diffusivity variation is often reported to be a decrease in the rate of diffusion with

chain length. However, in the case of diffusion, exceptions to this general trend are much more prevalent both in terms of particular guest-molecule instances, which might arise from resonant chain lengths correlating with particular channel lengths/ intersection spacing, and also in terms of a different trend entirely being observed for a particular zeolite. The main conclusion here is that the picture of diffusion is much more complicated. A detailed review of diffusion in zeolites is in fact given in chapter 3 but here this point is illustrated in figure 1.1(a), which shows the expected trend, and 1.1(b), which shows cases of diversion from this trend.

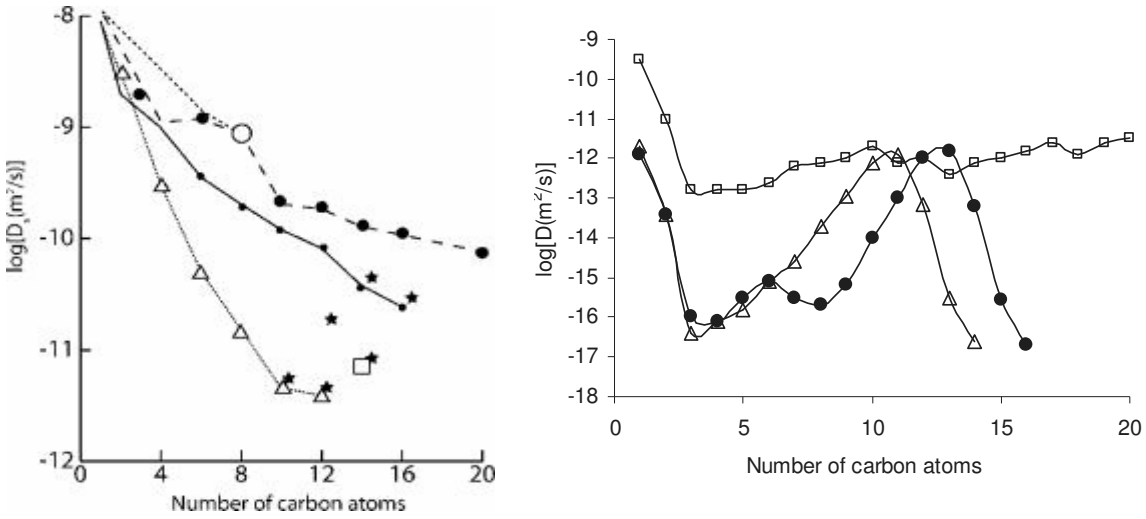

(a) (b)

Figure 1.1: Diffusion coefficients from literature. (a) Self-diffusion coefficients of the n-alkanes in MFI as a function of chain length at 300K as obtained by various techniques: ●, molecular simulations, Δ, PFG-NMR, □. QENS. The asterisks correspond to extrapolations to 300K. (Figure based on data from reference [78][79]). (b) Simulated Diffusion coefficients in zeolites ●. ERI, Δ. CHA, and □. LTA as a function of chain length at 605 K [80][81] .

For the scale of the sensing layer and the larger zeolite pore system, the diffusional behaviour most likely shares aspects of the Knudsen regime and the configurational and surface regimes and the effective diffusivity, discussed in section 1.1.4, will be a function of these particular forms for diffusivity and the porosity and tortuosity of the system.

(1.4) Summary

From the above discussion, to select a suitable metal oxide for a particular task, we must consider a variety of chemical properties such as phase composition, bulk stoichiometry and doping and also geometrical properties such as grain size, porosity and grain network.
The actual fabrication procedure will be crucial to sensor performance – the method of forming the film and the temperatures at which these processes are carried out, for example, are directly linked to many aspects of the microstructure. Also there are factors to consider in the larger-scale design of the device – the electrode positioning and their composition, sensing layer thickness and inclusion of a transformation element which might be included either as a separate layer or admixed within the sensing material. Operational conditions, such as operating temperature and the concentrations of target gas and carrier gas such as air will also be significant.

In rationalising and predicting effects of fabrication and operational choices on the sensor response there are clearly a great number of factors to consider. These different aspects of the response mechanism, which occur on different length scales, are all intimately linked making it particularly difficult to develop a description of the sensor behaviour. The ideal would be to have a model that could predict how the different properties should be chosen to optimise the sensor for a specific sensing task, however, the complexity of the interdependencies of different factors means there exists no rigorous quantitative theory for predicting sensor response.

This said, many models exist that successfully describe certain behavioural aspects although it is clear that there is a necessary compromise between system size and level of detail – a familiar predicament of computational modelling. Approximations are unavoidable and some of the value of the work here will be in evaluating which approximations are most suitable to make.

(1.5) Thesis overview

The aims of the work presented here, to be achieved by the application of computational methods, include characterisation of sensor response dependency on diffusion and reaction of gas through the porous device and how the microstructure and macroscopic design can be tailored, based on these characterisations, to increase sensor

selectivity. It is also considered how a zeolite transformation layer may enhance the selectivity, again in terms of the diffusion-reaction properties. A key premise here is the difficulty of simultaneously modelling a range of different behaviour occurring on different spatial scales and the need for compromise in any theoretical or computational model, between the size of the system modelled and the level of detail included. Following this, three principle methodologies are adopted.

Firstly, in chapter 2, atomistic level force-field calculations are used to calculate adsorption strengths of different molecules within six siliceous zeolite frameworks, the aim is to identify shape and size correlations between the adsorbate vs. framework geometries and the adsorption strength. First principle (density functional theory) calculations have also been performed to investigate the importance of the presence of ions within the zeolite system. The aim of this chapter is to investigate adsorption strength as a potential indicator of the suitability of a particular zeolite for a particular gas sensing task. Some comparison is made with experimental results of zeolite-modified sensor response.

In chapter 3, gas transport is considered more directly; firstly a review being given of diffusion in zeolites. Confinement on a larger scale and its affect on diffusion are then considered. This is relevant for transport occurring both through the sensor and the zeolite layer. Following the method of diffusion eigenstates, a model has been developed which takes an input of zeolitic diffusivity, which could be obtained from one of the previously discussed methods, and a measure of the preference of the gas for being in the zeolite compared to the pore phase and calculates the bulk phase diffusivity in response to varying the geometrical properties of the zeolite-pore system. The occurrence of a phase-dependent reaction may also be modelled and bulk-effective rate constants found. The behaviour of a model sensor system has also been investigated, represented as a construction of impenetrable grains at the surface of which a reaction may occur.

It is then considered in chapter 4, how variable bulk diffusivities and rate constants of the zeolite and sensor layers actually relate to the sensor response. A simple macroscopic model of the composite sensor device is considered consisting of two layers of different diffusivity and rate constant. The transient concentration through the

device is then found using the method of finite differences and from this the response is calculated. Following this, the effect of varying macroscopic features such as the electrode spacing as well as the relative diffusion-reaction properties of the sensor and zeolite layers are investigated.

Finally in chapter 5, further comparisons to experiment are made which support the proposed theories of previous chapters. The conclusions of the work, including the predictive potential of such methods, and routes of future development are then discussed.

References

[1] D. E. Williams, Sens. Actuators B 57 (1999) 1-16. "Semiconducting oxides as gas-sensitive resistors."

[2] M. Vilaseca, J. Coronas, A. Cirera, A. Cornet, J.R. Morante, J. Santamaria, Catalysis Today 82 (2003) 179-185. "Use of zeolite films to improve the selectivity of reactive gas sensors."

[3] D.E. Williams, S. R. Aliwell, K.F.E. Pratt, D.J. Caruana, R.J. Jones, R. A. Cox, G.M. Hansford, J. Halsall, Meas. Sci. Technol. 13 (2002) 923–931."Modelling the response of a tungsten oxide semiconductor as a gas sensor for the measurement of ozone."

[4] G. Korotcenkov, V. Golovanov, V. Brinzari, A. Cornet, J. Morante, M. Ivanov, J. Phys 15 (2005) 256-261. "Distinguishing feature of metal oxide films' structural engineering for gas sensor applications."

[5] G.F. Fine, L.M. Cavanagh, A. Afonja, R. Binions, Sensors, 10 (2010) 5469-5502 "Metal oxide semi-conductor gas sensors in environmental monitoring."

[6] J.W. Gardner, Sens. Actuators B, 4 (1991) 109-115. "Detection of vapours and odours from a multisensor array using pattern recognition Part I. Principal component and cluster analysis."

[7] D.E. Williams in: P.T. Moseley, B.C. Tolfield (Eds.) "Solid state gas sensors" Adam Hilger, Bristol (1987) chpt 5.

[8] (a) A. Rothschild, S. J. Litzelman, H. L. Tuller, W. Menesklou,
T. Schneider, E. Ivers-Tiffee, Sens. Actuators B, (2005) 223–230.
Temperature-independent resistive oxygen sensors based on SrTi1−xFexO3−δ solid solutions.
[8] (b) S. J. Litzelman, A. Rothschild, H. L. Tuller, Sens. Actuators B, (2005) 231–237.
The electrical properties and stability of SrTi0.65Fe0.35O3−δ thin films for automotive oxygen sensor applications.

[9] D. Kohl, J. Phys. D, 34 (2001) 125-149. "Function and applications of gas sensors."

[10] N. Taguchi, United States Patent 3,631,436, 4th July, 1970.

[11] N. Barsan, U. Weimar, J. Electroceramics, 7, (2001), 143. "Conduction Model of Metal Oxide Gas Sensors."

[12] G. Korotcenkov, Materials science and engineering B 139 (2007) 1-23. “Metal oxide for solid-state gas sensors: What determines out choice?”

[13] K. Sahner, R. Moos, Phys. Chem. Chem. Phys., 9 (2007) 635–641. “Modelling of hydrocarbon sensors based on p-type semiconducting perovskites.”

[14] K. Sahner, R. Moos, M. Matam, J.J. Tunney, M. Post, Sens. Actuators B 108 (2005) 102–111. “Hydrocarbon sensing with thick and thin film p-type conducting perovskite materials.”

[15] D. Niemeyer, D.E Williams, P. Smith, K. F. Pratt, B. Slater, C.R.A Catlow, A.M. Stoneham, J. Mater. Chem., 12 (2002) 667–675. “Experimental and computational study of the gas-sensor behaviour and surface chemistry of the solid-solution Cr2-xTixO3 ($x \leq 0.5$).”

[16] S. Pokhrel, C.E. Simion, V. Quemener, N. Bârsan, U. Weimar, Sens. Actuators B, 133 (2008) 78-83. “Investigations of conduction mechanism in Cr2O3 gas sensing thick films by ac impedance spectroscopy and work function changes measurements.”

[17] N. Barsan, C. Simion, T. Heine, S. Pokhrel, U. Weimar, J. Electroceram. 25 (2009) 11-19 “Modelling of sensing and transduction for p-type semiconducting metal oxide based gas sensors.”

[18] D. E. Williams, P.T. Moseley, J. mater. Chem., 1 (1991), 809-814. “Dopant effects on the response of gas-sensitive resistors utilising semiconducting oxides.”

[19] A. Gurlo, M. Sahm, A. Oprea, N. Barsan, U. Weimar, Sens. Actuators B 102 (2003) 291-298. “A p- to n-transition on α-Fe_2O_3-based thick film sensors studied by conductance and work function change measurements.”

[20] T. Wolkenstein, “Electronic processes on semiconductor surfaces during chemisorption”, Consultants Bureau, New York (1991).

[21] A. Rothschild, Y. Komem, Sens. Actuators B 93 (2003) 362-369. “Numerical computation of chemisorption isotherms for device modelling of semiconductor gas sensors.”

[22] S. Strassler, A. Reis, Sens. Actuators 4 (1983) 465-471. “Simple models for n-type metal oxide gas sensors.”

[23] S. Chang, J. Vac. Sci. Technol., 17 (1980) 366-369. “Oxygen chemisorption on tin oxide: correlation between electrical conductivity and EPR measurements.”

[24] P. Mark, J. Phys. Chem., 29 (1968) 689-697. “Chemisorption states of ionic lattices.”

[25] A. Gurlo, chem.phys.chem., 7 (2006) 2041-2051. “Interplay between O_2 and SnO_2: Oxygen Ionosorption and Spectroscopic Evidence for Adsorbed Oxygen.”

[26] P.K. Clifford, D.T. Tuma, Sens. Actuators, 3 (1983) 233-254. “Characteristics of semiconductor gas sensors I. Steady state gas response.”
[27] D. E. Williams, K.F.E. Pratt, Sens. Actuators B, 70 (2000) 214-221. “Microstructure effects on the response of gas-sensitive resistors based on semiconducting oxides.”

[28] T.A. Jones, in: P.T. Moseley, B.C. Tolfield (Eds.) “Solid state gas sensors” Adam Hilger, Bristol (1987) chpt 4.

[29] C. Xu, J. Tamaki, N. Miura, N. Yamazoe, Sensors and Actuators B, 3 (1991) 147–155. “Grain size effects on gas sensitivity of porous SnO_2-based elements.”

[30] J. electrochem. Soc., 141 (1994) 2207-2210. “Grain-Size Effects in Tungsten Oxide-Based Sensor for Nitrogen Oxides.”

[31] G. Zhang, M. Liu, Sens. Actuators B, 69 (2000) 144–151. “Effect of particle size and dopant on properties of SnO 2 -based gas sensors.”

[32] V. Brinzari, G. Korotcenkov, V. Golovanov, Thin Solid Films, 319 (2001) 167-175. “Factors influencing the gas sensing characteristics of tin dioxide films deposited by spray pyrolysis: understanding and possibilities of control.”

[33] N. Yamazoe, K. Shimanoe, Sens. Actuators B 128 (2008) 566-573. “Theory of power laws for semiconductor gas sensors.”

[34] S. Kirkpatrick, Rev Mod. Phys., 45 (1973) 574-588. “Percolation and conductance.”

[35] M. Ulrich, A. Bunde, C. Kohl, Applied Physics Letters, 85 (2004) 242-244. “Percolation and gas sensitivity in nanocrystalline metal oxide films.”

[36] V.Y. Sukharev, J. Chem. Soc. Faraday Trans., 89 (1993) 574-588. “Percolation Model of Adsorption-induced Response of the Electrical Characteristics of Polycrystalline Semiconductor Adsorbents.”

[37] G. Chabanis, I. P. Parkin and D. E. Williams, Meas. Sci. Technol. 14 (2003) 76–86. “A simple equivalent circuit model to represent microstructure effects on the response of semiconducting oxide-based gas sensors.”

[38] S.C. Naisbitt, K.F.E. Pratt, D.E. Williams, I.P. Parkin, Sens. Actuators B, 114 (2006) 969–977. “A microstructural model of semiconducting gas sensor response: The effects of sintering temperature on the response of chromium titanate (CTO) to carbon monoxide.”

[39] E. Llobet, J. Brezmes, X. Vilanova, J.E. Sueiras, X. Correig, Sensors and Actuators B, 41 (1997) 13-21. “Qualitative and quantitative analysis of volatile organic compounds using transient and steady-state responses of a thick-film tin oxide gas sensor array.”

[40] G. Sakai, N. Seok Baik, N. Miura, N. Yamazoe, Sensors and Actuators B, 77 (2001) 116-121. “Gas sensing properties of tin oxide thin films fabricated from hydrothermally treated nanoparticles. Dependence of CO and H_2 response on film thickness.”

[41] X. Vilanova, E. Llobet, R. Alcubilla, J.E Sueiras, X. Correig, Sens. Actuators B, 31 (1996) 175-180. “Analysis of the conductance transient in thick-film tin oxide gas sensors.”

[42] Y. Shimizu, Y. Nakamura, M. Egashira, Sens. Actuators B, 13-14 (1993) 128-131. “Effects of difisivity of hydrogen and oxygen through pores of thick film SnO,-based sensors on their sensing properties.”

[43] D.E. Williams, K.F.E. Pratt, J. Chem. Soc. Faraday Trans., 1995, 91(13), 1961-1966. “Theory of self diagnostic sensor array devices using gas-sensitive resistors.”

[44] P. Ingleby, J.W. Gardner, P.N. Bartlett, Sens. Actuators B, 57 (1999) 17-27. “Effect of micro-electrode geometry on response of thin-film poly(pyrrole) and poly(aniline) chemoresistive sensors.”

[45] D.E. Williams, K.F.E. Pratt, J. Chem. Soc, Faraday Trans., 92 (1996) 4497-4504. “Resolving combustible gas-mixtures using gas sensitive resistors with arrays of electrodes.”

[46] D.E. Williams, G.S. Henshaw, K.F.E. Pratt, J. Chem. Soc. Faraday Trans., 91 (1995) 3307-3308. “Detection of sensor poisoning using self-diagnostic gas sensors.”

[47] D.E. Williams, R. Peat, G.S Henshaw, K.F.E Pratt, J. Chem. Soc, Faraday Trans., 91 (1995) 4299-4307. “Reaction-Diffusion Effects and Systematic Design of Gas-sensitive Resistors based on Semiconducting Oxides.”

[48] J.W. Gardner, Sens. Actuators, 18 (1989) 373-387. “Electrical conduction in solid-state gas sensors.”

[49] J.W. Gardner, P.N. Bartlett, Sens. Actuators B 18-19 (1994) 211-220. “A brief history of electronic noses.”

[50] A. Carrasco, C. Saby, P. Bernadet, Flavour Fragrance J., 13 (1998) 335-348. “Discrimination of Yves Saint Laurent perfumes by an electronic nose.”

[51] R. Dutta, E.L. Hines, J.W. Gardner, K,R. Kashwan, M. Bhuyan, Sens. Actuators B 2 (2003) 228-237. “Tea quality prediction using a tin oxide-based electronic nose: an artificial intelligence approach.”

[52] J.W. Gardner, H.V. Shurmer, T.T. Tan, Sens. Actuators B, 6 (1992) 71-75. “Application of an electronic nose to the discrimination of coffees.”

[53] J. Brezmes, E. Llobet, X. Vilanova, G. Saiz, X. Correig, Sens. Actuators B, 69 (2000) 223-229. “Fruit ripeness monitoring using an Electronic Nose.”

[54] J.W. Gardner, P.N. Bartlett, “Electronic noses, principles and applications” Oxford university press, Oxford (1999).

[55] R.E. Baby, M. Cabezas, E.N. Walsoe De Reca, Sens. Actuators B, 69 (2000) 214-218. “Electronic nose: a useful tool for monitoring environmental contamination.”

[56] A.P.F. Turner, N. Magan, Nat. Rev. Microbiol., 2 (2004) 1-6. “Electronic noses and disease diagnostics.”

[57] R. Dutta, D. Morgan, N. Baker, J.W. Gardner, E.L. Hines, Sens. Actuators B, 109 (2005) 355-361. “Identification of *Staphylococcus aureus* infections in hospital environment: electronic nose based approach.”

[58] R.F. Machado, D. Laskowski, O. Deffenderfer, T. Burch, S. Zheng, P.J. Mazzone, T. Mekhail, C. Jennings, J.K Stoller, J. Pyle, J. Duncan, R.A. Dweik, S.C Erzurum, AJRCCM, 171 (2005) 1286-1291. “Detection of lung cancer by sensor array analyses of exhaled breath.”

[59] R Muller, E. Lange, Sens. Actuators, 9 (1986) 39. “Multidimensional sensor for gas analysis.”

[60] J.W. Gardner, Sens. Actuators B, 4 (1991) 109-115. “Detection of vapours and odours from a multisensor array using pattern recognition Part I. Principal component and cluster analysis.”

[61] J.W. Gardner, E.L. Hines, M. Wilkinson, Meas. Sci. Technol., 1 (1990) 446-451. “The application of artificial neural networks in an electronic nose.”

[62] L.B. McCusker, Ch. Baerlocher, D.H. Olson, “Atlas of zeolite framework types” Elsevier, Amsterdam (2007).

[63] J.W. McBain, “The sorption of Gases and Vaporous by solids” Rutledge and Sons, London (1931) Chapter 5.

[64] J.O. Titiloye, S.C. Parker, F.S. Stone, C.R.A. Catlow, J. Phys. Chem., 95 (1991) 4038-4044. “Simulation studies of the structure and energetics of sorbed molecules in high-silica zeolites. 1. Hydrocarbons.”

[65] R. Krishna, B. Smit, S. Calero, Chem. Soc. Rev., 31 (2002) 185-194. “Entropy effects during sorption of alkanes in zeolites.”

[66] I. Papai, A. Goursot. F. Fajula, J. Phys. Chem., 99 (1995) 12925-12932. “Modelling of N_2 and O_2 adsorption in zeolites.”

[67] N.Y, Chen, T.F. Degnan, C. Morris-Smith, “Molecular transport and reaction in zeolites: Design and application of shape selective catalysis”, VCH Publishers, New York (1994) chpt 8.

[68] X. Xu, J. Wang, Y. Long, Sensors, 6 (2006) 1751-1764. “Zeolite-based materials for gas sensors.”

[69] O. Hugon, M. Sauvan, P. Benech, C. Pijolat, F. Lefebvre. Sens. Actuators B, 67 (2000) 235-243. “Gas separation with a zeolite filter, application to the selectivity enhancement of chemical sensors.”

[70] M. Vilaseca, J. Coronas, A. Cirera, A. Cornet, J. Morante, J. Santamaria, Sensors And Actuators B, 124 (2007) 99-110. “Gas detection with SnO 2 sensors modified by zeolite films.”

[71] K. Sahner, D. Schönauer, P. Kuchinke, R. Moos. Sens. Actuators B, 133 (2008) 502-508. “Zeolite cover layer for selectivity enhancement of p-type semiconducting hydrocarbon sensors.”

[72] D. P. Mann, K. F. E. Pratt, T. Paraskeva, I. P. Parkin, and D. E.Williams. J. IEEE Sens., 7 (2007) 551-556. “Transition Metal Exchanged Zeolite Layers for Selectivity Enhancement of Metal-Oxide Semiconductor Gas Sensors.”

[73] P.B. Weisz, Pure & Appl. Chem., 52 (1980) 2091-2103. “Molecular shape selective catalysis.”

[74] J. Xiao, J. Wei, Chem. Eng. Sci., 47 (1992) 1123-1141. “Diffusion mechanism of hydrocarbons in zeolites - I. Theory.”

[75] H. Stach, U. Lohse, H. Thamm, W. Schinner, Zeolites, 6 (1986) 74-90. “Adsorption equilibria of hydrocarbons on highly dealuminated zeolites.”

[76] C.-C. Lee, R. J. Gorte, W. E. Farneth, J. Phys. Chem. B, 101 (1997) 3811-3817. “Calorimetric Study of Alcohol and Nitrile Adsorption Complexes in H-ZSM-5.”

[77] J. F. Denayer, W. Souverijns, P. A. Jacobs, J. A. Martens, G. V. Baron, J. Phys. Chem. B, 102 (1998) 4588-4597. “High-Temperature Low-Pressure Adsorption of Branched C5-C8 Alkanes on Zeolite Beta, ZSM-5, ZSM-22, Zeolite Y, and Mordenite.”

[78] B. Smit, T. L. M. Maesen, Chem. Rev., 108 (2008) 4125–4184. “Molecular Simulations of Zeolites: Adsorption, Diffusion, and Shape Selectivity.”

[79] H. Jobic, D.N. Theodorou, J. Phys. Chem. B, 110 (2006) 1964-1967. “Diffusion of Long n-Alkanes in Silicalite. A Comparison between Neutron Scattering Experiments and Hierarchical Simulation Results.”

[80] D. Dubbeldam, S. Calero, T.L.M. Maesen, B. Smit, Phys. Rev. Lett., 90 (2003) 245901-246100. “Incommensurate Diffusion in Confined Systems.”

[81] D. Dubbeldam, B. Smit, J. Phys. Chem. B, 107 (2003)12138-12137. “Computer Simulation of Incommensurate Diffusion in Zeolites: Understanding Window Effects.”

Chapter 2: Adsorption of gases in zeolites.

(2.1) Introduction

To make effective use of the catalogue of naturally occurring and synthetic zeolites available, for enhancing gas sensor selectivity, it would be highly desirable to have some sort of predictive tool that could indicate a suitable choice of zeolite for a particular sensing task. As discussed in the previous chapter, the zeolite transformation layer presents a barrier through which the transport depends on both macroscopic and microscopic properties of the layer formation. In this chapter the microscopic level is considered. Due to the molecular scale confinement of gas within the zeolite microstructure, it is proposed that there may be molecule dependent transport i.e. favoured transport of one molecule over another through the zeolite layer, hence the introduction of selectivity when the zeolite is combined as part of the sensor design. The generally accepted (though poorly understood) picture of diffusion within zeolites is that molecules hop between adjacent adsorption sites under the influence of the potential field of the zeolite framework (and other sorbed molecules). One essentially needs to determine the initial strength of adsorption of the molecule onto the zeolite surface, which is investigated in the course of this chapter; the energetic barrier that the adsorbate faces to move to another site and then try to associate with this a time scale over which the hopping process occurs.

Due to the vast number of zeolites available (to be tested against many possible sorbates), computational methods clearly have an advantage for testing such dependencies due to the relative ease of application. There exist a number of models that have proved successful in providing insight into adsorption in zeolites [1][2] and these are generally classed as being either classical force-field based or based on first principles. The latter approach provides a more detailed picture of the electronic structure but is greatly more computationally demanding and hence limited in the size of the system that can be modelled compared to the force-field approach.

.

Here a classical force-field approach is used to probe the dependency of the strength of adsorption on the comparative dimensions of the sorbate and the zeolite pore. Six siliceous zeolite frameworks are considered, chosen to include an appropriate cross-section of the pore and channel structures that typically arise. Adsorption strengths of

molecules of different size and shape – for example linear and branched alkanes – are calculated with an aim of identifying patterns which could be indicative of potential discriminatory capacity. Another contributor to the strength of adsorption is the presence of ions within the zeolite framework. In light of this, a quantum mechanics based approach is proposed to explore sorbate-ion interaction within the presence of a simple zeolite cluster.

The merit of these methods and the suitability of the calculation of adsorption strengths in general as a predictive tool in selecting a suitable zeolite for a gas sensing task are discussed and observations made from these calculations are compared with experimental results of sensor response.

(2.2) Computational models for gas adsorption in zeolites

The strength of adsorption can be defined as the difference between the energies of the zeolite (E_z) and gas molecule (E_g) separately and the energy of the system in which the molecule has been adsorbed onto the zeolite surface (E_{z+g}). At zero Kelvin this is the binding energy (E_{be}) given by:

$$E_{be} = (E_z + E_g) - E_{z+g} \qquad \text{Equation 2.1}$$

(Defined such that the more positive the value of E_{be}, the more strongly bound the molecule)

To take into account a finite temperature, where there will be a distribution of molecular energy over different sites, the change in enthalpy is a more appropriate quantity and one considers the difference in the enthalpy of the molecule from an external (infinitely dilute) reservoir (H_g) and of the molecule within the zeolite framework (H_z). This is known as the isosteric heat of adsorption, a function of both temperature and concentration (q_{zg}):

$$q_{zg} = H_g - H_z \qquad \text{Equation 2.2}$$

A positive value indicates that the framework is favoured over a reservoir and hence the molecule will be adsorbed. Equations 2.1 or 2.2 can then be evaluated following one of the approaches now discussed

1. Atomistic force-field calculations:

The potential energy of the system is determined by a functional form comprised of (classical) representations of different discrete, localized interactions occurring between the atoms of the system. The function can be computed at any point in configuration space – which is defined to be the 3N-dimensional space spanned by the 3N Cartesian coordinates of the N-particle system.

Both bonded and non-bonded terms are included, bonds are represented typically by a simple harmonic oscillator and the non-bonded components include an electrostatic contribution, modelled using Coulomb's law, and a Van der Waals term represented with a Lennard-Jones potential. Parameters required to represent these interactions are taken from experiment and from higher level calculations.

Atoms are assigned a value for charge and charge polarisability, and whilst parameters may be taken from first principle calculations, no further detail of the electronic contribution to energy is accounted for as part of the force-field calculation. The lack of any detailed electronic input does limit the use of force-field methods when it comes to studying interactions where electronic redistribution occurs. Hence bond based methods are generally best suited to the study of siliceous zeolites.

With an expression for the system energy in hand, energy minimisation (EM) methods such as conjugate gradient and Newton-Raphson can be applied [3] to find the atomic positions giving the lowest energy. EM alone does not guarantee that the minimum found is the true, global minimum of the system and is better used in conjunction with a Monte Carlo (MC) simulation [3][4] which can facilitate efficient sampling of the configuration space. The basis of the MC simulation technique for this application is the generation of an ensemble of configurations (a Markov chain) for the system of interest. A new configuration is generated by random displacement steps or the creation or deletion of molecules. Through the course of the simulation, new configurations are generated and accepted if the energy of the system has been reduced. If the energy has not been reduced then, assuming the system obeys Boltzmann statistics, the configuration is accepted with probability P:

$$P = \exp\left(\frac{-\Delta U}{K_B T}\right)$$

Where U is the internal energy, K_B is the Boltzmann constant and T is the system temperature.

Sophisticated models have been developed that use biasing techniques (for example configurational biasing for insertion of sorbates into dense systems) to dramatically reduce the computational effort of probing the energy landscape of complex systems: see for example [1].

These types of calculation can comfortably model atom numbers on the scale of multiple zeolite unit cells i.e. around 100,000 atoms. Large zeolite systems can be simulated using their unit cell structure along with periodic boundary conditions.

2. Ab initio calculations:

Ab initio or first principle methods take into account the quantum chemical behaviour of the system. Density functional theory (DFT) is one particular vein of quantum methods and is the focus of the discussion here. DFT is a highly regarded tool in the field of quantum chemistry with a good level of accuracy achievable (observed through correlation with experimental data) for relatively low computational cost (compared to, for example, Hartree Fock methods with electron correlation treatments).

In DFT the total energy is expressed as a functional of the charge density [5] – in turn a function of the molecular orbitals of the system – rather than in terms of the many-body wave function itself as in other standard quantum mechanical formalisms. An expression for the energy can be formed, as in equation 2.3, by considering the different energetic contributions namely the kinetic energy, T, and electrostatic energy from nuclei-electron attraction, U, and electron-electron repulsion. The repulsion between electrons can be thought of as having a Coulombic contribution – which can be included in the form of U – and an exchange-correlation term E_{xc}.

$$E[\rho] = T[\rho] + U[\rho] + E_{xc}[\rho] \qquad \text{Equation 2.3}$$

The total energy is optimised with respect to variations in the density to give the Kohn-Sham equations [6]. DFT then follows an iterative, self-consistent process, solving the Kohn-Sham equations until convergence of the density function is achieved, at which point the total energy can be evaluated. The form for E_{xc} requires some approximation for computation to be feasible, the choice of exchange-correlation approximation and of the basis sets being what really set apart different DFT models.

Here the DMol^3 [7][8] software is used, a key feature of which is the use of numerical basis functions – regarded as a particularly reliable approach due, for example, to the

minimisation of basis set superposition error [9]. DMol^3 offers several different approximations for the exchange-correlation function, defined as either being a local density approximation (LDA) where the electron density is effectively assumed to be uniform by considering only the density at the point where the functional is evaluated. Alternatively the approximation can be improved by including the gradient at this point, known as a generalised gradient approximation (GGA).

Whist a much more detailed picture can be formed than with the force-field model, the size of the system that can be simulated is much smaller. However, as a rapidly developing field and with ever-increasing computing resources available, first principle methods will certainly be much more applicable to larger systems in the near future [10].

(2.3) Force-field simulation details

(2.3.1) Overview

Calculations have been carried out to find the location of favourable adsorption sites and the binding strength at sites using a combination of energy minimisation and Monte Carlo based simulation techniques via the Materials Studio simulation platform [11]. Materials studio is a compilation of advanced materials simulation and modelling software, its core module being the materials visualizer in which molecular structures, including an extensive library of zeolites, can be examined and modified.

The principal simulation engine for Materials studio modelling is Discover [11] which here has been used to carry out energy minimization and single point (fixed geometry) energy calculations. Discover uses the "CFF" consistent force-field functional form and here the COMPASS force-field has been used throughout. COMPASS [12] (Condensed-Phase Optimized Molecular Potentials for Atomistic Simulation Studies) is considered to be a 'high quality and general force-field' of well validated parameters suitable to investigate a range of different molecules. Importantly, this *ab initio* force-field enables accurate prediction of gas-phase and condensed phase properties simultaneously which is clearly advantageous here. COMPASS is also compatible with the Sorption module discussed below.

All CFF force-fields have the same general functional form which includes non-bond terms, terms for the deformation of bond lengths, bond angles, torsion angle and out of plane interactions. The non-bond energy is the sum of the pair wise additive potential for the steric and electrostatic interactions of the form:

$$e_{ij} = \varepsilon[(\frac{r^*}{r})^9 - 2(\frac{r^*}{r})^6] + \frac{q_i q_j}{\varepsilon r_{ij}}$$

Where the electrostatic interactions are represented by the standard Coulomb form and the Van der Waal interactions are represented by the Lennard-Jones potential but with a 9^{th} power repulsive term rather than the more usual 12^{th} power term (this does not have any physical significance but rather arises due to computational convenience).

The Sorption [11] module of Materials Studio has been developed specifically for the task of sorption within a 3-dimensional periodic structure such as a zeolite framework and here has been used to load sorbate gas molecules into different zeolite structures at their preferred binding sites. Sorption uses a Monte Carlo algorithm for either the grand canonical or canonical ensemble corresponding to fixed pressure and fixed loading calculations respectively. This enables the calculation of binding energies for sorbates at infinite dilution and also the investigation of the effect of sorbate-sorbate interactions by modelling higher loadings. Here another consideration must be made for the evaluation of potential field, namely how to represent the non-bond energy of a periodic system. Sorption uses the Ewald summation technique [13] which involves the use of a Fourier space summation of interaction energies which converges easily compared to the equivalent real space summation.

(2.3.2) Structure preparation

Six zeolite frameworks have been studied in the course of this investigation, all in the siliceous form. These are FER, MOR, MFI, BEA, FAU and LTA; images of the structures, taken from the Materials Studios Visualizer, are shown in figure 2.1 and some key descriptors are given in table 2.1. A useful categorisation for describing the key features of the frameworks relevant to this investigation is that of Beerdsen et. al.[14]. They discuss the diffusion of molecules confined within nanoporous structures such as zeolites and propose a simple classification of zeolites defining three general types as follows:

1. Channel type: 1D channels such as FER and MOR.
2. Intersecting channel type: a regular pattern of the 3D system such as MFI and BEA.
3. Cage-type: cages connected by windows which can be large as with FAU, or small as with LTA.

This categorization does of course depend on the molecule being adsorbed, for example a small molecule in a FER type structure which has side pockets from its main channels, effectively sees a 3D intersecting channel type.

Zeolite structures consisting of one unit cell were imported from the Materials Studio database (unit cell dimensions given in table 2.1) and were converted to P1 symmetry as the Sorption module requires low symmetry structure inputs so as to avoid the symmetry relationships, on which the calculation relies, being violated by the introduction of a gas molecule.

Structures were also converted where necessary into supercell structures to avoid interactions between adsorbed molecules in different unit cells (supercell ranges are also given in table 2.1).

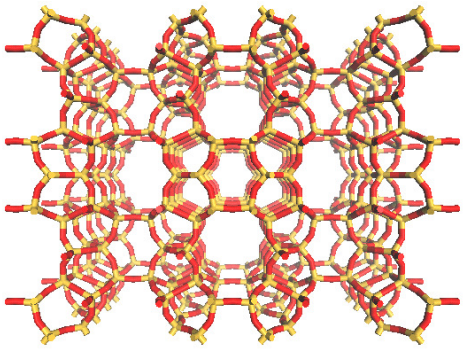

FER viewed along [001]

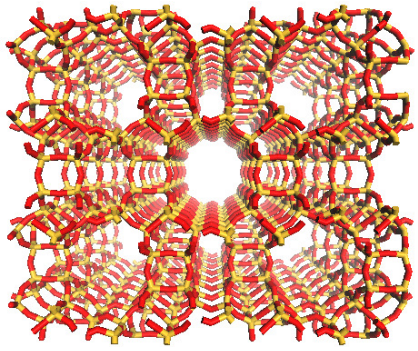

MOR viewed along [001]

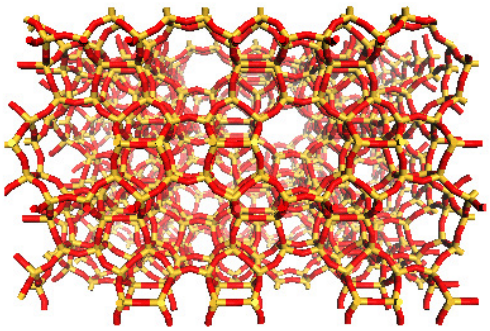

MFI viewed along [100]

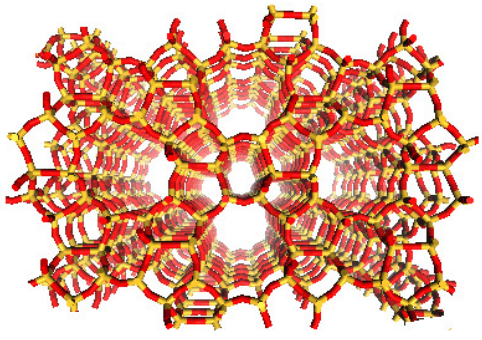

MFI viewed along [010]

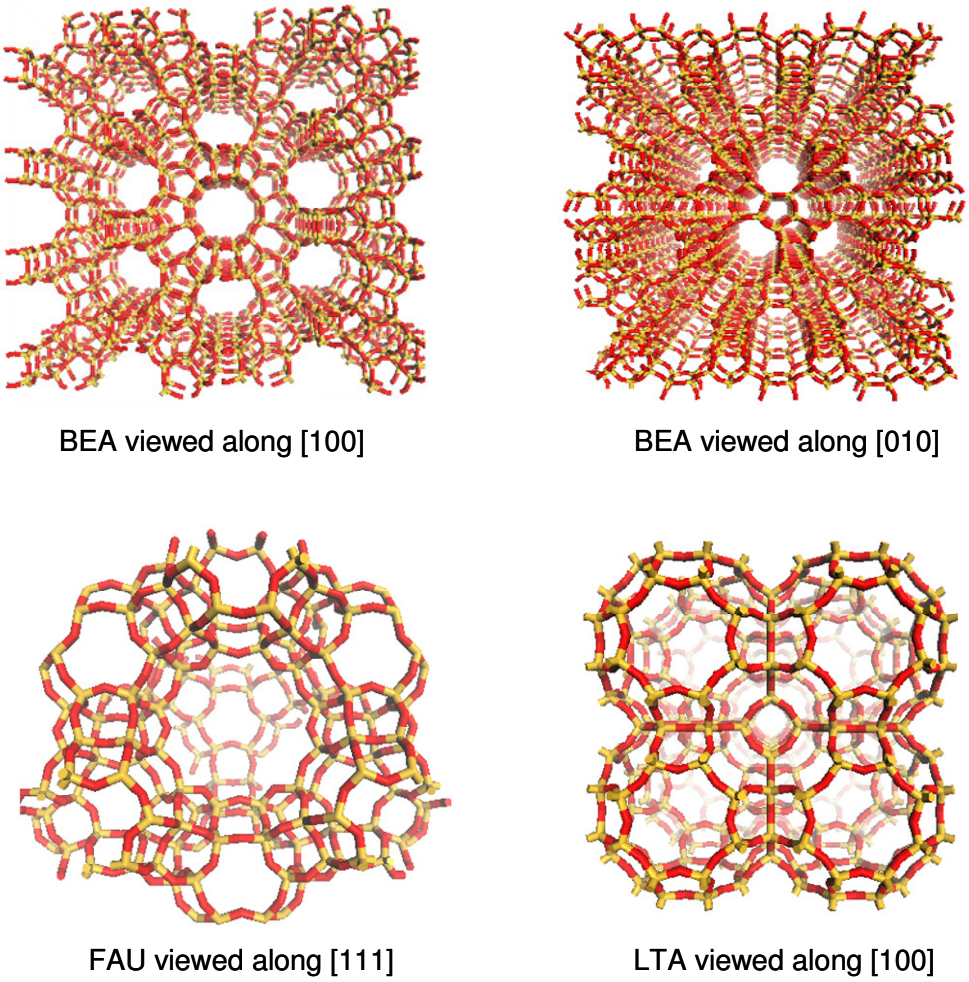

Figure 2.1: Images of the different zeolite frameworks used in the calculations showing the main channel and pore structures. Atoms represented as silicon: yellow, oxygen: red.

The sorbates tested include branched and linear alkanes and alcohols, aromatics, alkenes, amines, CO and NO_2.

Guest molecules where constructed within the Materials Studio Visualizer and then energy minimised through Discover to find E_g from equation 2.1. The optimised structures were then used for the sorption calculations. The 'Smart Minimizer' was used which employs a combination of the Newton-Raphson, conjugate gradient and steepest decent minimisation methods resulting in a highly efficient computational procedure. Note whilst the conjugate gradient method is the most efficient first order method it can be unstable far from the minimum hence the use of the simpler 'steepest descent' method for the beginning steps of the calculation is beneficial.

Zeolite Name	Structure type	Topology	Density T/1000 Å	Unit cell dimensions/ Å	Supercell range	No. oxygen in ring	Ring dimensions/ Å	
							Minimum	Maximum
Ferrierite	FER	Channel	17.8	(38.4, 28.3, 14.9)	(2, 2 ,2)	10 8	4.2 2.5	5.4 4.8
Mordinite	MOR	Channel	17.2	(18.1, 41, 30.1)	(1, 2, 4)	8 12	2.6 6.5	5.7 7
ZSM-5	MFI	Intersecting channel	17.9	(40, 39.8, 26.8)	(2, 2, 2)	10 10	5.1 5.3	5.5 5.6
Beta	BEA	Intersecting channel	15.1	(25.3, 25.3, 26.4)	(2, 2, 1)	12 12	5.6 7.7	5.6 6.6
Y	FAU	Cage	12.7	(25, 25, 25)	(1, 1, 1)	12	7.4	7.4
A	LTA	Cage	12.9	(24.6, 24.6, 24.6)	(1, 1, 1)	8	4.1	4.1

Table 2.1: Details of siliceous zeolite frameworks used in force-field calculations. Minimum and maximum values are given of ring dimension of any molecularly accessible pore structures as these are often not spherical.

Discover requires a system of less than 200 atoms to use the Newton-Raphson method so first-order methods only were used for the later optimisations of the zeolite systems. For all optimisations, a Van der Waals' interaction cut-off distance of 12Å was used and charges were assigned according to the COMPASS typing rules (the charges used in COMPASS are partial charges derived from ab initio methods).

It is useful to consider different characterisations of the zeolite as looking at just one property, such as channel diameter, can be misleading, for example, a cage structure is not well represented as a channel. After the structures were prepared, analysis of the zeolite and also the sorbate structures was performed in part using the QSAR [11] (Quantitative Structure-Activity Relationships) module via the Materials Studio platform. In particular the Atoms Volumes and Surfaces tool was used to calculate zeolite free volumes potentially available to adsorbate molecules. The van der Waals surface of the zeolite structure is firstly constructed and the appropriate volume excluded, a spherical probe particle is then used to analyse the free volume. Clearly the guest molecule will not always be spherical and also no analysis of the truly accessible volume (i.e. whether or not a particle can pass through a restricting window) is made. However, this method does provide a parameter that is insightful when used in conjunction with other descriptors and has the advantage that it is easily generated.
For the sorbates, the heights and widths were calculated as "critical dimensions" as in [15][16], taking angles and bond lengths from $DMol^3$ optimised structures ($DMol^3$ optimisation is discussed in section 2.5) using the measuring tools available in the Visualizer. A van de Waals radii correction was also added for which values were taken from [17]. Note these values should not be considered as infallible as access into a zeolite where otherwise is indicated may still be possible due rotational motion or a change of shape on interaction with the zeolite framework. Therefore in the calculation of binding energies, molecules apparently excluded according to their critical dimensions are still included. The values of critical dimensions are useful, however, in discussion of experimental results of zeolite modified gas sensors. Also dipole moments are given; these were calculated using $DMol^3$ through the QSAR module.

(2.3.3) Infinite dilution calculations

To find the binding energy of a single sorbate molecule within different zeolite supercells, a comparison of the energy of the zeolite with and without the sorbate

molecule (following equation 2.1) must be made. Hence a Sorption fixed loading calculation was executed to find the low energy binding site of one molecule sorbed in each of the zeolites tested. This also gives maximum and minimum values of the isosteric heat of adsorption. The temperature was, for the most part, set as 298K.

The Sorption quality setting was set to "fine" (referring to parameters such as the non-bond cut-off distances). An equilibration stage, in which the system adjusts to the specified temperature, of 10^5 steps precedes the production stage of 10^6 steps. Repeats of calculations showed appropriately small uncertainty associated with the results.

Sorption automatically constrains the lattice structure and for the subsequent energy minimisation calculation, carried out using Discover, the lattice atoms were also constrained. Test calculations using an unconstrained lattice were also performed to check the validity of this using a constrained lattice and the patterns of response were found to be unchanged whereas the computation time was greatly increased.

The Sorption calculations were executed using the standard Metropolis Monte Carlo method described above which is suitable for the study of small molecules. The first stage of the calculation is an insertion stage consisting of 10^5 attempts. Insertion may fail even though the molecule can actually fit into the framework but is tightly fitting. This does restrict the capabilities of the calculations, for example it is difficult to find binding energies of alkanes of chain length longer than 10 using this method.

It should be noted also that Sorption does not sample only the accessible free volume but the whole free volume of the unit cell such that if a molecule should in fact not be able to enter a certain cavity due to the presence of a small intersecting window this is not accounted for in the simulation.

(2.3.4) Higher loadings

In any practical situation, interactions between guest molecules are also going to contribute to the energy landscape either hindering or promoting adsorption of subsequent molecules. Also one would expect that beyond a certain loading, further loading will be greatly hindered as energetically favoured binding sites will no longer be available. The Sorption module can be used to simulate higher loadings either by specifying a loading or a pressure value. Fixed loading calculations were performed for increasing load per unit cell (puc) to assess whether changing the load affects the patterns of binding energy within the different zeolites. The methodology was essentially the same as for the infinite dilution calculations.

(2.4) Results of descriptor and force-field calculations

(2.4.1) Zeolite and sorbate classifications

Figure 2.2 gives the calculated free volume for the different zeolites for different probe radii with zeolites plotted in order of increasing density. MOR and FER in fact have very similar densities and the decrease in free volume from MOR to FER is therefore greater than expected. This is attributed to the narrower channels of the FER framework. A more noticeable departure from this trend of high density and low free volume is MFI which has a much greater free volume than lower density FER, however, this is seen to be strongly dependent on the probe radius, much more so than for the other zeolites and in fact this result is likely indicative of inaccuracy in the calculation.

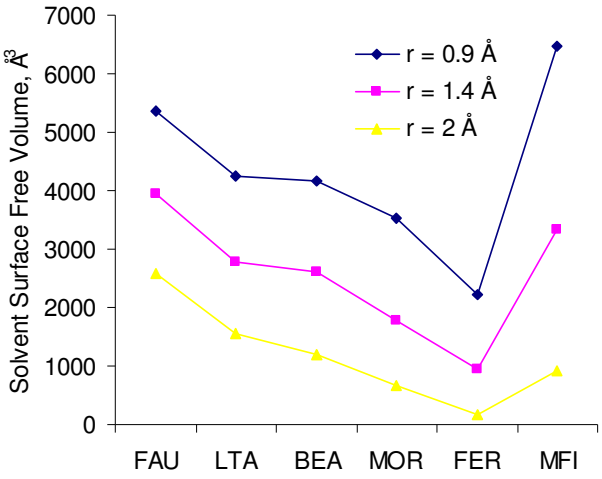

Figure 2.2: Solvent surface free volumes calculated using different solvent radii for the different zeolites studied.

Table 2.2 gives descriptors for the sorbates including critical dimensions of length, width and height and, from comparing these with the dimensions of the channels and windows of the different zeolite frameworks, possible exclusions are proposed. Also given are the calculated dipole moments. Molecules with different functional groups can be ordered according to dipole moment following: alcohols > amines > alkenes > alkanes.

Molecule	Height/ Å	Width/ Å	Length/ Å	Expected Exclusions	Dipole Moment/ D
CO	3.3	3.3	4.2		0.112
NO_2					0.472
Methane	3.8	4.1	3.9		0.000
Propane	4.2	4.6	6.7		0.036
Pentane	4.1	4.6	9.2		0.040
Heptane	4.1	4.5	11.7		0.033
Octane	4.1	4.7	12.9		0.000
Nonane	4.1	4.5	13.3		0.007
Decane	4.1	4.5	14.4		0.000
3-ethylpentane	4.4	6.8	9.2	LTA, MFI, FER	0.027
3-butylpentane	6.7	7.8	10.6	LTA, BEA, MFI, MOR, FER	0.042
Methylbenzene	6.6	4.1	8.3	LTA, MFI, FER	0.528
Propylbenzene	6.6	5.3	10.3	LTA, MFI, FER	0.589
Benzene	6.6	7.3	3.3	LTA, MFI, FER	0.000
Ethylamine	4.2	4.6	6.6		1.467
Propene	4.2	5	6.5		0.341
Ethanol	5.4	4.5	6.4		1.510
Isopropyl	4.5	5.3	6.7	LTA	1.671
Propanol	4.2	4.6	7		1.531

Table 2.2: Key sorbate descriptors.

(2.4.2) Binding Energies – infinite dilution

Here the infinite dilution adsorption behaviour is discussed in terms of binding energy with values given such that a larger positive value indicates a stronger binding strength. The binding energy was found to be equal to the maximum isosteric heat for a low simulated temperature of 298K (the minimum isosteric heat was found to give the same pattern of response). Unlike the binding energy, the maximum isosteric heat at infinite dilution increases with temperature as does the difference between maximum and minimum heats – as one would expect.

Results for the binding energy are now presented without regard to the temperature dependence of the heats of adsorption as for the actual sensor system the picture is more complicated than just understanding the behaviour of the zeolite and the temperature dependence of the metal oxide is in fact likely to be dominating in this respect. The idea here is to try to associate trends in sensor behaviour with the basic, underlying zeolite adsorption behaviour for which binding energy gives a more primary picture.

Figure 2.3(a) gives the binding energies of linear alkanes of different chain length. As one would expect due to the increased number of guest-host interactions, the binding energy is seen to increase with chain length and for the most part with zeolite density (in accordance with the discussion of literature given in section 1.3), with some notable exceptions.

FER gives a higher than expected binding energy except with methane and most apparent with octane. This is likely to be a consequence of the 1D channel structure, the main channel of FER being very narrow and hence the adsorbed molecule feels strong interactions from the structure surrounding the channel. This correlates with the low calculated free volume of FER (figure 2.2). MOR also presents a 1D system, however, the channel is much wider and hence this effect is not so prominent.

The comparative binding energy of FAU is seen to be molecule dependent – propane binds more strongly with FAU than any other zeolite, the binding energy being greater than that of pentane in FAU. The methane-FAU and methane-LTA energies are also higher than expected. A feasible explanation is that this is due to smaller molecules being able to fit into the small windows at the cage intersections where they are able to bind more strongly – an optimum fit occurring for propane in FAU and only seen with methane in LTA due to the smaller window size. This is as observed on inspection of

the sorption structures as in figure 2.4. This point is examined further considering the results for alkanes at higher loadings given below.

The variation of binding energy for each zeolite is given in figure 2.3(b) as the standard deviation over the different alkanes tested, that is, the extent of variation from the mean of the data set, here the mean binding energy of the different alkanes within a particular zeolite. For the most part a trend is observed of increased variation with increased framework density apart from BEA and FER being a little higher than expected. Alternatively one can look at the extent of variation for each molecule within the different zeolites as in figures 2.3(c) and (d). 2.3(c) very clearly illustrates the point that confinement will affect adsorption to a greater extent the closer the dimensions of the molecule are to the confinement scale. The variation with different frameworks is seen to increase linearly with increasing carbon number. This result is perhaps somewhat trivial and it is helpful to consider instead the variation of binding energy where the results are normalised to the number of carbon atoms – as in figure 2.3(d). In this case there is still an overall trend of increasing variability with chain length but with a notable departure for propane – which is in accordance with the above discussion.

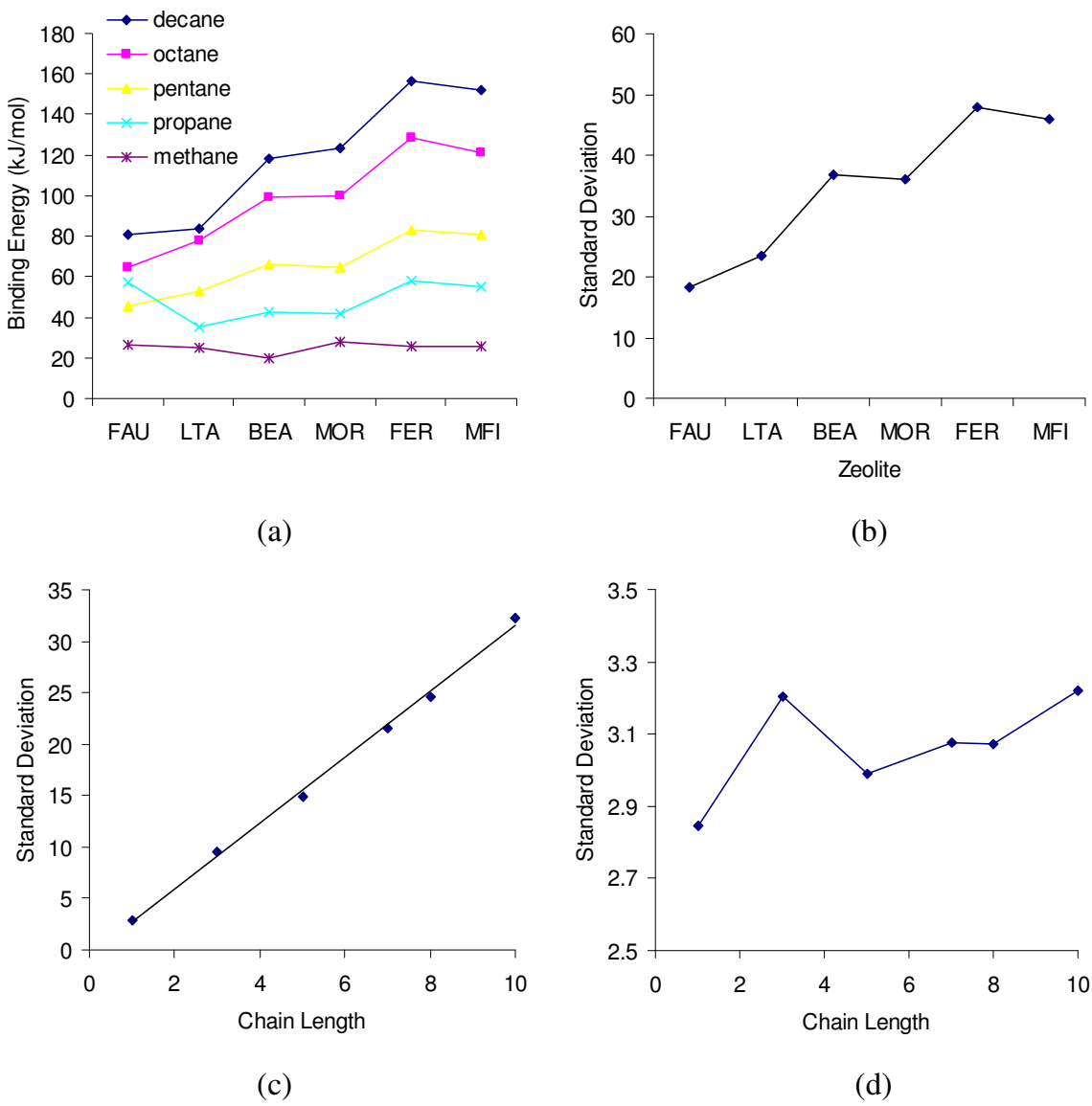

Figure 2.3: (a) Binding energy of linear alkanes in zeolite frameworks in order of increasing density. (b) Standard deviation of alkane binding energy in 6 zeolites as a function of chain length. (c) Standard deviation of binding energy of the set of linear alkanes for each of the different zeolite frameworks tested. (d) Standard deviation of alkane binding energy normalised by carbon number in 6 zeolites as a function of chain length.

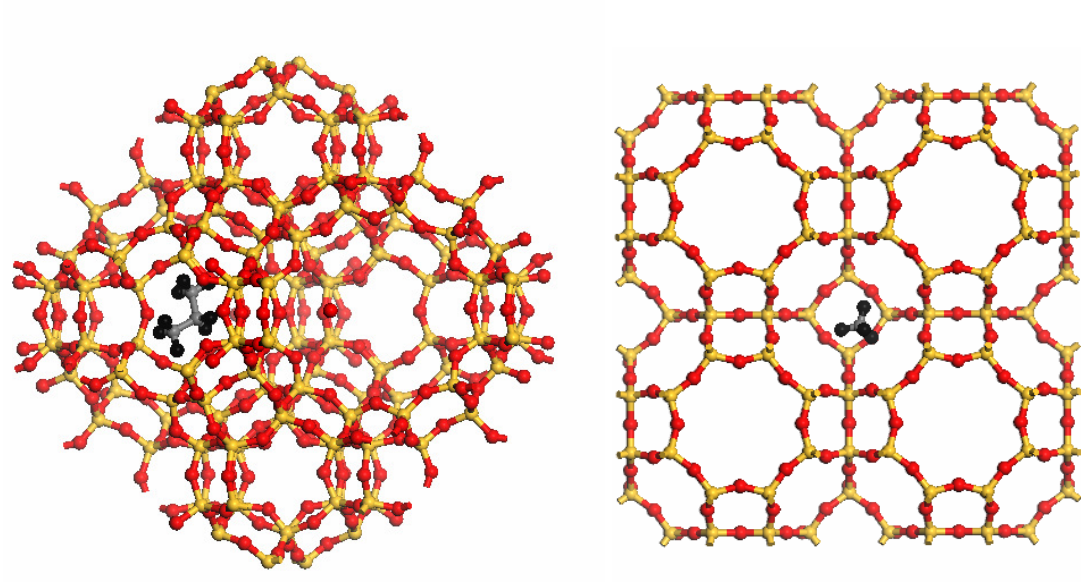

(a) (b)

Figure 2.4: (a) propane in FAU (b) methane in LTA. Atoms represented as silicon: yellow, oxygen: red.

Similarly calculations were performed for alcohols – again distinction would be presumed possible between alcohols of different chain lengths however not between alkanes and alcohols of the same equivalent chain length. This point is demonstrated in figure 2.5(a) giving the binding energy of equivalently sized propane and ethanol and also for the equivalently sized amine ethylamine and alkene propene (referred to as C2 molecules). Figure 2.5(b) gives binding energies for nitrogen dioxide, carbon monoxide, isopropanol (IPA) and propanol alongside ethanol (CO and NO_2 are included in light of parallel experimental studies).

The binding energy of ethylamine is slightly higher than the other three C2 sorbates other than for FER and LTA where all molecules give a very similar result. Also with MOR, propene gives a higher than expected binding strength. However, any differences are marginal at best (particularly when experimental difficulties are considered) and it is concluded that, based on these results, you could not expect to distinguish between these molecules.

NO_2 and CO, as with the C2 molecules, give very similar binding patterns, the only difference being the slightly higher average energy of NO_2, expected due to the larger size of this molecule. The three alcohols also follow this trend of size and here, as was

observed for linear alkanes, variable binding occurs within FAU. IPA and ethanol both bind strongly with FAU, being able to fit into the window structure, whereas for propanol the binding strength is lower, thus giving an example of possible discrimination between these two isomers, based on shape.

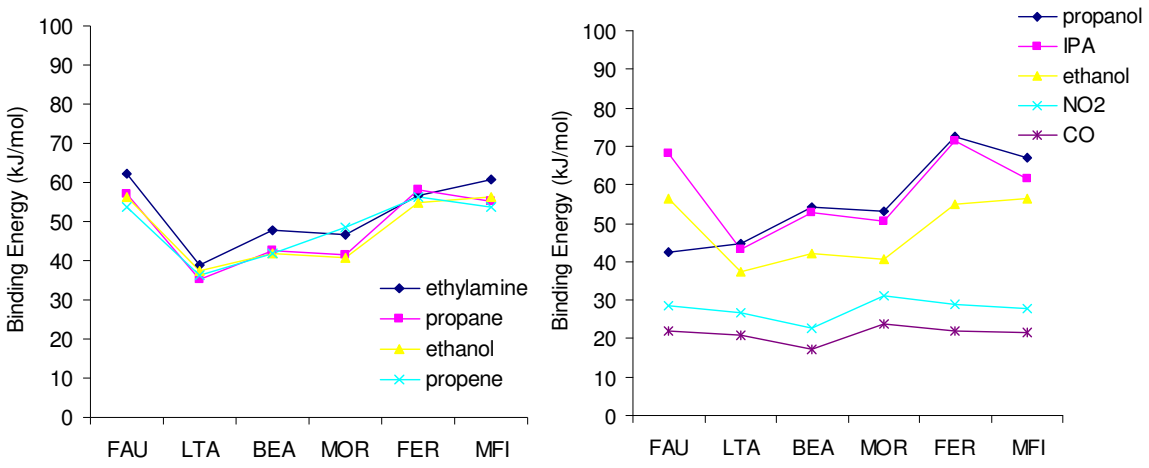

(a) (b)

Figure 2.5: Binding energy of (a) four C2 molecules with different functional groups and (b) NO_2, CO, propanol, IPA and ethanol in zeolite frameworks in order of increasing framework density.

Figure 2.6 compares branched, linear and aromatic C7 and C9 alkanes with the aim of further illustrating the role of shape on binding strength. A smaller subset of zeolites is used as the bulkier branched molecules are difficult to load within FER and MOR using Sorption. Manual insertion was deemed to be too unreliable for finding the sorbate position which was the true, global minimum in energy. Indeed, considering the critical dimensions given in table 2.2 it is unlikely that the branched molecules could fit into the very narrow channels of FER and, in some cases, of MOR.

The greatest variation in binding strength between the different molecules, in both cases, is observed with MFI for which the more linear the molecule the higher the interaction strength, the aromatics giving the lowest interaction strength. As shown from the critical dimension values, the branched molecules, as well as obviously being shorter, are generally more compact than their linear counterparts and hence on average the distance to the framework is larger such that the attractive interactions are diminished. A similar pattern is observed for BEA, however, 3-ethylpentane's binding energy is relatively higher than 3-butylpentane, this is most likely due to the longer 3-

butylpentane coinciding with a channel intersection, i.e. a region where it will experience less guest-framework interactions. The binding energies are very similar for the three molecules within LTA and FAU and this can be understood in terms of the cage structure, which will only "see" differences in the shape of the molecule in the way that has been described for the channel structure, if those molecules are of a size comparable to that of the cage dimensions or they closely resemble the pore wall. Again this is in agreement with what was discussed from the literature in section 1.3 for adsorption enthalpies of linear and branched in zeolites of different framework types.

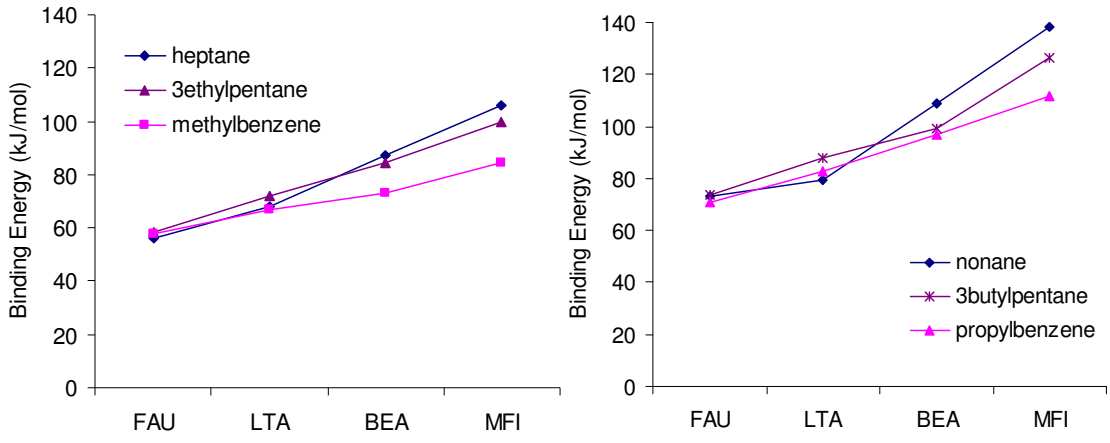

(a) (b)

Figure 2.6: Binding energy of (a) 7C hydrocarbons of different branching and (b) 9C hydrocarbons of different branching in zeolite frameworks in order of increasing density.

(2.4.3) Higher loadings

Binding energies were also calculated at higher loadings - figure 2.7(a) gives the average binding strength per molecule loaded for methane, propane and pentane at loadings of 1, 5 and 10 molecules puc. One notable difference between the infinite and finite dilution cases is the reduction of the propane-FAU interaction strength. Not all the molecules will now reside at the most favourable binding site described above and the result is a lower average energy per molecule, however, 5 and 10 molecules puc of propane give very similar patterns in binding energy. With methane, the variation in binding energy in the six zeolites decreases as the loading is increased. With pentane, on the other hand, there is very little difference between the three different loadings. As loading is increased the effects of specific shape and size correlations between framework and small molecules are effectively mitigated, though the decrease in

variation vs. loading is different for different sorbate-zeolite loadings and there may be intermediate loadings where the average binding energy increases rather than decreases with loading.

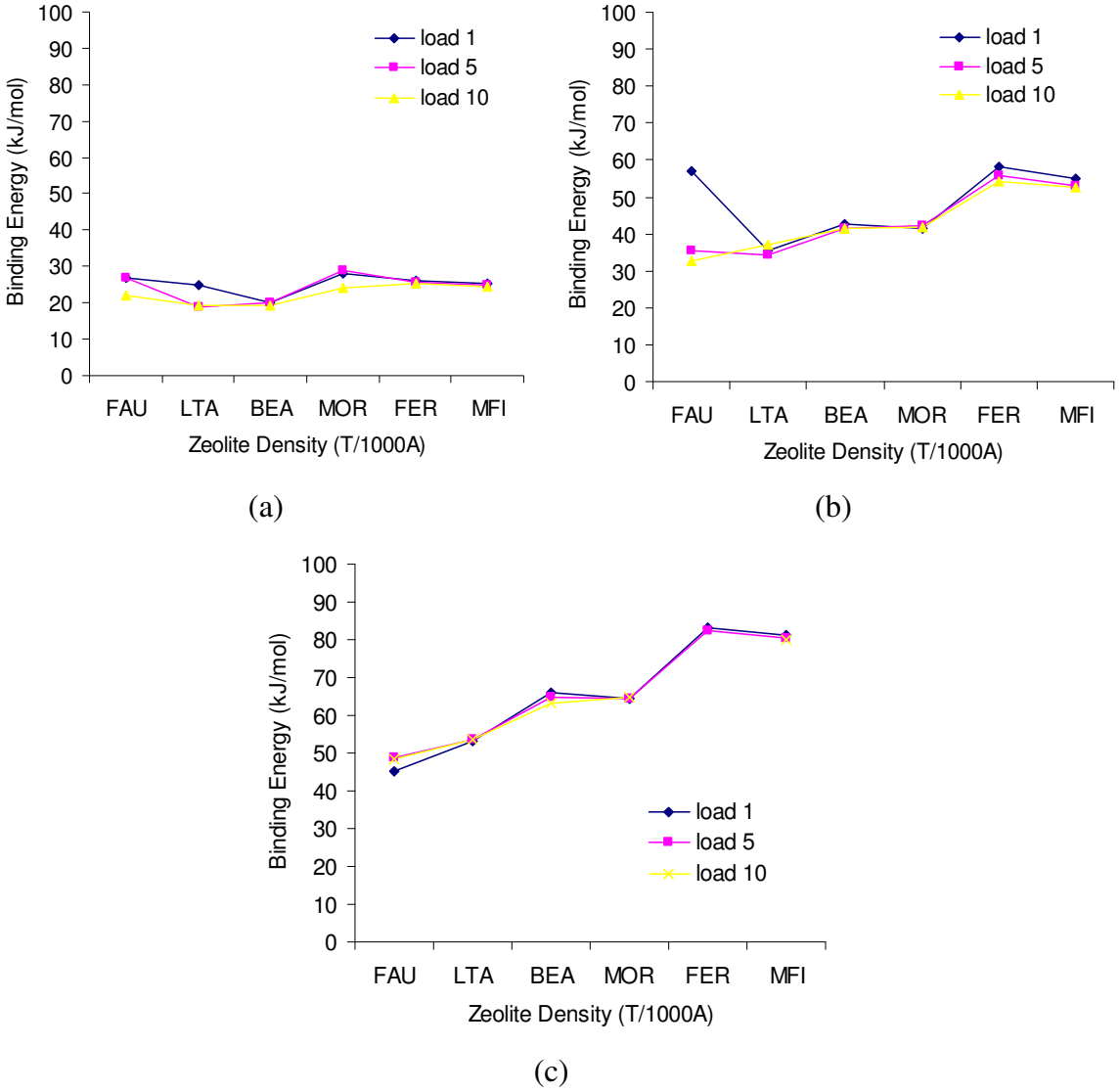

Figure 2.7: Plots for average binding energy per molecule for different loadings of (a) methane (b) propane and (c) pentane. Note it was not possible to load 10 pentane molecules into the FER framework.

Sorbate-sorbate interactions may also play a role – figure 2.8 gives the binding energy per molecule as a function of the load for groups of similarly shaped and sized sorbates in zeolites MFI and FAU. In MFI, the variation in binding strength with loading is small on an appreciable scale (given that *chemical accuracy* is typically considered to be 4 kJ mol^{-1} and that the experiment is more involved than simply what is occurring

within the zeolite) and the relative order of binding strength remains unchanged. In FAU the variation is more significant and as the load increases above around 10 molecule puc, the binding strengths become distinct following the order ethanol > ethylamine > propane. That there is more of a distinction between the interactions of these molecules at higher loads in FAU but not with MFI may be attributed to differences in framework – the large internal cage structure of FAU provides an environment where sorbate-sorbate interactions are more numerous than sorbate-zeolite interactions compared with the channel structure of MFI.

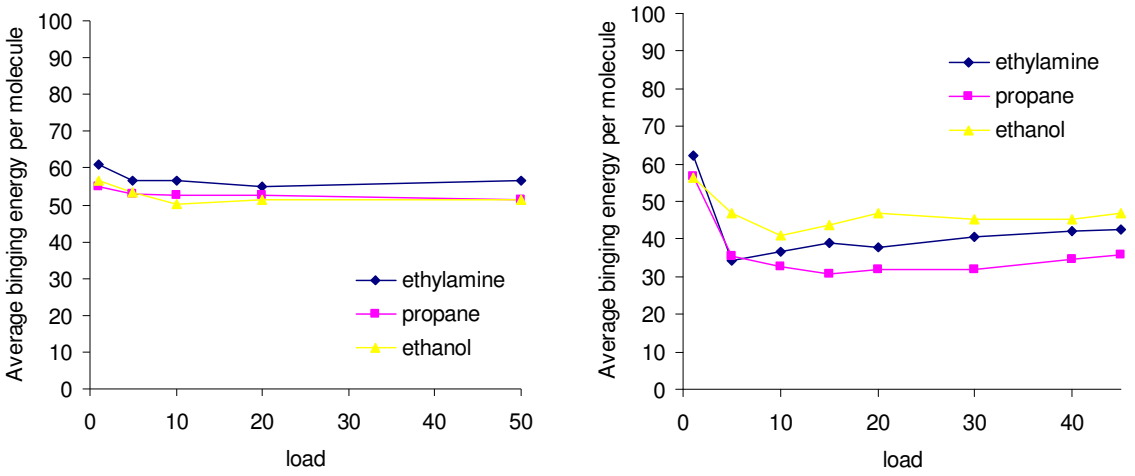

Figure 2.8: Average binding energy as a function of load for 2C molecules in (a) MFI and (b) FAU.

(2.4.4) Summary of force-field results

Several conclusions can be drawn from analysis of the force-field results. Firstly, variation in the strength of adsorption within the zeolite framework can be correlated to the size and shape of a molecule compared to the topology of the framework. The ratio of molecular to framework confinement dimension is seen to be of utmost importance. This is particularly clear from figure 2.3(c) which shows that the variation in binding energy for decane for the six zeolites tested was over 10 times that of methane – likewise greater variation was seen for denser zeolites with a given sorbate. Only if this ratio is sufficiently large will it be possible to observe variations which originate from shape correlations between framework and sorbate which have also shown to be of importance. For example, if the binding energies of linear alkanes in zeolites are normalised to the number of carbon atoms in the chain, thus eliminating the size effect, propane gives notably higher variation within the six zeolites tested chiefly due to its

tight fit into the cage window of FAU. Also differences in binding energy are observed to originate from whether a molecule is straight, branched or aromatic.

It is also concluded that no significant difference in binding strengths is observed between small molecules with different functional groups. In practice one might expect differences to occur based on the polarity of the molecule as the siliceous frameworks are hydrophobic in nature. With reference to table 2.1 which gives the calculated dipole moments of these molecules, one might expect a preference for the adsorption of alkanes/alkenes compared to alcohols/amines – this is not as observed from the force-field calculations. Whether or not this is due to shortcomings of the model or whether the variation really does not occur can not be stated explicitly, however, the extension of this issue to low silica, cation containing zeolites – for which the opposite is expected in terms of adsorption of polar molecules – certainly pushes beyond what is possible with the force-field formalism. This issue is discussed further in the next section.

The question is really, where variations are observed, will these be significant in practice against the backdrop of the highly involved process of the sensor response, and even when considering other factors of the zeolite adsorptive behaviour including concentration variation, ion interaction or the occurrence of a reaction?

Another point to address is how the adsorption strength actually translates into information about gas transport through a zeolite layer? On the one hand, strong adsorption can indicate a favourable transition from gas to zeolite and therefore through the zeolite layer, but on the other hand could indicate an unfavourable transition out of the zeolite and may result in blocking of channels (an issue at high loadings) hence further hindering gas transport. These points are discussed further in section 2.6 with comparison to experimental results.

(2.5) DFT Calculations

(2.5.1) Simulation details

In order to provide some quantification of the effects of the inclusion of cations within the system and to probe the dependency of adsorption on molecular polarity, cation-sorbate interactions having been investigated using the DFT code DMol^3 introduced

above. The aim was to further probe the adsorption of the small molecules between which little variation in the adsorption energy over the six siliceous zeolites considered was found following the force-field method (figure 2.5).

Due to the restriction on atom numbers imposed by the computational expense of DFT calculations, typical alumino-silicate zeolite fragments were used rather than the whole unit cell – these were standard four and six silicon-oxygen rings as depicted in figure 2.9. Such clusters have been shown to offer a suitable approximate representation in the study of different zeolite systems [18][19]. Another approach might be to use periodic DFT in order to provide detail of the long range interactions (electrostatic and dispersion) that are clearly ignored in using a cluster model. This is, however, a more complex and computationally demanding process for which the additional effort is not necessarily worthwhile for the present application (for which it is acknowledged that certain details of the system at hand are overlooked). The ease of application and the more generic nature of the simple cluster model are not disadvantageous attributes at this stage of the investigation [20].

Again structures were prepared using the Materials Studio platform; standard ring structures as shown were taken from crystallographic data and OH groups were added to saturate dangling bonds. The structures were geometry optimised using DMol^3 and the OH groups were then constrained such that only the ring atoms themselves were allowed to relax during subsequent optimisations. A sodium ion was then added to each ring structure and these again were optimised. To this structure the sorbate molecule – also energy optimised using DMol^3 – was then added in a chemically reasonable position just above ion and then optimised to obtain the adsorption energy of the sorbate onto the zeolite cluster. Several repeats were made, with different starting geometries.

The calculations were performed using the gradient corrected PW91 functional [21] and with the DNP (double numerical plus polarization functions) basis set [7] regarded as being suitable for the calculation of adsorption strengths of small molecules in zeolite clusters [22]

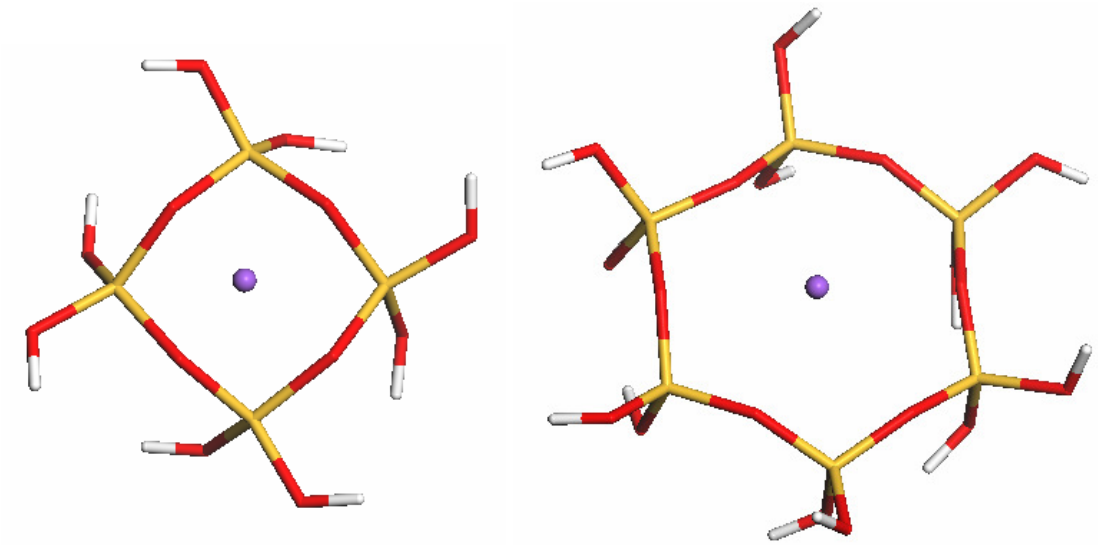

(a) (b)

Figure 2.9: (a) Four and (b) six ring zeolite clusters. Atoms represented as silicon: yellow, oxygen: red, hydrogen: white, sodium: purple.

(2.5.2) Results of DFT calculations

Figure 2.10 gives binding energies calculated using DMol[3] plotted alongside force-field calculated binding energies of the sorbates in siliceous zeolite LTA. Also plotted are values of dipole moment as given in table 2.2. There is more variation between the energies for different C2 molecules (figure 2.10(a)) calculated using the DFT method than following the force-field approach, although this is still to a relatively small extent for the 6-ring system. The pattern of variation is the same for both the zeolite clusters and whereas the force-field method yields a binding strength for ethylamine that is greater than that of ethanol, the DFT approach predicts it to be intermediate between propane and ethanol – correlating to the calculated dipole moments, i.e. a strong bind correlating to a high dipole moment.

All four data sets are in fact well correlated for the comparison of CO and NO_2 with ethanol in terms of the relative order (though it should be noted that in this instance the molecular size also follows this order). Here the 6-ring has the greatest variation in binding strength, the 4-ring system still having slightly more variation than the force-field results.

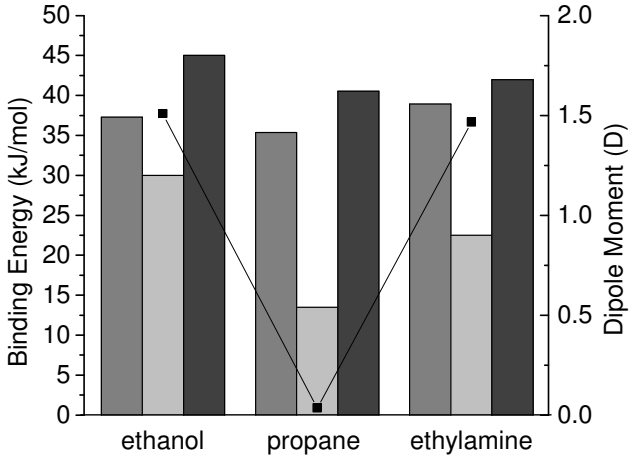

(a)

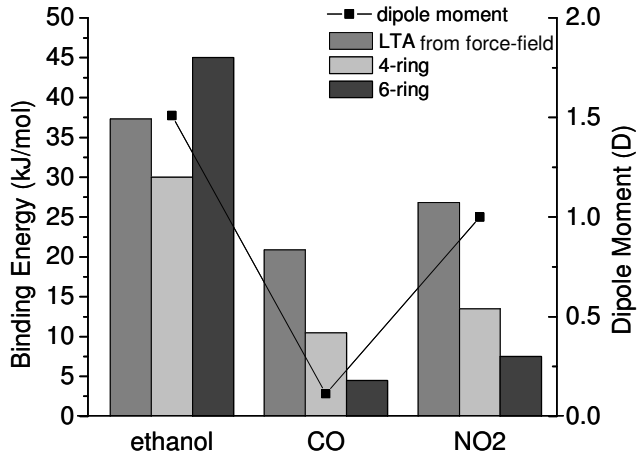

(b)

Figure 2.10: Binding energy calculated for 4 and 6 ring clusters with sodium ion, compared with force-field results for LTA and dipole moment for (a) 2C molecules and (b) CO, NO_2 and ethanol.

(2.5.3) Summary of DFT results

As was stated in section 2.5.1, the calculations performed here are quite simple in terms of what can be achieved with DFT methods, for example, larger, more complex clusters or periodic systems could be used or more informed efforts to position potential sorbates could be applied. However, for the discussion here, we are in part concerned with testing the expediency of different methods with a view to a process that can be easily and widely applied to encompass a vast number of different gas/zeolite pairings. Hence it is of interest to examine whether this simple approach can offer a constructive insight into the affect of ions in zeolites on the selective adsorption of different molecules.

The variation in binding energy of the three C2 molecules is greater when calculated using the DFT method compared with force-field approach, which at first glance could potentially be taken as evidence of selective adsorption at ion sites due to the presence of different functional groups. However, the two clusters themselves give different results to an extent similar to the increase in variability between the sorbates making, this conclusion questionable. None the less it can be argued that a more realistic picture of ion-molecule interaction is revealed as indicated by the correlation between the order of ethylamine and ethanol binding energies calculated using DFT and the dipole moment (i.e. expect a more polar molecule to bind more strongly with the ion): this order is incorrect from the force-field results. What leads from this of course, is that simply using the dipole moments, with the realisation that the zeolite structure will act to mitigate such distinction to a small degree, offers the same information as obtained form performing the DFT calculation and this would indeed be more in keeping with the objectives of the investigation as discussed. Hence the conclusion ultimately drawn here is that these calculations are not well suited to the design of a sensor array.

(2.6) Comparison with experimental data.

(2.6.1) Linear hydrocarbons [23]

Figure 2.11(a) gives the response of control and zeolite-modified chromium titanate (CTO) sensors to linear alkanes of different chain length. The CTO powder was formed as described in [23] and screen printed to form the sensor structure, over this the zeolites were overlaid, again using the method screen printing. The zeolites used were alumino-silicate forms of FAU (zeolite Y) with ratio of silicon to aluminium Si/Al = 3, BEA (zeolite beta) with Si/Al = 12 and MFI (ZSM-5) with Si/Al = 30. The responses of the zeolite sensors to the shorter chain-length alkanes are significantly enhanced compared to the control sensor, the response decreasing to that of the control sensor as the chain length increases to about 10. The response of the control sensor, in comparison, does not depend greatly on chain length. The zeolites are effective in enhancing the response following the order zeolite-Y > zeolite-β > ZSM-5.

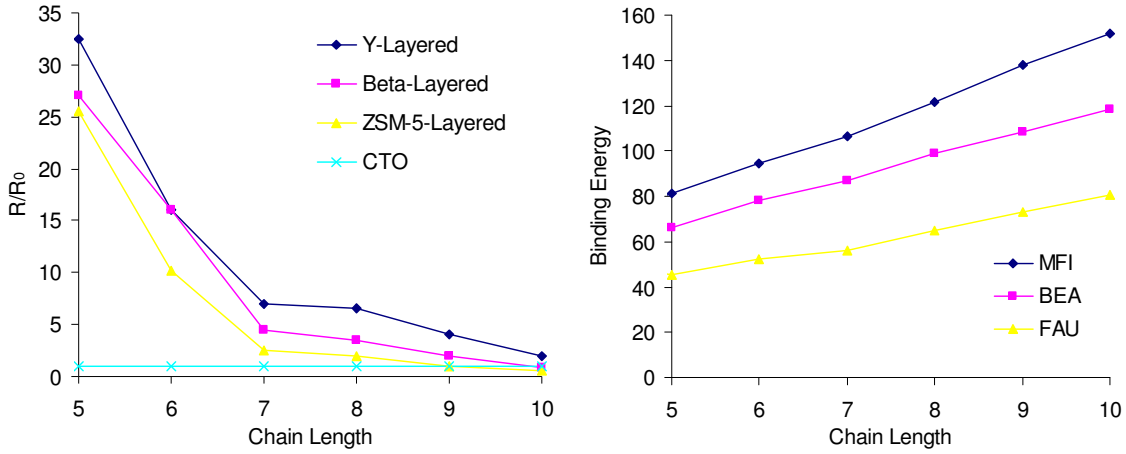

(a) (b)

Figure 2.11: (a) Control CTO and zeolite modified sensor response (R/R_0) at 400˚C and (b) binding energies calculated using force-field method for linear alkanes of increasing carbon chain length.

The enhanced response suggests that the gas stream is actually chemically modified within the zeolite layer, but even though the occurrence of a reaction is not something that has been considered here, some correlation with the force-field calculated binding energies can be identified. The calculated binding energy, figure 2.11(b), increases with increasing chain length. An interpretation based solely on this result is that an increase of binding strength is indicative of inhibited diffusion through the zeolite pore network with larger molecules adsorbing strongly rather than passing through to the sensor layer (and also possibly consequently blocking channels) – hence there is a decrease in sensor response. Whilst a reaction does complicate this picture, as one must now consider reactants and products, the above is likely to stand as an underlying argument as larger reactants will give larger products which will face the same issues diffusing through the layer.

The binding strength in the three different zeolite frameworks follows the order of MFI > BEA > FAU, which, following the reasoning given above, does correlate with the sensor response. However, the extent to which the binding strengths differ increases with chain length, contrary to what is observed for the sensor response. This shows the limit of the comparison between the two data sets as at this point the aspect of sorbate behaviour within the zeolite which is represented in figure 2.11(b), becomes irrelevant in terms of experimental conditions of the zeolite-sensor system.

Note, it is also observed experimentally that the response time increases with chain-length [24], again indicating slower diffusion of the longer molecules. Response time and diffusion-reaction effects are discussed in more detail in chapter 4.

(2.6.2) CO, NO_2 and ethanol [25]

Figure 2.12 presents a comparison between force-field calculated binding strengths and experimental results of the fractional increase in conductance $((G-G_0)/G_0)$ of WO_3 sensors with zeolite over layers as described in [25]. WO_3 was obtained from New Metals Chemicals Limited. The zeolites used were as in section 2.6.1 with the addition of zeolite A (LTA) with Si/Al = 1. The WO_3 and zeolite powders were screen printed to form the layered composite sensor device. Binding energies are given per molecule for infinite dilution and load 20 puc.

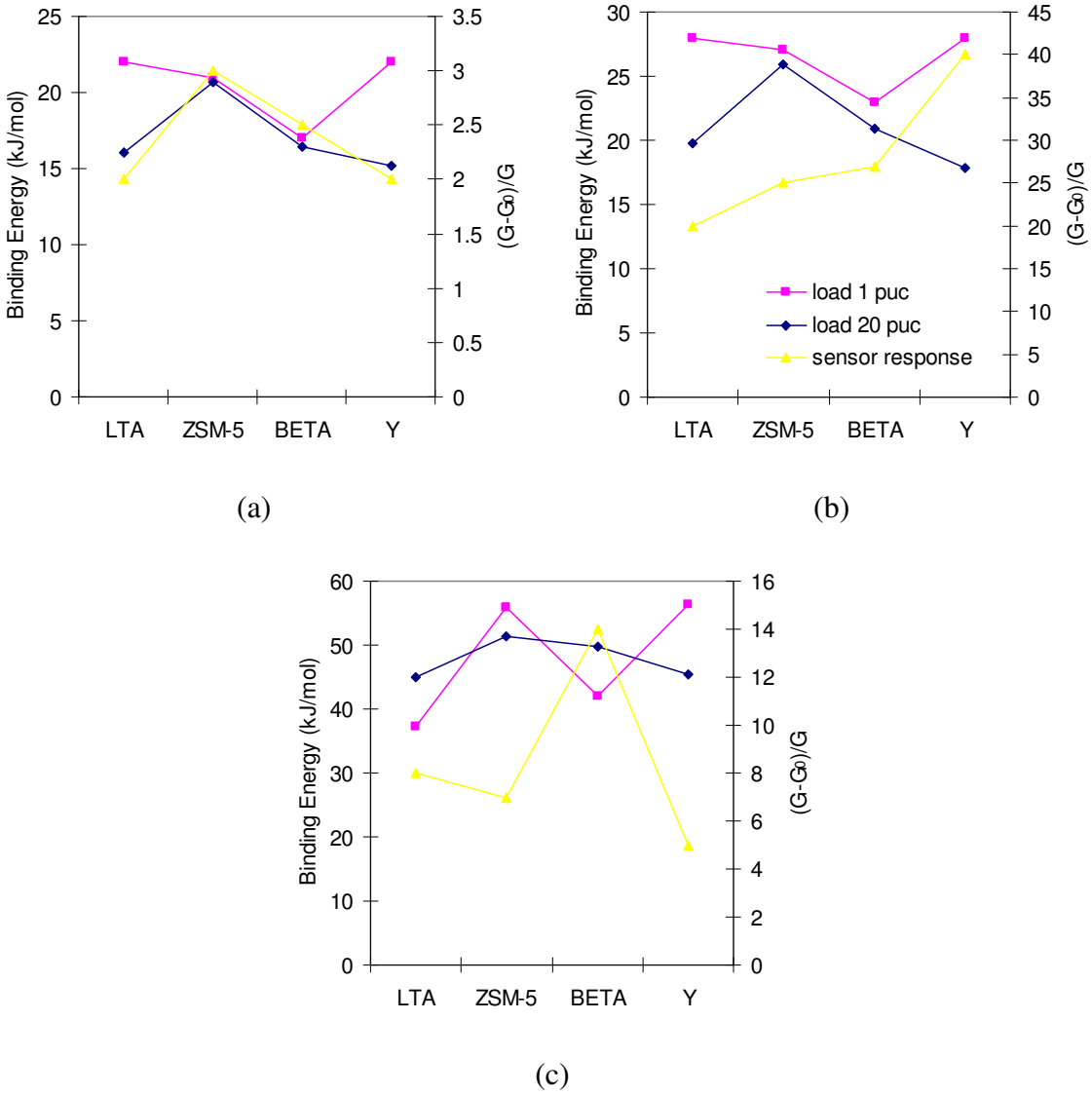

Figure 2.12: Zeolite modified WO_3 sensor response at 350˚C to and calculated binding energies at two different loads of (a) CO, (b) NO_2 and (c) ethanol with four zeolites (named according to experimentally used form).

The binding energy of CO at a load of 20 puc (for which the effect of enhanced binding of the small molecule within the window of a cage structure is not observed) appears to be well correlated to the sensor response. Here however, contrasting to what was argued previously for paraffin molecules; a strong bind correlates to a high response. This can be reasoned in terms of a favourable transition of CO from the gas phase into the zeolite therefore enhancing the transport of gas to the sensor. That the alkanes behave differently can be attributed to their comparatively larger size, resulting in the molecules being more likely to block the zeolite channels.

Whilst NO_2 and CO have very similar binding strengths in the four zeolites, their response patterns are different – this is particularly true with zeolite-Y. This is very likely due to the neglect of the presence of ions in the force-field model, the experimentally used form of zeolite-Y being known to be ion containing. As was shown in figure 2.10, ion-sorbate interaction strength is expected to increase following CO < NO_2 < ethanol and it is true that the deviation of experimental response from the force-field result for adsorption strength in FAU follows this order.

For ethanol, it could be argued that there is correlation of response with the binding energy of the type described in section 2.6.1, where a stronger binding energy indicates slower diffusion, again explained in terms of the larger size of ethanol such that the effect of channel blocking is more likely to dominate over increased transition from the gas phase.

It is also noted that the directions of deviation of NO_2 and ethanol response in FAU are contrasting – this is demonstrative of the importance of the interpretation of what has occurred in the zeolite in terms of the sensor. NO_2 is an oxidising gas and is expected to give a conductance decrease with n-type WO_3 whereas ethanol is a reducing gas which should give a conductance decrease – it is suggested that a reaction occurs in the zeolite converting the gases from their reducing/oxidising types, hence the observed deviation in results.

(2.6.3) Isopropanol and ethanol [26]

CTO sensors were prepared, as in section 2.6.1, as described in [23]; the zeolites used were aluminosilicate forms (with Si/Al ratios as above) of LTA (zeolite A), MFI (ZSM-5) and FAU (zeolite Y). The sensors were screen printed and tested with isopropanol (IPA) and ethanol.

Here for both gases, correlation is noted between results for binding energy and response where a strong bind is taken to indicate an unfavourable transition through the zeolite phase to the sensor layer. Firstly it is observed that the response is reduced from the control sensor, except for the LTA sensor response to ethanol, indicating a reaction to a less sensitive species occurs within the zeolite or that the gas is not passing through the sensor zeolite effectively. Also for the most part the response of IPA is higher than that of ethanol, as predicted by the binding energy calculations. The response of the

LTA sensor to ethanol, however, is enhanced indicating that there is a reaction occurring within the zeolite to a product of higher sensitivity, for the IPA on the other hand, the response is reduced. That IPA does not follow the same type of reaction is unexpected – in fact it is more likely the case that the larger size of IPA compared to ethanol means that it cannot pass through the small window of the LTA framework. The values of critical dimension given in table 3.2 support this argument.

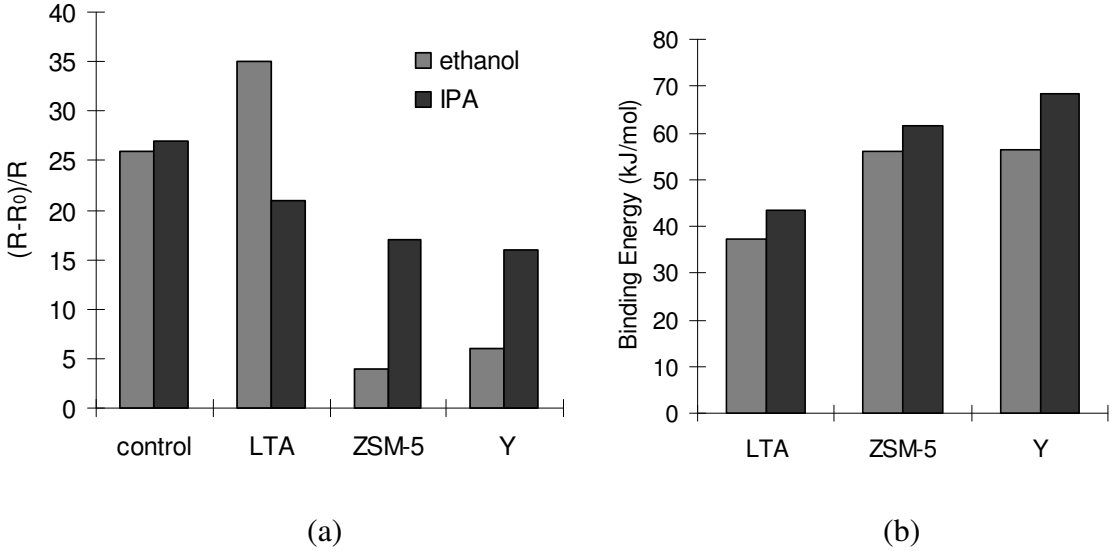

Figure 2.13: (a) Control CTO and zeolite modified sensor response ($(R-R_0)/R$) at 400˚C and (b) binding energies calculated using force-field method for ethanol and IPA.

(2.7) Conclusion

It is concluded that from the results presented above, evidence can be drawn to support the use of zeolites for the purpose of gas sensing. It is shown that the binding strength of a molecule in a zeolite framework depends on the shape and size of the molecule that is adsorbed within a specific zeolite framework. It has also been shown that the presence of ions is likely to affect adsorption based on molecular polarity – though also it is suggested that the larger zeolite structure in fact acts to mitigate this effect.

Whilst the sensor response data can to some extent be rationalised in terms of the calculations presented here, ultimately it has to be concluded that the quantification of the strength of adsorption of gas within the microscopic framework of a zeolite, in either of the ways investigated here, is not sufficient to predict the effect of a zeolite over-layer on sensor response. For one, it is clear that there is a wealth of details for each gas-zeolite combination in terms of reactions and specificities of temperature and

concentration dependencies making generalisations of the types explored here limited in their usefulness. A much more thorough set of exploratory calculations are required – that fully probe the different aspects of a particular gas-zeolite instance. This however, requires the expenditure of a considerable amount of effort in input and process and will greatly reduce the model's transferability to different gas-zeolite combinations, something that would be highly desirable here.

Whilst the observed behaviour of the zeolite-gas system is of course due to the atomic or electronic interactions, the methods investigated here fall short of being able to reliably predict the macroscopic manifestation of the sorbate-zeolite interactions – that is the transport of the test gas molecules through the zeolite layer. Whilst the individual drawbacks of the force-field and DFT methods for studying adsorption in such systems have been discussed, ultimately the correlation between adsorption and diffusion in such complex topologies emulates this complexity, the matter being further complicated by the two fold-system of pores characterised by different length scales and the occurrence of reactions and essentially it is necessary to turn to other methods that look more directly at diffusion.

It is also important to remember at this point that the properties of the zeolite, for the application central to this work, must be defined with respect to the sensor. The sensitivities of the sensor material to different gases define the transformation properties of the zeolite in terms of whether the zeolite acts to enhance or diminish the response. Also the transport properties of the zeolite may be directly influenced by the diffusion-reaction properties of the sensor layer as, as with the micro- and macroscopic phases of the zeolite, the transport within a medium depends on the surrounding environment – we can define a second composite system consisting of zeolite and sensor phases. The discussion of diffusivity (and reactivity) in zeolites is hence extended to the more general topic of diffusion in porous or composite media.

References

[1] B. Smit, T.L.M Maesen, Chem. Rev., 108 (2008) 4125. "Molecular Simulations of Zeolites: Adsorption, Diffusion, and Shape Selectivity."

[2] N.J. Henson, A.K, Cheetham, J. Inclusion Phenom. Mol. Recognit. Chem., 21 (1995) 137-158. "Absorbed Molecules in Microporous Hosts - Computational Aspects."

[3] A.R. Leach, "Molecular modelling: principles and applications" Pearson Education (2001).

[4] D. Frenkel, B. Smith, "Understanding molecular simulation: from algorithms to applications." Elsevier, USA (1996).

[5] P. Hohenberg, W. Kohn, Phys. Rev. B, 136, (1964) 864-871. "Inhomogeneous electron gas."

[6] W. Kohn, L.J. Sham, Phys. Rev. A, 140 (1965) 113-1138. "Self-consistent equations including exchange and correlation effects."

[7] B. Delley, J. Chem. Phys., 92 (1990) 508-517. "An all-electron numerical method for solving the local density functional for polyatomic molecules."

[8] B. Delley, J. Chem. Phys., 113 (2000) 7756-7764. "From molecules to solids with the DMol^3 approach."

[9] Y. Inada, H. Orita, J. Comput. Chem., 2008, 29, 2, 225-232. "Efficiency of Numerical Basis Sets for Predicting the Binding Energies of Hydrogen Bonded Complexes: Evidence of Small Basis Set Superposition Error Compared to Gaussian Basis Sets."

[10] J.B. Nicholas, Top. Catal., 4 (1997) 157-171 "Density functional theory studies of zeolite structure, acidity and reactivity."

[11] Materials Studio, Version 4.0, Accelrys Inc.: San Diego 2005.

[12] H. Sun, J. Phys. Chem. B, 102 (1998) 7338-7364. "An ab initio force-field optimized for condensed-phase applications – overview with details on alkanes and benzene compounds."

[13]M.F. Allen, D.J. Tildesley, "Computer Simulation of Liquids" Oxford Science Publications (1987).

[14] E. Beerdsen, D. Dubbeldam, B. Smit, Phys. Rev. Lett., 96 (2006) 44501- 44504. "Understanding diffusion in nanoporous materials"

[15] F. Jimenez-Cruz, G.C. Laredo, Fuel, 83 (2004) 2183-2188. "Molecular size evaluation of linear and branched paraffins from the gasoline pool by DFT quantum chemical calculations."

[16] C.E. Webster, R.S. Drago, M.C. Zerner, J. Am. Chem. Soc., 120 (1998) 5509-5516. "Molecular Dimensions for Adsorptives."

[17] A. Bondi, J. Phys. Chem., 68 (1965) 441-451. "van der Waals volumes and radii."

[18] M. Danilczuk, A. Lund, Chem. Phys. Lett., 490 (2010) 205-209. "Adsorption of NO in Li-exchanged zeolite A. A density functional theory study."

[19] L.A.M.M. Barbosa, G.M. Zhidomirov, R.A. van Santen, Phys. Chem. Chem. Phys., 2 (2000) 3909-3918. "Theoretical study of methane adsorption on Zn(II) zeolites."

[20] J.D. Gale, Top. Catal., 3 (1996) 169-194. "A density functional study of molecular adsorption in zeolites."

[21] J.P. Perdew, Y. Wang, Phys. Rev. B, 45 (1992) 13244. "Accurate and simple analytic representation of the electron-gas correlation energy."

[22] D.F. Plant, A.Simperler, R.G. Bell, J. Phys. Chem. B, 110 (2006) 6170–6178 "Adsorption of methanol on zeolites X and Y. An atomistic and quantum chemical study."

[23] T.C. Paraskeva, "Improving the performance of sensor for electronic noses using zeolites as selectivity modifiers", Ph.D. thesis, University College London, 2004.

[24] D.P. Mann, K.F.E. Pratt, T. Paraskeva, I.P. Parkin, D.E. Williams, J. IEEE Sens., 7 (2007) 551-556. "Transition Metal Exchanged Zeolite Layers for Selectivity Enhancement of Metal-Oxide Semiconductor Gas Sensors."

[25] A. Afonja, S. Dungey, R. Binions, I. P. Parkin, D.W. Lewis, D. E. Williams, ECS Transactions, 16 (2009) 77-84. "Gas Sensing Properties of Composite Tungsten Trioxide-Zeolite Thick Films."

[26] R. Binions, A. Afonja, S. Dungey, D.W. Lewis, I. P. Parkin, D. E. Williams, ECS Transactions, 19 (2009) 241-250. "Zeolite Modification: Towards Discriminating Metal Oxide Gas Sensors"

Chapter 3: Diffusion and reaction in porous media.

(3.1) Introduction

Diffusion in porous or composite media has been widely researched, the transport of gas or fluid species being central to many important processes such that developing a model to understand diffusive behaviour is crucial across different scientific fields. Because of the typically complex and varied geometries of the systems of interest and the large number of variables which could potentially have a significant bearing on the behaviour, the ideal of an all-encompassing, transferable model is unrealistic. It is instead the case that a model will need to focus on specific features of the system at hand, for example the scale of confinement or a heterogeneous distribution of adsorption sites, and hence there exist a vast number of different approaches in accordance with the numerous applications.

The importance of diffusion processes in understanding sensor behaviour has been discussed and operating within our system one can identify different diffusional regimes; the porous layers of metal oxide, those of the zeolite crystallites and the zeolite micro-pore system where the pores and channels are of molecular dimension. The topic of zeolitic diffusion is an extensively, if not conclusively, researched field in itself, the nano- or meso-scale confinement giving rise to unique diffusional properties. In this chapter, firstly a brief review is given into different methods used to tackle zeolitic diffusion alongside an introduction to some key features of diffusion theory.

The essential difference between the porous layers of the sensor system and the microporous zeolite structure is identified as the larger scale of confinement of the former, as was discussed in chapter 1. The atomistic detail is less significant in the scheme of the larger system and it is more appropriate to characterise the confining solid in terms of the porosity or the distribution of different phases and the penetrability of and diffusivity within the different phases.

In chapter 1 the idea of an effective diffusivity was introduced, represented as a function of bulk properties of the solid – its porosity, tortuosity and bulk phase diffusivity [1]. Effective medium models are widely used in study of diffusion in composite media, collectively referred to as effective medium theory (EMT). The cornerstone theory of EMT was originally developed by Landauer [2] to describe the

electrical resistance of binary metallic mixtures and was then extended to the analogous system of diffusion in porous materials by Davis [3]. EMT assumes an inhomogeneous distribution of locally homogeneous regions of the different phases. Local inhomgeneities are then treated as fluctuations in the diffusivity of an effective medium with diffusivity equal to that of the system as a whole. Based on these considerations, an expression for the effective diffusivity can be derived. Whilst this theory has proved successful [4,5], a lack of long range correlations renders the standard EMT formalism inadequate near the percolation threshold (i.e. the point at which infinite connectivity of a system first occurs) [6].

Other approaches for the study of porous media include the method of random walks [7,8], Monte Carlo simulation [6,9,10], homogenization [11] and perturbation techniques [12] and finding eigensolutions of the diffusion equation [13]. It is generally regarded that tracing random walkers and finding diffusion eigenstates are the most widely and effectively applicable. The eigenstates approach is less restricted by timescale than the random walker method and is a more appropriate choice if long time spans are to be considered, i.e. on the scale of a typical sensor response time [13,14]. The model presented here is based of the method of eigenstates, following the formulism of Bergmann and Dunn [13,15,16,17], originally applied to a system of impenetrable obstacles at the surface of which particle decay may occur. This has been adopted as a representation for the porous metal oxide sensor system. The theory has been extended, as is described in the course of this chapter, to model a system of two penetrable phases. In this case, a reaction may occur within one or both of the phases as defined by a bulk rate constant and this is used to represent the porous, two-phase zeolite layer. Details of the computational method are given and results are presented to illustrate the dependency of the effective diffusivity and rate constant of the two model systems on the porosity, surface area, partition coefficient, ratio of bulk phase diffusivities and surface and bulk reaction properties.

(3.2) Diffusion in zeolites

(3.2.1) Introduction to diffusion theory

The diffusivity may either quantify the movement of molecules in response to a concentration gradient, in which case it is referred to as the transport diffusivity, or in the absence one, where it is known as the self diffusivity.

The transport diffusivity, D_t, or Fickian diffusivity, is generally thought of being the subject of Fick's 1st law relating the flux, J, and concentration, C:

$$J = -D_t \nabla C \qquad \text{Equation 3.1}$$

The self-diffusivity, D_s, can also be described using an expression such as 3.1, however, in this case the total concentration of the system is constant and C refers to the concentration of a small subset of molecules known as tracer molecules.

D_s can also be found from the Einstein equation which describes the time dependence of the mean square displacement, $< \bar{r}(t) >$, of the tracer molecules:

$$< \bar{r}(t) >= 6D_s t \qquad \text{Equation 3.2}$$

(Alternatively $< \bar{r}(t) >$ could be computed from the velocity autocorrelation function).

Ultimately it is the transport diffusivity that we are concerned with for the application of gas sensing; however, the self-diffusivity is often the more natural subject of zeolite studies. D_t and D_s, as defined by equations 3.1 and 3.2, are not equal but can be related via a third diffusivity, the Maxwell-Stephan or corrected diffusivity D_0, so called as it formulates the diffusivity as a consequence of a gradient in chemical potential which, whilst it may be more natural to consider concentration, is the true driving force for transport type diffusion [18].

(3.2.2) Methods for studying diffusion in zeolites

Molecular dynamics [19,20] is the extension of the force-field formulation introduced in the last chapter, to model the time evolution of a dynamical system. As well as initial positions, initial atomic velocities are assigned randomly at the beginning of the calculation in accordance with the defined system temperature. By integrating Newton's second law with respect to time, the positions of the system components can be traced over time following which the mean square displacement can be calculated. The self-diffusion coefficient can then be calculated following equation 3.2.

Compared to its energy minimisation counterparts (chapter 2), molecular dynamics is a highly computationally expensive method due to the computation of the potential field over successive time steps. As a consequence the method is restricted to relatively fast

diffusing sorbates such that a sufficient sample of the molecule's diffusional behaviour can be recorded in the short amount of physical time that it is possible to simulate. This time is reduced considerably if framework motion is to be included and similarly, high concentrations will challenge the limit of available computing power (bearing in mind, of course, that available computing power is rapidly growing).

Molecular dynamics can be applied to find transport diffusivities, as reviewed in for example [20,21], all approaches having in common a significant increases in the CPU-time required for the calculation. The increase in computational difficulty is reflected in comparison of results with other methods which show less consistency for the transport coefficients than for self-coefficients. However, in light of increasing computing power there has been a shift to the computation of transport diffusivities via molecular dynamics and such calculations are beginning to prove their worth [22].

Longer times can be modelled with the departure from the atomistic to the mesoscopic scale. Stochastic or "jump" models describe the zeolite as a network of interconnected pores with adsorption sites at the intersections. Adsorption sites are sites of low potential energy and molecules are presented with an energy barrier when moving to an adjacent site. This model more closely follows the concept of configurational diffusion discussed in chapter 1. The event of the molecule hopping between regions of the zeolite is referred to as a rare event (n.b. the difficulty in using time-restricted molecular dynamics).

By modelling the diffusive behaviour as a Markov stochastic jump process [23], the relevant equations can be solved to find the diffusivity within the network using a form of the Monte Carlo algorithm known as kinetic Monte Carlo [24]. Unlike with molecular dynamics, the time scale does not represent actual physical time. However, this model is closely associated with the method of random walks [7] and through following a random walk type formulism, a timescale can be incorporated into the model via the introduction of a hopping rate between sites. The topology and intermolecular interactions of the system are included in the calculation via the positioning of adsorption sites and direction of jumps allowed. All rates of hopping between sites are assumed to be known beforehand and that nothing can be determined from the simulation about the rates is a disadvantage of this type of model.

To compute the hopping rate one needs to know the probability of the molecule being at the top of the energetic barrier which in turn requires knowledge of the free energy

surface. Molecular mechanics, as discussed in chapter 2, offers one route for finding free energy surfaces. Additionally some concept – an average – of the time that it takes for the molecule to cross the barrier clearly needs to be incorporated and for this dynamically corrected transition state theory (TST) is typically used [24]. Kinetic Monte Carlo can then be used to convert the hopping rate to a diffusivity.
Approaches based on these methods have been particularly insightful in understanding the loading dependence of the different diffusivities [25] [26].

On a somewhat different note, Derouane et al. presented the creep diffusion model [27,28], based on a more fundamental picture of confinement. It focuses on the curvature of the zeolite internal surface and the attractive and repulsive non-covalent interactions that occur between sorbate and the zeolite. The molecule seeks to be in an optimum position in terms of the balance of these forces, where the energy is a minimum. This results in the molecules adsorbing more closely to the curved surface than would be expected for a flat surface (such that the molecule is seen to "creep" along the zeolite surface). In fact his model offers a theoretical explanation to much of the unusual behaviour of diffusion in zeolites which include rapid diffusion of molecules which fit tightly within a pore or channel (single-file diffusion) [29], the window effect (or resonant diffusion) [30] and shape dependent catalytic behaviour [31].

Finally effective medium theory (EMT) has also been applied to zeolitic diffusion, for example as in [32] where its application was shown to be successful in the modelling of a heterogeneous distribution of adsorption sites (where the system is far from the percolation threshold).

Experimentally it is generally found – as one would expect - that macroscopic methods such as membrane permeation [33], uptake methods [34] and chromatographic methods [35] more readily lend themselves to the measurement of the transport diffusivity whereas microscopic methods including NMR techniques [36], Incoherent QENS (quasi-elastic-neutron-scattering) [37] and tracer methods [38] may be used to find the self-diffusivity.

Despite the considerable volume of research carried out into the subject of diffusion in zeolites, results are rather inconclusive both between different computational approaches and in comparison with experimental methods (and indeed between different experimental methods). Diffusion coefficients obtained following different approaches varies sometimes by several orders of magnitude [20]. This is less due to a particular technique being incorrect and more so the high sensitivity of such systems to the operating conditions.

Despite this, some general trends have successfully been brought to light, although they are typically subject to exception, for example, the decrease in diffusivity of linear alkanes with increasing chain length (c.f. section 2.6.1) [20]. Indeed, insight certainly can be gained by researching the literature on the calculation and measurement of diffusion coefficients in zeolites using the methods discussed, however, care should be taken in regards to the operating conditions used and values should be taken as a guide rather than as a definitive quantification.

(3.3) Overview: A model for diffusion and reaction in composite media

(3.3.1) Key aspects of the Bergman-Dunn model

We now consider the larger scale confinement of gas, which occurs both within the zeolite and sensor layers of the sensor system, and how certain properties of the confining solid shape the transport of gas through the device.

The sensor is thought of as consisting of impenetrable particles of metal oxide, represented in figure 3.1(a) as being spherical, surrounded by a pore phase i.e. air. Whilst the particle is assumed impenetrable, hence presenting a boundary to the flow of gas, a reaction may occur at this boundary. Note, this model is in keeping with the original Bergman-Dunn system introduced above.

The zeolite crystallites (figure 3.1(b)) are, on the other hand, accessible to the gas (assuming the molecule in question has dimensions smaller than the zeolite pore structure). Here a reaction may occur within the zeolite phase. There is no rigid boundary as with the sensor system but there may be a change in properties such as the diffusivity as the gas moves between the two phases.

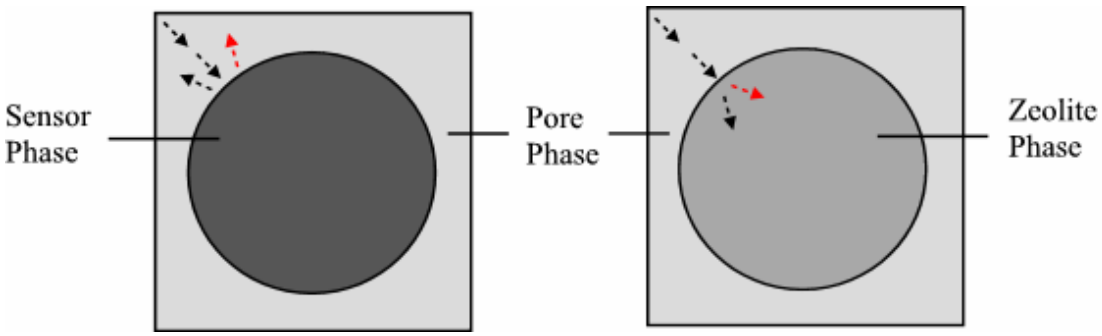

(a) (b)

Figure 3.1: 2-D representation of the systems to be modelled. Depicted is a spherical object of the phase of interest (either metal oxide sensor or zeolite), surrounded by the pore fluid (which will typically be air). A reaction may occur either (a) at the sensor surface or (b) within the zeolite phase.

To begin, equation 1.2 is recalled for the time and space dependent variation of concentration, given here as equation 3.3, where D is the diffusivity, k is the rate constant, $\vec{r}$ is the position vector (in Cartesian space) and t denotes time:

$$\frac{\partial C(\vec{r},t)}{\partial t} = \nabla \cdot (D(\vec{r},t)\nabla C(\vec{r},t)) - k(\vec{r})C(\vec{r},t) \qquad \text{Equation 3.3}$$

A more mathematically precise term for the concentration is introduced as the *diffusion propagator*, $G(\vec{r},\vec{r}',t)$, which also satisfies the diffusion-reaction equation 3.3 and which not only expresses the concentration as a function of the current position (and time) but also takes into account its point of release (at t=0). Using the language of random walks, $G(\vec{r},\vec{r}',t)$ is said to be a Green's function and the conditional probability of finding a random walker (or particle of gas) at position $\vec{r}$ and time t after release at $\vec{r}'$, $t = 0$ .. Both the diffusion propagator and the concentration are referred to interchangeably here (both follow equation 3.3).

That modelling diffusion in porous media is so challenging arises from the difficulty of implementing boundary conditions. For a system of impenetrable obstacles the general form for the boundary condition is $\frac{\partial C}{\partial \vec{r}} = 0$ at the pore-solid boundary.

It is because the boundary presents a discontinuity in the concentration that the problem becomes quickly unworkable for anything but the simplest geometries. Where both

phases are penetrable, whilst there is not a discontinuity, there is still a difficulty in modelling the partitioning of gas in a complex system.

The need for additional terms to incorporate the occurrence of a chemical reaction complicates matters further especially when the reaction cannot be characterised as in equation 3.3 but is localised at an interface (adsorption/ reaction at sensor surface).
If some decay reaction occurs at the interface between pore space and solid, with rate ρ, the following holds at the boundary:

$$\frac{\partial C}{\partial \vec{r}} - \frac{\rho}{D_P} C = 0$$

Where D_p is the diffusion coefficient in the unconstrained pore fluid.

In the papers central to this work, Bergman and Dunn look at the case of a porous system consisting of impenetrable obstacles imbedded within the pore fluid where a reaction may occur at the pore-solid interface. They overcome both the issue of complex boundary conditions and the difficulty of including a surface-localised reaction term with the following two key features:

1. They find diffusion eigenstates for a system where there is no surface reaction by using the chemical potential diffusion equation rather than the equation for the particle concentration. The chemical potential does not suffer the interfacial discontinuities which are so problematic when dealing with concentration.
2. They then calculate the eigenstates for the system where a surface reaction may occur by expanding them in terms of those calculated for the same system but where no reaction occurs.

The theory is easily extended to the case where there are two penetrable phases with a defined partition coefficient and the theory for this more general set up is now summarised. The theory presented here is also an extension of the original model in that it includes a bulk, phase-dependent reaction as in equation 3.3 above.

(3.3.2) Finding diffusion eigenstates

Equation 3.4 is a general trial solution of equation 3.3, consisting of time and space dependent parts and where λ is a constant and $\phi_\lambda(\vec{r})$ is some function of space:

$$C(\vec{r},t) = \phi_\lambda(\vec{r})e^{-\lambda t}$$ Equation 3.4

Substituting into equation 3.3 and rearranging gives the following eigenvalue equation:

$$-\lambda\phi_\lambda(\vec{r}) = \nabla\cdot(D(\vec{r},t)\nabla\phi_\lambda(\vec{r})) - k(\vec{r})\phi_\lambda(\vec{r})$$

Here the function, i.e. the eigenfunction set, is the space-dependent part of the trial solution, $\phi_\lambda(\vec{r})$, and λ is the eigenvalue.

Following the definition of the diffusion propagator and considering the orthonormality of the set of eigenfunctions, the solution of equation 3.3 can then be expressed as a sum of all the eigenfunctions weighted by the corresponding eigenvalue as:

$$C(\vec{r},\vec{r}',t) = \sum_\lambda e^{-\lambda t}\phi_\lambda(\vec{r})\phi_\lambda^*(\vec{r}')$$ Equation 3.5

Hence the concentration variation with position and time can be calculated via the calculation of a truncated set of space dependent functions $\phi_\lambda(\vec{r})$ and the set of eigenvalues λ.

It is interesting to note that this method is analogous to that used for solving the Schrödinger equation for a quantum particle in a potential field, see for example [39]. The method of finding eigenstates is prevalent in solving such differential equations due to the reduction of a potentially highly complex equation to a system of linear algebraic equations.

(3.4) Theory

(3.4.1) The diffusion equation in terms of chemical potential

The diffusion equation can be written in terms of the chemical potential, $\mu(\vec{r},t)$, as follows: $$n_\mu(\vec{r})\frac{\partial\mu(\vec{r},t)}{\partial t} = \nabla\cdot\left[D(\vec{r},t)n_\mu(\vec{r})\nabla\mu(\vec{r},t)\right] - k(\vec{r})n_\mu(\vec{r})\mu(\vec{r},t)$$ Equation 3.6

where $n_\mu(\vec{r})$ is the local value of thermodynamic derivative equal to $\frac{\partial C}{\partial\mu}$.

By allowing diffusion to occur into the solid phase and instead presuming the thermodynamic derivative tends to zero in the solid, the chemical potential $\mu(\vec{r},t)$ will be a continuous function of $\vec{r}$ for all space and hence equation 3.6 holds for the entirety of the system (not just the pore space) such that the eigenstates method can now be applied.

(3.4.2) Use of a periodic microstructure

The spectrum of eigenstates is discrete only for a periodically repeating pore space – for a disordered porous system the summation in equation 3.5 is replaced by an integration and the solution is intractable.

For a periodic microstructure the eigenfunction, $\phi_\lambda(\vec{r})$, can be written in Bloch form (or Bloch-Floquet form) i.e. the product of a plane wave function and a function with the same periodicity as the material [40]:

$$\phi_\lambda(\vec{r}) \to \phi(\vec{r})_{n\vec{q}}\, e^{i\vec{q}\cdot\vec{r}}$$
$$\lambda \to \lambda_{n\vec{q}} \qquad \text{Equation 3.7}$$

The eigenvalues fall into bands - where *n* is the band index and $\vec{q}$ is a wave-vector in the 1st Brillouin zone (as all solutions can be completely characterized by their behaviour in the 1st Brillouin zone).

A Fourier series expansion can then be used to define the plane wave function $\phi(\vec{r})_{n\vec{q}}$ as $\varphi_{n\vec{q}}(\vec{r}) = \sum_g \tilde{\phi}_{n\vec{q}}(\vec{g}) e^{i\vec{g}\cdot\vec{r}}$ Equation 3.8

Where the sum is over the set of reciprocal lattice vectors ($\vec{g}$).

(3.4.3) The eigenvalue equation

The Fourier coefficients $\tilde{\phi}_{n\vec{q}}$, discussed above, satisfy the following matrix eigenvalue equation (written in matrix notation):

$$\lambda_{n\vec{q}} \hat{W} \tilde{\phi}_{n\vec{q}} = \hat{\Gamma} \tilde{\phi}_{n\vec{q}} \qquad \text{Equation 3.9}$$

In order to derive this equation, from equation 3.6, the following steps must be taken.

1. Firstly substituting in the trial solution equation 3.4 into equation 3.6, as was done in the first section, gives the eigenstate equation:

$$-\lambda n_\mu(\vec{r})\phi_\lambda(\vec{r}) = \nabla[D(\vec{r}) n_\mu(\vec{r}) \nabla \phi_\lambda(\vec{r})] - k(\vec{r}) n_\mu(\vec{r}) \phi_\lambda(\vec{r}) \qquad \text{Equation 3.10}$$

2. To continue, (for our two phase system) the phase 1 indicator function (or characteristic function) is introduced:

$$\theta_1(\vec{r}) = \begin{cases} 1 & \textit{In phase 1} \\ 0 & \textit{In phase 2} \end{cases}$$

Similarly an expression can be written for a phase 2 indicator function and the functions of the two phases are related as $\theta_1(\vec{r}) = 1 - \theta_2(\vec{r})$

Following this, general expressions can be formed for the diffusivity, rate constant and thermodynamic derivative in terms of their bulk properties:

$$D(\vec{r}) = D_1\theta_1(\vec{r}) + D_2\theta_2(\vec{r})$$

$$k(\vec{r}) = k_1\theta_1(\vec{r}) + k_2\theta_2(\vec{r})$$

$$n_\mu(\vec{r}) = n_{\mu 1}\theta_1(\vec{r}) + n_{\mu 2}\theta_2(\vec{r})$$

3. The next step is to define

$W(\vec{r}) = 1 - w\theta_2(\vec{r})$, $U(\vec{r}) = 1 - u\theta_2(\vec{r})$ and $X(\vec{r}) = 1 - x\theta_2(\vec{r})$

where $w = 1 - z$; $u = 1 - \frac{zD_2}{D_1}$; $x = 1 - \frac{zk_2}{k_1}$ and $z = \frac{n_{\mu 2}}{n_{\mu 1}}$

Note, this implies knowledge of the bulk diffusivities and rate constants of the unconfined phases and the ratio of thermodynamic derivatives, *z*, giving the preference of the gas to be in phase 1 compared to phase 2, i.e. the partition coefficient.
Note that in the case of impenetrable obstacles, the impenetrable phase is phase 2.

These expressions, along with the forms for $D(\vec{r})$, $k(\vec{r})$ and $n_\mu(\vec{r})$ can be used to transform equation 3.8 to give:

$$-\lambda W(\vec{r})\varphi_\lambda(\vec{r}) = D_1\nabla\cdot[U(\vec{r})\nabla\phi_\lambda(\vec{r})] - k_1X(\vec{r})\phi_\lambda(\vec{r}) \qquad \text{Equation 3.11}$$

4. Finally the use of a periodic structure is realised and equations 3.7 and 3.8 are substituted into equation 3.10. The indicator function is also expanded in terms of a Fourier series such that $W(\vec{r})$, $U(\vec{r})$ and $X(\vec{r})$ can now be written in integral form.

$$\theta_2(\vec{r}) = \sum_g \theta_g^{(2)}(\vec{g})e^{i\vec{g}\cdot\vec{r}} \quad \text{where} \quad \theta_g^{(2)}(\vec{g}) = \frac{1}{V_a}\int_{V_a} dV\theta_2(\vec{r})e^{-i\vec{g}\cdot\vec{r}}$$

Following this, the differential equation can be translated to a infinite set of linear algebraic equations and the move is made to a matrix representation. After a little effort the matrix equation 3.9 is obtained:

$$\lambda_{nq}\sum_{g'}W_{gg'}\tilde{\phi}_{nq}(\vec{g}') = \sum_{g'}\Gamma_{gg'}\tilde{\phi}_{nq}(\vec{g}')$$

Where $W_{gg'}$ comes straightforwardly from the expression for $W(\vec{r})$ above as $W_{gg'} = \delta_{gg'} - w\theta^{(2)}_{g-g'}$ (where the 2 superscript indicates the phase 2 medium).

Similarly $U_{gg'} = \delta_{gg'} - u\theta^{(2)}_{g-g'}$ and $X_{gg'} = \delta_{gg'} - x\theta^{(2)}_{g-g'}$ from which the $\hat{\Gamma}$ matrix is constructed. Note to complete this stage, as well as putting the indicator into an integral form, one must also account for the differentiation of the $U(\vec{r})$ function i.e. the $D_1\nabla\cdot[U(\vec{r})\nabla\phi_\lambda(\vec{r})]$ term in equation 3.11.:

$$\Gamma_{gg'}(\vec{q}) = D_1(\vec{g}+\vec{q})\cdot(\vec{g}'+\vec{q})(\delta_{gg'} - u\theta^{(2)}_{g-g'}) + k_1(\delta_{gg'} - x\theta^{(2)}_{g-g'}) \qquad \text{Equation 3.12}$$

Equation 3.9 is an infinite set of linear equations, a truncated set of which can be solved by matrix methods as discussed in section 3.5. Once the Fourier coefficients are found, they can be put back into the original form to find the diffusion propagator, the effective diffusion and rate coefficients. Note it is also possible to find the time-dependent diffusion coefficient through its relation with the PFGSE (pulsed field-gradient spin-echo) amplitude [41]. However, the variation of the diffusion coefficient is found to occur over a much short timescale than is relevant to sensor as considered here and hence is not investigated here.

(3.4.4) Extension of model to include an interface reaction [16]

To extend the model to include the occurrence of surface decay of rate ρ, two sets of eigenvalues and eigenfunctions are now required (note in this instance the discussion is restricted to impenetrable obstacles and the impenetrable phase is referred to as phase 2):

1. $\lambda\phi_\lambda + D_1\nabla^2\phi_\lambda = 0$ inside the pore space.

   $\frac{\partial\phi_\lambda}{\partial n} = 0$ at the pore-matrix interface.

2. $\mu\psi_\mu + D_1\nabla^2\psi_\mu = 0$ inside the pore space.

   $\frac{\partial\psi_\mu}{\partial n} + \frac{\rho}{D_1}\psi_\mu = 0$ at the pore-matrix interface.

The objective is then to express the second set of eigensolutions in terms of the first set of eigensolutions which are those calculated following the method above. This is done by taking the overlap integrals between the two function types and applying Green's theorem to form two different transformations which can then be combined (again substituting in periodic forms) to obtain a second matrix eigenvalue equation with eigenfunctions A_m and eigenvalues $\frac{(\mu_{nq} - \lambda_{mq})}{\rho}$ [2]:

$$(\mu_{nq} - \lambda_{nq})A_m^{(n)}(\vec{q}) = \rho \sum V_{mp}(\vec{q}) A_p^{(n)}(\vec{q})$$

Where the $\hat{V}$ matrix has the form:

$$V_{nm}(\vec{q}) = 4\sum_g \sum_{g'} \tilde{\varphi}_{nq}^*(\vec{g}) K(\vec{g} - \vec{g}') \tilde{\phi}_{mq}(g') \qquad \text{Equation 3.13}$$

In turn K is defined below as the closed surface integral for the geometry of the system being simulated:

$$K(\bar{g}) \equiv \frac{1}{V_a} \oint_{\partial V_p \cap V_a} e^{-i\vec{g}\cdot\vec{r}} ds$$

The actual eigenfunctions for the interface decay system are found as:

$$\psi_{n\vec{q}} = \sum_m A_m^{(n)}(\vec{q}) \phi_{m\vec{q}}$$

As is described in the next section, the properties of a two-phase system can now be found where either a phase-dependent or a surface-localised occurs.

(3.5) Computational Procedure

(3.5.1) System of two penetrable phases with phase-dependent reactions

Following the theory described above, it is possible to compute the effective diffusivity and rate constant for a periodic, 3-dimensional, 2-phase composite system in which either phase (or both) may be penetrable and where a phase-dependent reaction may occur. An overview of the computational procedure is now given and the program process is summarised as a flow chart in figure 3.2, additionally the full C-code is given on CD.

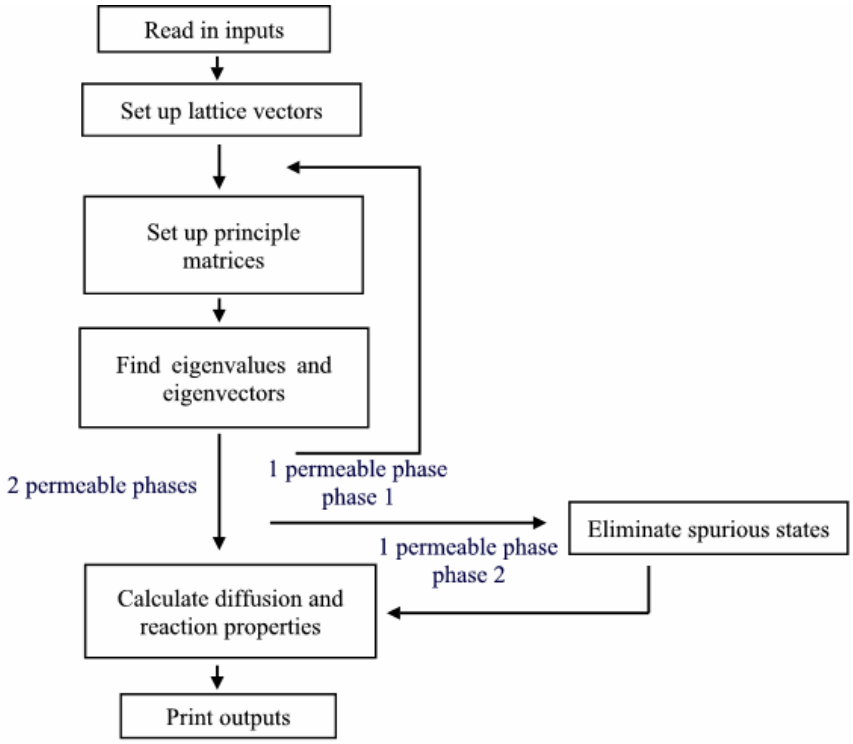

Figure 3.2: Flow chart to represent the computational process for calculating bulk diffusion and reaction coefficients following the method of diffusion eigenstates.

Stage 1: Setting up the matrix equation $\lambda_{n\vec{q}}\hat{W}\tilde{\phi}_{n\vec{q}} = \hat{\Gamma}\tilde{\phi}_{n\vec{q}}$

At this stage scalar inputs D_1, D_2, K_1, K_2, z, a, N_g; vectors $\vec{g}$ and $\vec{q}$ and the matrix $\theta^{(2)}_{g-g'}$ are required and are now discussed. A summary is given in table 3.1.

(a) The bulk diffusion coefficients D_1, D_2, of the gas in the two phases and the ratio of thermodynamic derivatives, z, as discussed in section 3.3, are user defined along with dimensionless bulk rate constants $K_1 = k_1 a^2 / D_1$ and $K_2 = k_2 a^2 / D_2$ where a is the unit cell length. The use of dimensionless variables in advantageous in removing trivial variation from the results data, i.e. that a molecule that diffuses slowly will react for a longer period is trivial and is eliminated using the dimensionless form which divides through by the diffusivity.

Also the quality of the calculation is set via the choice of N_g which determines the number of reciprocal lattice vectors used for the calculation as shown below. A good convergence of the different calculated properties was achieved with N_g =6 and is hence

used for all results presented here. Figure 3.3 demonstrates the convergence of the calculated effective diffusivity with increasing N_g. Good convergence is achieved for each of the different cases with $N_g = 6$.

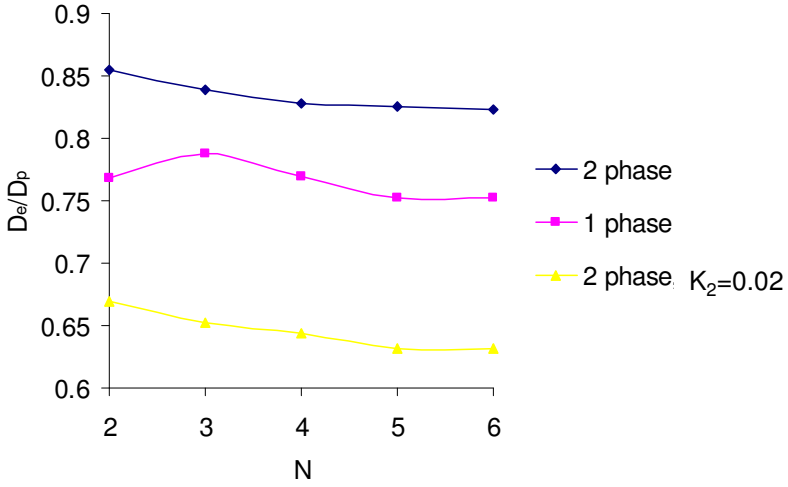

Figure 3.3: Convergence of the calculated bulk effective diffusion coefficient, D_e, with the number of lattice vectors, N_g, used for the calculation, for a system of solid spheres and both a passive and reactive case of a system of penetrable spheres (where there is a partitioning between phases of z = 5 ($z = n_{\mu 2} / n_{\mu 1}$) and equal diffusivity in the two phases).

(b) The $\vec{g}$ vectors form the truncated set of reciprocal lattice vectors which, for the case of the simple cubic lattice, have the form:

$$\vec{g} = \frac{2\pi}{a}(n_x, n_y, n_z)$$

Where $n_x, n_y, n_z = -N_g, ..., 0, ..., N_g$ so the size of the matrices involved in the calculations is given by $(2N_g + 1)^3$.

Note, if different crystal symmetry is required the appropriate reciprocal lattice vectors obviously must be used – this will also affect the calculation of the indicator function matrix (discussed for the simple cubic lattice below). Also for symmetries lower than simple cubic the diffusivity becomes a tensor quantity.

(c) $\vec{q}$ is a wave-vector in the 1st Brillouin zone. In order to evaluate certain properties, as discussed below, $\vec{q}$ should be small compared to the inverse length of the pores. However, $\vec{q}$ should not be taken as being too close to zero due to the high degeneracy of eigenvalues associated with the high symmetry of the zero wave-vector point in

reciprocal space. Preliminary tests were performed to verify the validity of the $\vec{q}$ value used, results of which are presented below.

(d) The elements of the $\theta^{(2)}_{g-g'}$ matrix are the Fourier coefficients of the indicator function for phase 2 given by:

$$\theta^{(2)}_{g}(\vec{g}) = \frac{1}{V_a}\int_{V_a} dV\theta_2(\vec{r})e^{-ig\cdot r} \qquad \text{Equation 3.14}$$

It is through the indicator function that information about the geometry of the system is included into the model. It must be specified whether this choice refers to phase 1 or phase 2, for example if spherical geometry is selected for phase 1 then the unit cell will consist of a centrally placed sphere of phase 1 embedded in phase 2 medium. The integral, equation 3.14, can be solved analytically in many cases by exploiting symmetries of the geometry, forms for the geometries used here are taken from [42].

.

Potentially any system geometry could be solved for by employing numerical methods such as 3-dimensional Monte Carlo numerical integration. However, here only exactly solvable cases are considered.

Stage 2: Solving the matrix equation $\lambda_{n\vec{q}}\hat{W}\tilde{\phi}_{n\vec{q}} = \hat{\Gamma}\tilde{\phi}_{n\vec{q}}$

The matrix equation can now be solved by making the following considerations to find the eigenvalues λ_{nq} and eigenfunctions $\tilde{\phi}_{n\vec{q}}$.

(a) The matrix equation (equation 3.9) is not in fact in a desirable form as most eigenstate finding algorithms work for the standard form: $\hat{A}\cdot\vec{x} = \lambda\vec{x}$.

As is generally the case with matrix problems, some sort of factorisation is required to convert the matrix to the standard form from which calculations can be carried out more efficiently.

Commonly used when solving linear equations and also for inverting matrices, finding determinants etc, are factorisation methods such as the LU (lower upper) factorisation [43], where a matrix is written as the product of a lower triangular and upper triangular matrix. Here a factorisation of the $\hat{W}$ matrix is performed.

If a matrix is positive definite and also symmetric, the Cholesky factorisation method [44] can be applied to decompose the matrix as the product of a unique lower triangular matrix and its transverse. This is a special case of the LU factorisation which requires only half of the arithmetic operations – around $N^3/3$. Here the routine *choldc* [44] has been used to perform the Cholesky decomposition of the $\hat{W}$ matrix as $\hat{W} = \hat{R}^{+}\hat{R}$.

Whilst this method is efficient and on the whole numerically highly stable, there is an issue with the value of *w* used for cases where one phase is impenetrable as if *w* is too close to 1 (i.e. $w = 1 - \frac{n_{\mu 2}}{n_{\mu 1}}$) the factorisation becomes inaccurate. Instead a small but finite value for the partition coefficient must be used. No such restriction is placed on the value of *u* and although realistically $n_{\mu m} \to 0$ before $D_m \to 0$ it is argued in [3] that no advantage is found in having a non-zero D_m and in general the validity of this approximation is approved. The Cholesky method also has the added benefit of easy inversion of the resultant triangular $\hat{R}$ matrix as required for the next step of the computation. It was verified that the original $\hat{W}$ matrix could be reconstructed by calculating the product $\hat{W} = \hat{R}^{+}\hat{R}$.

(b) The following matrix can now be constructed:

$$\hat{\Lambda} = (\hat{R}^{-1})^{+}\hat{\Gamma}\hat{R}^{-1}$$

So that the eigenvalue equation can now be written in the desired form given above as:

$$\lambda_{nq}(\hat{R}\tilde{\phi}_{nq}) = D_p\hat{\Lambda}(\hat{R}\tilde{\phi}_{nq}) \qquad \text{Equation 3.15}$$

to which standard methods can be applied to find eigenvalues λ_{nq} / D_p and eigenvectors $\hat{R}\tilde{\phi}_{nq}$.

(c) Essentially finding eigenvalues and eigenvectors is a problem of root finding – the $\hat{\Lambda}$ determinant can be expanded as an Nth degree polynomial in λ, the roots of which are the eigenvalues. However, this is not an advantageous route for computational efficiency. Instead, methods for reducing the matrix to a simpler form are again employed. The routine *tred2* [45] is used to reduce the $\hat{\Lambda}$ matrix to a tridiagonal form. This routine is based around the Householder algorithm which is essentially a series of

orthogonal reflections of the vectors that comprise the matrix. The operation count for this routine is $4N^3/3$ in the limit of large N.

(d) The actual eigenvalues and eigenvectors are then found using *tqli* routine [46] again using Householder transformations, here as part of the QL algorithm (with implicit shifts) which is based around decomposition to a triangular matrix (the L matrix) and an orthogonal (Q) matrix. This stage uses around $3N^3$ operations. Again, the routine has been verified, here by testing the equality of the two vectors constructed for each eigenvector $\tilde{x}$ as $\hat{\Lambda}\tilde{x}$ and $L\tilde{x}$ (where L is the corresponding eigenvalue).

(e) Finally the eigenstates are sorted into ascending order using a standard sorting routine.

Stage 3: Calculating diffusion properties

With a set of eigenvectors and eigenvalues now in hand, it is possible to calculate several properties of the system.

(a) The bulk effective stationary diffusion coefficient D_e at long times can be calculated in the limit of small $\vec{q}$ following the simple form relating it to the lowest lying eigenstate [47]:

$$\lambda_{0\vec{q}} = \lambda_{00} + D_e|\vec{q}|^2 + O(|\vec{q}|^4)$$

It was argued above that the $\vec{q}$ value should not be too small. Here we note a second restriction, i.e. it cannot be too large so as to be able to calculate the bulk effective diffusivity according to the approximation given above. Figure 3.4 shows the range of stability of the $\vec{q}$ value. All calculations were carried out with $\vec{q}a = 0.3$.

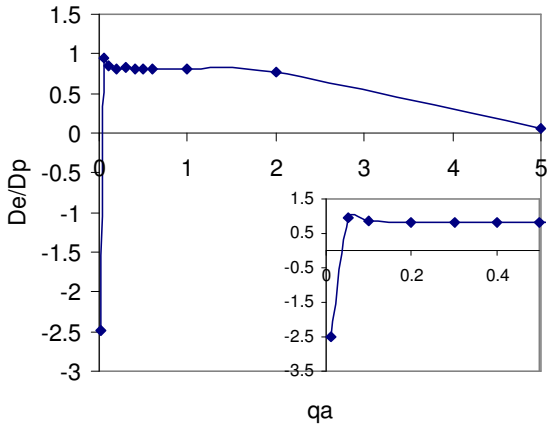

Figure 3.4: Calculated bulk effective diffusion coefficient, D_e, as a function of $\vec{q}a$. Calculated for a system of impenetrable spheres.

(b) The diffusion propagator can be found by forming the expansion given in equation 3.5 (true also for the set of eigenfunctions of the interface decay system):

$$G(\vec{r},\vec{r}',t) = \sum_{\lambda} e^{-\lambda t}\phi_{\lambda}(\vec{r})\phi_{\lambda}^{*}(\vec{r}')$$

The set of space-dependent functions, $\phi_{n\vec{q}}(\vec{r})$, can be calculated from the set of eigenfunctions that have been calculated so far, $\tilde{\phi}_{n\vec{q}}(\vec{g})$, following equation 3.8:

$$\phi_{n\vec{q}}(\vec{r}) = \sum_{g} \tilde{\phi}_{n\vec{q}}(\vec{g})e^{i\vec{g}\cdot\vec{r}}$$

The following substitution can be made for the complex exponential term:

$$e^{i\vec{g}\cdot\vec{r}} = \cos(\vec{g}\cdot\vec{r}) + i\sin(\vec{g}\cdot\vec{r})$$

This gives the following expression for the propagator, where it is confirmed in the course of the computation that the imaginary part of the concentration summation is equal to zero:

$$G(\vec{r},\vec{r}',t) = \sum_{\lambda} e^{-\lambda t}\sum_{g}\sum_{g'} \tilde{\varphi}_{nq}(\vec{g})\tilde{\phi}_{mq}(\vec{g}')[\cos(\vec{g}\cdot\vec{r})\cos(\vec{g}'\cdot\vec{r}') + \sin(\vec{g}\cdot\vec{r})\sin(\vec{g}'\cdot\vec{r}')]$$

Here $G(\vec{r},\vec{r}',t)$ is, of course, the chemical potential diffusion propagator, whereas it is actually the concentration propagator that is of interest. In fact the two are equal if the initial and final positions at which the propagator is evaluated are in the same phase. If this is not the case, the calculated propagator must be weighted by the partition coefficient according to the associated position vector. See line 651 of the main code.

(c) Finally the effective rate constant may be calculated by considering the concentration change at points on a grid. For low symmetry systems such as one of

spherical obstacles the computational effort can be greatly reduced by considering a 2-dimensional grid and then transforming this to represent the 3-dimensional geometry. The code written to perform this is given in figure 3.5 below. The space-dependent eigenfunctions are calculated for the each space point on the grid and the average concentration over the points is then found and normalised to the average concentration where no reaction occurs, this final concentration value is denoted $G_{av}(t)$.

The effective rate constant is then calculated as:

$$k_e = -\frac{\log(G_{av}(t_2)) - \log(G_{av}(t_1))}{(t_2 - t_1)}$$

```
if( i == 0 || i == 2*n_x || j == 0 || j == 2*n_y)
diffn_prop_tot+= 2*fabs(diffn_prop_re_space[i,j]);

else{
for (n=1; n<=((2*n_x/2)); n++)
{
if (i== n || i == 2*n_x-n || j == n || j == 2*n_y-n)
diffn_prop_tot+= 6*(n+1)*fabs(diffn_prop_re_space[i,j]);

else if (i==((2*n_x/2)) && j==((2*n_y/2)))
diffn_prop_tot+= (6*n+1)*fabs(diffn_prop_re_space[i,j]);
}
}
if (j<2*n_y)
counter ++;
}
if (i<2*n_x)
counter ++;
}
```

Figure 3.5: Code written to transform 2-dimensional concentration profile to 3-dimensions where there is spherical symmetry (line 35 of function *find_conc.c*).

Figure 3.6 shows provides some analysis of the method accuracy, 3.5(a) shows that the graph of log(G) as a function of time does indeed give a straight line and figure 3.6(b) shows the convergence of the effective rate constant with grid size. A good convergence of the calculated rate constant was achieved with $(25+1)^2$ grid points which is hence used for all results presented here.

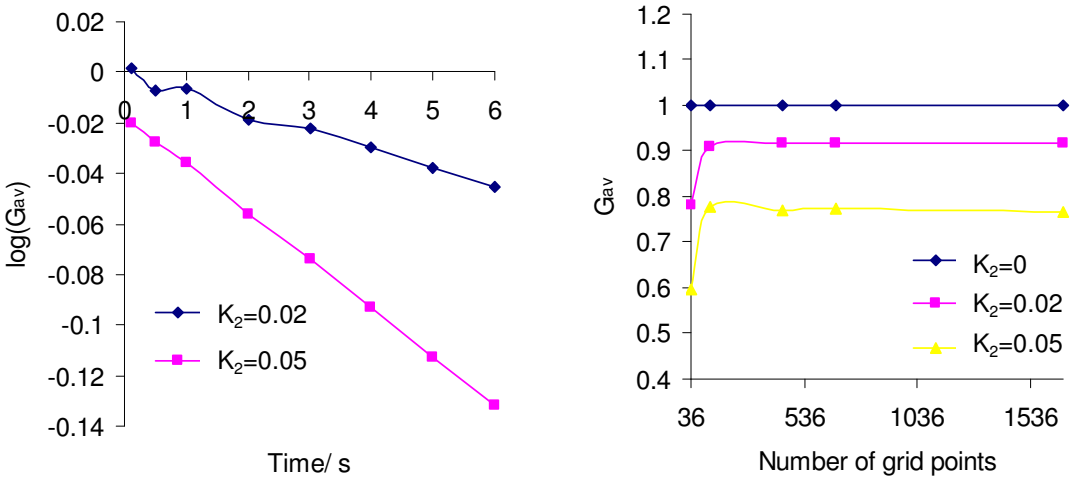

(a) (b)

Figure 3.6: Averaged concentration as a function of (a) time with $(25+1)^2$=676 grid points and (b) the number of grid points at time 5s. (Calculated for a system of two penetrable phases with porosity 0.48 and where $z = 5$ ($z = n_{\mu 2} / n_{\mu 1}$)and D_1=D_2)

(3.5.2) System of impenetrable obstacles with a surface reaction

It is possible to follow the same three stages as above with modifications as follows in order to extend the calculation to calculate the diffusional properties of the system where a surface-localised reaction occurs.

Stage 1: Setting up the matrix equation $\hat{V}A_\lambda = \dfrac{(\mu_{n\bar{q}} - \lambda_{n\bar{q}})}{\rho} A_\lambda$

The only additional inputs here (other than of course the eigenvalues and eigenvectors for the ρ = 0 stage) are the scalar reaction rate, ρ, and the $\hat{K}$ matrix and here the dimensionless rate parameter $\dfrac{\rho a}{D_1}$ is defined. For now, the geometries considered where a surface reaction may occur are non-overlapping and overlapping spheres. The $\hat{K}$ matrix has the form:

$$K(\bar{g}) \equiv \frac{1}{V_a} \oint_{\partial V_p \cap V_a} e^{-i\vec{g}\cdot\vec{r}} ds$$

This expression can be evaluated analytically for the case of non-overlapping spheres as:

$$K(\bar{g}) \equiv \frac{4\pi R}{a^3} \frac{\sin(|\vec{g}|R)}{|\vec{g}|}$$ where R is the sphere radius.

For overlapping spheres, we must account for the loss of surface area occurring over the regions where the spheres are overlapping. The expression for one of these segments, $K_o(\bar{g})$, six of which must be subtracted from the previous expression and which must be integrated numerically, is as follows:

$$K_o(\bar{g}) \equiv \frac{2\pi}{a^3}\frac{\sin g(|\vec{g}|R)}{|\vec{g}|R}\int_{\pi-\sin^{-1}(a/(2R))}^{\sin^{-1}(a/(2R))}\frac{a\cos\theta}{2\sin\theta}\sqrt{\left(\frac{a}{2\sin\theta}\right)^2+\left(\frac{a\cos\theta}{2\sin^2\theta}\right)^2}\,d\theta$$

The numerical integration was performed following Simpson's rule using the routine *qsimp* [48].

The $\hat{V}$ matrix can then be constructed following equation 3.13 by performing simple matrix multiplications.

Stage 2: Solving the matrix equation $\hat{V}A_\lambda = \frac{(\mu_{n\bar{q}} - \lambda_{n\bar{q}})}{\rho}A_\lambda$

Steps (c) to (e) from stage 2 of section 3.5.1 are now followed to solve the matrix equation. Note the eigenvalues that are given following these steps have the form $\frac{(\mu_{nq} - \lambda_{mq})}{\rho}$.

Stage 3: Calculating diffusion properties

If one phase is impenetrable a further consideration which must be made is the occurrence of spurious states as a consequence of using the chemical potential diffusion equation in order to deal with the stringent boundary conditions.

In principle, it is possible to identify spurious eigenstates using the following relation, as calculated in function *spurious*:

$$\phi_{nq}^{+}\hat{W}^2\phi_{nq} = \begin{cases} 1 & true \\ 1-w & spurious \end{cases}$$

However in practice the distinction becomes "fuzzy" due to the truncation of the matrices. Fortunately, this lack of distinction only becomes problematic for large eigenvalues in which case their contribution is not very significant (as we are concerned with $e^{-\lambda t}$) and hence these states do not actually need to be removed.

It was found that the low lying spurious states were much more identifiable through the calculation where surface decay is possible – even where the surface decay coefficient

was set to zero. Hence for all calculations of impenetrable obstacles, both parts of the computation where performed. Note it has been confirmed that the two stages give the same result by considering cases where it was possible to distinguish between spurious and real states.

It is now possible to calculate the diffusion properties as discussed in stage 3 of section 3.5.1. An example input file is given in figure 3.7. Note computation times range from about 10 minutes, if just the effective diffusivity without surface reaction is to be calculated, to about an hour for finding rate constant with surface reaction on a 4GB processor.

Input	Description
D_1	Diffusion coefficient in the pore space – for a two phase medium this is the phase in which gas is released and subsequently any properties are measured.
D_2	Diffusion coefficient in the solid matrix or second penetrable phase.
z	The ratio of thermodynamic derivatives in the two phases (phase 2/ phase1).
a	The unit cell length.
N_g	The size of the truncated set of the lattice vectors and hence the size of the matrices involved in the calculation.
$\vec{g}$	The lattice vectors, simple cubic lattice form given above.
geometry dimensions	Dependent on the geometry to be calculated for, for example sphere radius.
r_vec_init(x, y, z)	Point of gas release.
$k_1 a^2 / D_1$, $k_2 a^2 / D_2$	Dimensionless, non-localised phase-dependent reaction constants.
$\frac{\rho a}{D_1}$	Dimensionless form for rate constant at surface.

Table 3.1: Summary of program inputs

Function	Description
choldc.c [43]	Performs Cholesky decomposition and matrix inversion.
tred2.c [44]	Reduces N x N matrix to tridiagonal form based on the Householder algorithm.
tqli.c [45]	Determines eigenvalues and eigenvectors using QL algorithm with implicit shifts (requires real symmetric matrix on input).

sort.c	Sorts the eigenstates into ascending order.
bessj1.c [49]	Finds the Bessel function of order 1 as required in the evaluation of cylindrical and overlapping sphere geometries.
qsimp.c [48]	Performs numerical integration of a function over the closed interval [*A*, *B*] using Simpson's rule.
find_transpose.c	Finds transpose of a square matrix.
matrix_mult.c	Finds the product of two square matrices of the same dimension.
vec_dot.c	Calculates the dot product between two vectors.
reader.c [50,51]	Reads in inputs from file (see figure 3.7).
find_porosity.c	Calculates system porosity.
geom_calc.c	Finds the $\theta^{(2)}_{g-g'}$ matrix as given by equation 3.14.
spurious.c	Identifies and eliminates spurious eigenstates.
find_conc.c	function to calculate average concentration converting 2D grid to 3D for spherical geometry

Table 3.2: Summary of program functions

```
# anything after hash ignored

# matrix size for calculation - needs to be calculated as
pow((2*NMAX+1),3) where NMAX is the number of lattice points in
any one direction index. Chose from 9, 125, 343, 729, 1331, 2197
matrix_size 2197

# unit cell size
unit_cell_length 1e-5

# chose geometry. Chose from Options sphere, ellipse, rectangle,
channel_and_pore, square_pore_channel
geometry sphere

# for sphere, enter radius (srad).
srad 5e-6

# extra dimensions for ellipse and rectangle. For channels and
pores x is pore size, y is channel width, z is channel length.
#x_length 4e-6
#y_length 1e-6
#z_length 3e-6

# for cylinder enter cylinder height and radius.
#c_radius 1e-6
#c_height 1e-5

# decide whether the shape is phase 1 or phase 2. NOTE: a shape
of phase 1 which doesn't touch unit cell edge and with d_2 = 0
gives an unconnected pore system.
```

```
phase 2


# diffusion coefficient of gas in homogeneous phase 1.
d_1 1e-5

# diffusion coefficient of gas in homogeneous phase 2.
d_2 1e-5

# partition coefficient.
partition_coeff 5

# bulk phase dependent reaction rate constant for reaction
occurring in phase 1.
1_macro 0.

# bulk phase dependent reaction rate constant for reaction
occurring in phase 2.
2_macro 0.02

# chose whether want to perform surface reaction phase of
calculation. NOTE: presently must be spherical geometry.
surface_reaction no

# dimensionless reaction rate for surface localised reaction.
rate_reaction 0.0

# point of initial gas insertion (only need if doing conc).
init_position 5e-6 5e-6 5e-6

# decide whether want to calculate concentration profile (and
hence rate constant).
concentration yes

# enter times at which to calculate concentration.
t_1 0.1
t_1 5

# enter q_vector value. Will be divided by length of unit cell
q_vector 0.1 0. 0.
```

Figure 3.7: Example input file.

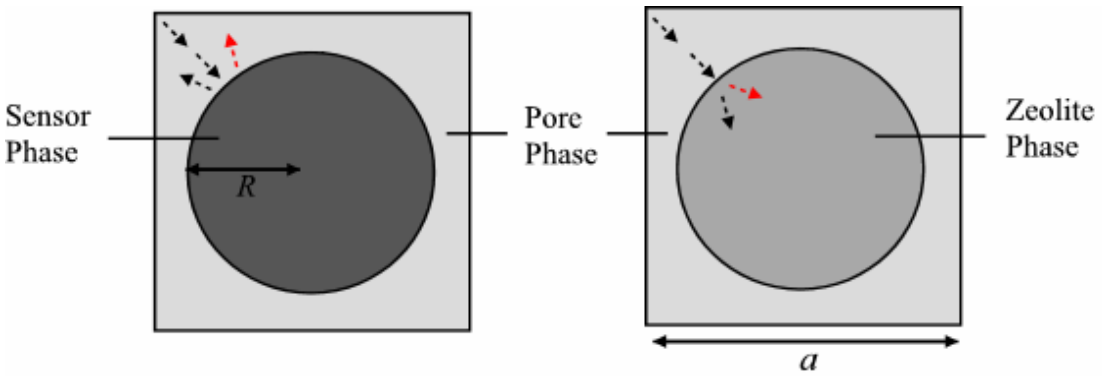

Figure 3.8: 2-D representation of the model systems. Depicted is a single unit cell comprising of a spherical object, surrounded by the pore fluid. A reaction either occurs (a) at the sensor surface or (b) within the zeolite phase. (Only one point of gas release is shown, due to the periodic nature, gas will in fact be introduced from each corner.)

(3.6) Results

(3.6.1) Modelling the sensor layer

As illustrated in figure 3.8(a), the sensor layer is represented by a system of impenetrable obstacles surrounded by the pore fluid in which the test gas has a bulk diffusivity D_p. A reaction of dimensionless rate $\frac{\rho a}{D_p}$ may occur at the surface of the solid phase – the surface area of the solid phase hence being a variable of interest, along with the porosity of the system. Results of the calculated bulk effective diffusivity and bulk effective rate constant are hence presented as functions of these two variables. The formulae for porosity and surface to volume ratio are given in table 3.3 for non-overlapping and overlapping spheres. To compare systems of equal porosity but different surface to volume ratio, the ratio in the table is divided by the unit cell volume and multiplied by a unit volume. The high surface area system will be comprised of smaller particles than the low surface area system that has the same porosity.

	$0 \le \frac{R}{a} \le \frac{1}{2}$	$\frac{1}{2} < \frac{R}{a} \le \frac{1}{\sqrt{2}}$
ϕ	$1 - \frac{4\pi}{3}\left(\frac{R}{a}\right)^3$	$1 + \frac{\pi}{4} - 3\pi\left(\frac{R}{a}\right)^2 + \frac{8\pi}{3}\left(\frac{R}{a}\right)^3$
$\frac{aS_p}{V_p}$	$\frac{4\pi\left(\frac{R}{a}\right)^2}{1 - \frac{4\pi}{3}\left(\frac{R}{a}\right)^3}$	$\frac{2\pi\left(\frac{R}{a}\right)\left(3 - 4\left(\frac{R}{a}\right)\right)}{1 - \frac{\pi}{4} - 3\pi\left(\frac{R}{a}\right)^2 + \frac{8\pi}{3}\left(\frac{R}{a}\right)^3}$

Table 3.3: Forms for porosity, ϕ, and pore surface to volume ratio, $\frac{S_p}{V_p}$, for overlapping and non-overlapping spheres of radius *R*.

Figure 3.9 gives the calculated bulk effective diffusivity, D_e/D_p, as a function of porosity, for a system in which no reaction occurs. The diffusivity increases as the pore volume increases as one would expect. Also given is the diffusivity for a system of cylindrical pores – in this case the bulk diffusivity falls off more slowly as the pore fraction is reduced, a result of the system being less tortuous.

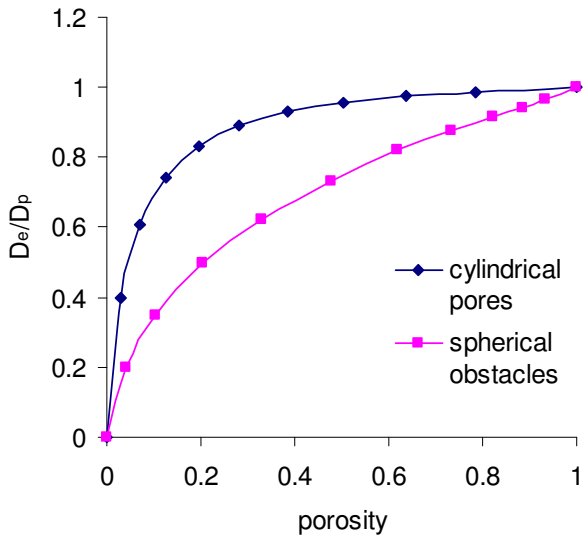

Figure 3.9: Calculated effective diffusivity for the two phase system relative to the pore phase diffusivity, D_e/D_p, for as a function of porosity for systems of different geometry.

If a reaction occurs at the pore-solid interface, the effective diffusivity will depend on the rate of this reaction and also the surface-to-volume ratio in addition to the porosity. Figures 3.10 (a) and (b) give the diffusivity for systems of different porosity for two

different surface-to-volume ratios where a surface-localised reaction occurs of dimensionless rate $\frac{\rho a}{D_p}$. For the majority of cases, the effect of the reaction is to reduce the effective diffusivity and it is observed that the extent to which this occurs is greater where there is a higher surface area – as one would expect. The diffusivity is seen to fall less steeply as the porosity decreases and in fact for porosity ϕ = 0.33, the diffusivity actually increases as the surface rate constant increases, most notable again for the higher surface-to-volume ratio.

This behaviour can be understood as a consequence of the greater number of gas molecules that can fit into the larger volume of the pore phase, increasing the probability of a particle hitting the surface – this will clearly have a lesser consequence where the surface area is smaller. As the porosity becomes very small, the molecules begin to obstruct each other such that their decomposition, whilst reducing the number of diffusing bodies, actually aids their movement through the confining environment and hence the diffusivity is increased in this extreme.

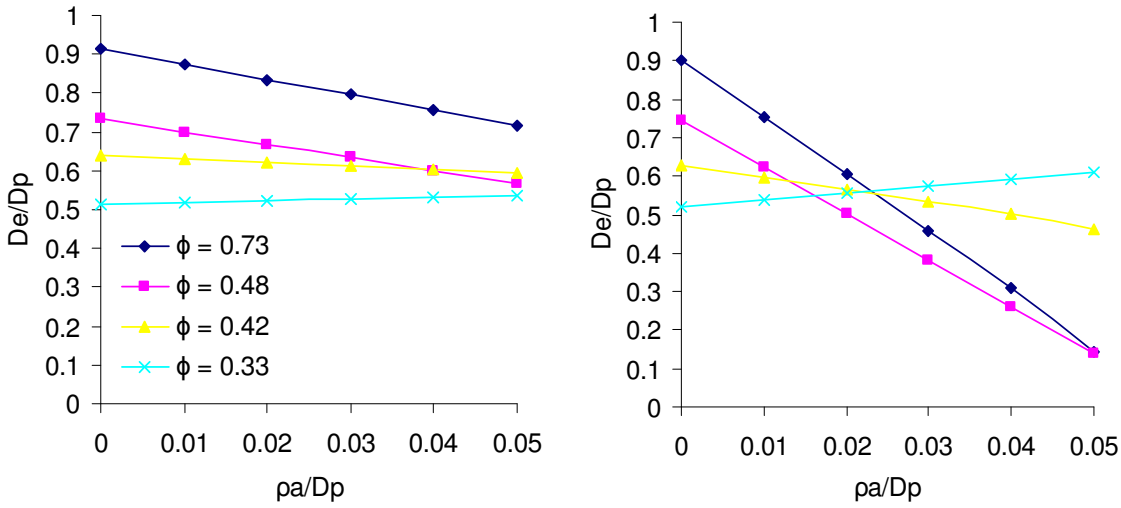

Figure 3.10: Calculated effective diffusivity for the two phase system relative to the pore phase diffusivity, D_e/D_p, as a function of $\frac{\rho a}{D_1}$ for systems of different porosity and $\frac{S_p}{V_p}$ values of (a) 2 and (b) 13.

The calculated dimensionless bulk effective rate constant ($K_e = \frac{k_e a^2}{D_e}$), as shown in figure 3.11, again also depends strongly on the surface-to-volume ratio and of course

the input rate, increasing with both for all porosities. For the lower $\frac{S_p}{V_p}$ case, the system with porosity $\phi = 0.48$ gives a much higher rate constant than the $\phi = 0.73$ case whereas for the higher $\frac{S_p}{V_p}$ case this difference is marginal. Otherwise the rate constant increases with porosity. This maximum in rate constant can be attributed to the slower diffusion associated with the low porosity system, increasing the probability that a molecule stays within the vicinity of the surface where it may then react. That this is not a dominating factor for the diffusivity is understood by considering the definition of the diffusivity, i.e. a measure of how quickly the gas molecules move as an average over all the molecules, compared to that of the rate constant which is effectively a measure of how quickly the molecules disappear. The number of molecules that hit the surface is a property connected with the system of molecules as a whole, whereas the relative time that molecules reside at the surface region does not depend on the total number of molecules, but is directly related to the subset of molecules that decay. Hence, the lower porosity/slow diffusion effect will be more apparent when considering the rate constant. This balance is further illustrated in figure 3.12 which gives the rate constant as a function of porosity for the two different surface-to-volume ratios considered for a constant surface rate. The effective rate constant reaches a maximum value at porosity dependent on the surface-to-volume ratio.

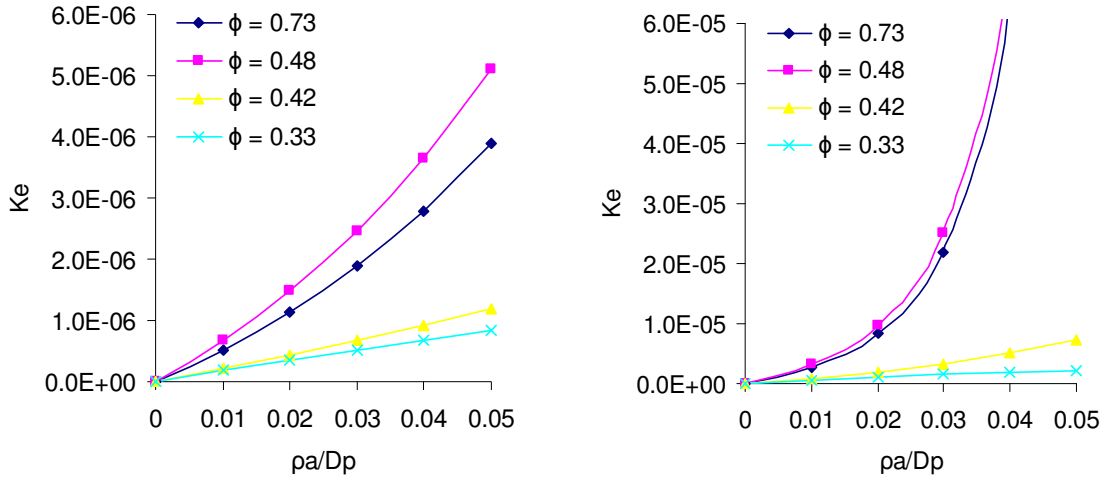

(a) (b)

Figure 3.11: Dimensionless effective rate constant, K_e, as a function of $\frac{\rho a}{D_1}$ for systems of different porosity and $\frac{S_p}{V_p}$ values of (a) 2 and (b) 13.

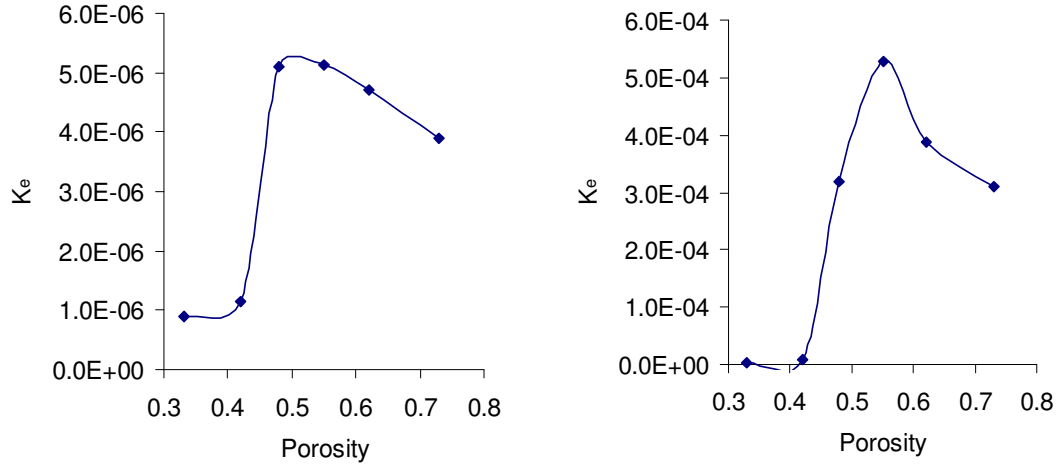

(a) (b)

Figure 3.12: Dimensionless effective rate constant, K_e, as a function of porosity for $\frac{\rho a}{D_1}$ = 0.05 and $\frac{S_p}{V_p}$ values of (a) 2 and (b) 13.

Essentially, in interpreting these results in terms of the real system and if the gas does not react, an ideal system would allow for fast diffusion through the pore network. In this case, the gas can penetrate the sensor layer effectively and quickly and a high porosity would be favourable to achieve this. Also it would be desirable to have a large a surface area as possible to promote the interaction which generates the response,

although there are of course additional issues to consider. Firstly we must address whether this is actually a realistic design: too high a porosity will be practically unachievable as this would require particles to be suspended within the pore fluid in an unstable formation (note also some level of sintering is unavoidable). Secondly we must consider connectivity: the particles must be connected so as to enable sufficient charge transfer through the layer. Furthermore if a reaction occurs, we also have to ask whether it is the product or the reactant that we are concerned with – or both. A high surface area will lead to a fast decomposition of the reactant such that if it is the reactant that is to be detected, some compromise needs to be made to accommodate the fact that the high surface area (needed for interaction) will result in low penetration of the gas through the layer. If the product is of interest then again a high surface area, high porosity system would appear advantageous. However, where certain connectivity has to be achieved for a current to actually be able to flow through the porous layer and resulting in a lower surface area, or due to other practical limitations, it may be the case that using a lower porosity gives a higher effective rate constant.

(3.6.2) Modelling the zeolite layer

The zeolite layer is represented by a system of two phases, the zeolite phase and the macropore phase, both of which are penetrable; the model system is illustrated in figure 3.8 (b). It is now aimed to demonstrate the dependency of the system's bulk diffusion and rate constants in terms of the following properties:

1. The ratio of diffusivities of the gas within the two bulk form phases, D_p/D_z. From the literature, as discussed in section 3.2, it is found that a gas may in cases diffuse more quickly within the zeolite phase than in the pore fluid (assumed here to be air) as confining structures may act to reduce directions of random motion hence assisting the transport of the gas through the structure [52]. Often, however, zeolite diffusion is observed to be slower than in air as the confinement acts to disrupt the flow of gas. Here we look quite generally at cases where the zeolite diffusivity is larger, smaller and equal to the pore diffusivity.

2. The partitioning of gas between the two layers, z ($z = n_{\mu z} / n_{\mu p}$). Where $z > 1$, the zeolite layer is favoured – this can be understood as due to the gas binding favourably onto the zeolite framework as expected, for example, for a polar molecule in a cation-

containing aluminosilcate framework. Conversely the gas-zeolite interactions may be unfavourable such that $z < 1$.

3. The system porosity, ϕ, i.e. the pore fraction (where the zeolite fraction is 1- ϕ).

4. The rate constant of the zeolite layer which is given in dimensionless form as $K_z = k_z a^2 / D_z$.

Figure 3.13 gives the calculated effective diffusivity as a function of the porosity, the gas can of course now move through the entirety of the system, it is released in the pore phase and here has the same diffusivity in both phases. Two cases are shown of where the gas favours being in the zeolite phase (the central, spherical phase), as is defined by the value of partition coefficient ($z = 10$ or $z = 20$). This is compared to an example of the zeolite phase being less favourable than the macroporous region ($z = 0.3$) and also the system of impenetrable obstacles, as was given in figure 3.9 above.

A point of interest here (figure 3.13) is that the relationship between porosity and diffusivity is not monotonic where $z > 1$. A minimum in diffusivity occurs at porosity $\phi \approx 0.75$ for $z = 20$ and $\phi \approx 0.65$ for $z = 10$. This result relates to the idea of a percolation threshold as discussed in chapter 1. At first, as the volume of the favoured zeolite phase is decreased, the diffusivity of the system is decreased as one would expect based on previous discussions. However, the diffusivity reaches a minimum as the amount of zeolite phase is reduced to the extent that as molecules favourably enter this phase, this reduces transport through the system as a whole, as the regions are now poorly connected. Hence, decreasing the volume of zeolite thereafter actually increases the diffusivity – this point occurring at a higher porosity as partitioning favours the zeolite. The minimum also becomes shallower as z decreases tending to a line of constant D_e/D_p (=1) at $z = 1$, where both phases are favoured equally.

On the other hand, where the pore phase is favoured, the relationship between diffusivity and porosity is monotonic. In the case of impenetrable spheres, this is (as has already been discussed) as expected. One might expect therefore, that for $z = 0.3$ that there would also be a minimum point such that the $z > 1$ and $z < 1$ cases give mirror images of each other, and this is in fact as predicted using EMT. However this is not the case here and this can be attributed to the fact that EMT does not take into account which phase the gas is released into – here the macropore phase. This is why the eigenstate model gives a minimum point with $z > 1$ and not with $z < 1$, since in the

former case, the gas must pass through the less favoured phase and in the latter case it can avoid it.

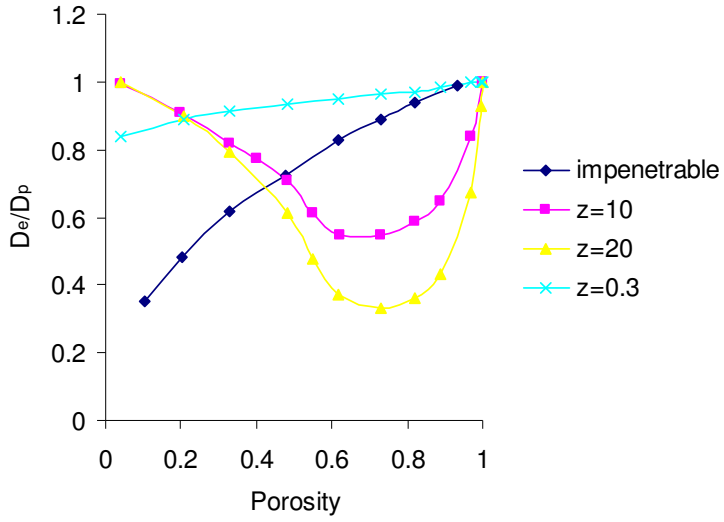

Figure 3.13: Calculated effective diffusivity for the two phase system relative to the pore phase diffusivity, D_e/D_p, as a function for porosity for a system with different partition coefficients ($z = n_{\mu z} / n_{\mu p}$). The ratio of diffusivities in the two phases is equal to unity.

It is of course likely that the diffusivities of the gas within the zeolite and within the pore phase are not equal; in this case the bulk effective diffusivity will depend on the ratio of diffusivities of the two phases as well as the partition coefficient and the porosity. This is demonstrated in figure 3.14 which gives D_e/D_p as a function of the ratio D_p/D_z. In terms of the partition coefficient, a simple surmise would be that if the gas diffuses more quickly in the pore phase, then D_e will increase as the pore phase becomes more favourable and vice versa if the gas diffuses more quickly in the zeolite. This is exactly as shown in the extremes of figure 3.14(a), which gives a system where the zeolite phase consists of spheres which are just touching (ϕ=0.48).

A higher porosity system is shown in figure 3.14(b) and in this case we again see the need for a sufficient fraction of zeolite phase for the expected behaviour to be observed. Where $D_z>D_p$, z=10 (as the highest z value considered) actually gives the lowest effective diffusivity as the gas is favourably absorbed into the small volume of the zeolite phase where it does not transport effectively through the system as a whole.

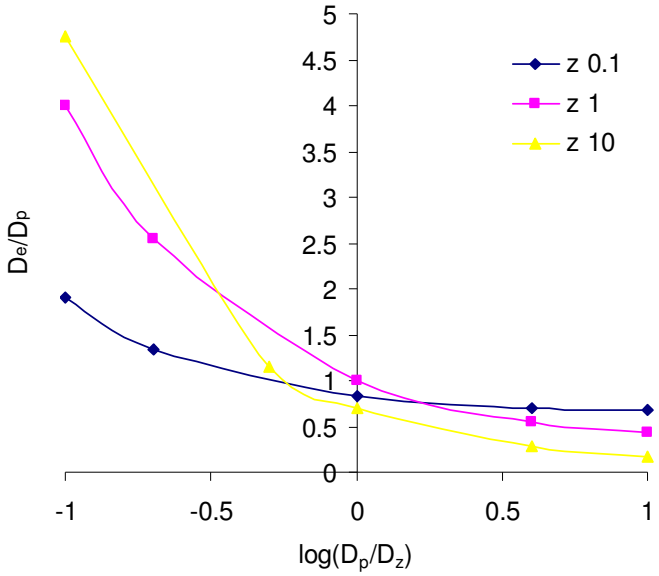

(a)

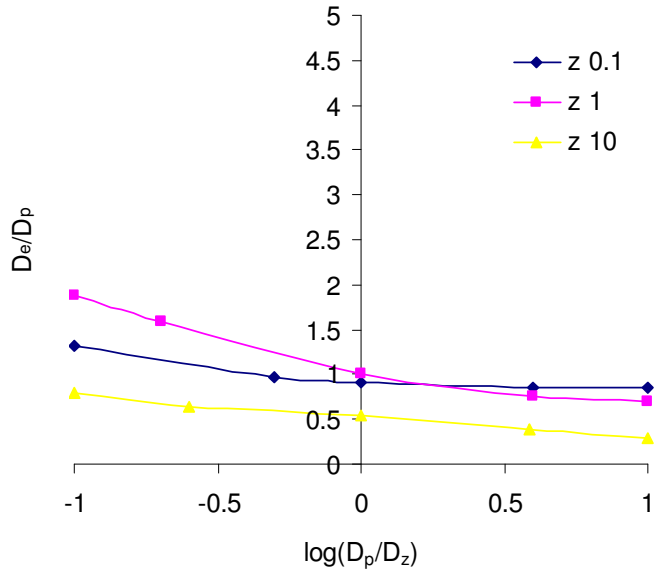

(b)

Figure 3.14: Calculated effective diffusivity for the two phase system relative to the pore phase diffusivity, D_e/D_p, as a function of the ratio of diffusivities of the two phases D_p/D_z for different partitioning ($z = n_{\mu z} / n_{\mu p}$) and for porosity (a) 0.48 and (b) 0.73. Series are z=0.1, blue; z=1, pink; z=10, yellow.

Where a reaction occurs within the zeolite, the diffusivity is reduced, as was discussed in section 3.6.1 and is now shown in figures 3.15-3.17. In all cases the diffusivity falls most steeply for large z, i.e. where adsorption into the zeolite phase, in which the reaction takes place, is favoured. Figure 3.15 gives the calculated effective diffusivity for cases of the diffusion in the zeolite being greater or less than that in the pore, for a

system where the zeolite consists of just touching spheres (ϕ=0.48). Where $D_p/D_z < 1$, if no reaction occurs and the gas is favourably absorbed into the zeolite phase, the bulk effective diffusivity increases with partition coefficient as has been discussed. However, as the rate constant increases, there is a counteracting reduction in diffusivity which is most effective for high z systems where the gas favours being in the zeolite phase. Hence the diffusion observed for high z becomes slower than for a system where the zeolite is not favoured.

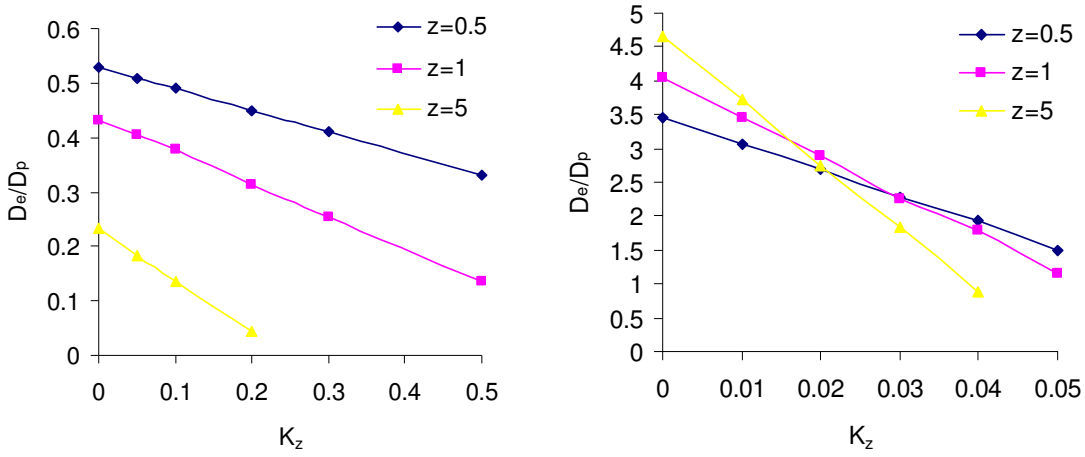

(a) (b)

Figure 3.15: Calculated effective diffusivity for the two phase system relative to the pore phase diffusivity, D_e/D_p, for a system of porosity = 0.48 (just touching spheres) for different partition coefficients ($z = n_{\mu z} / n_{\mu p}$) and ratio of diffusivities (a) D_p/D_z = 10 and (b) D_p/D_z = 0.1.

In figure 3.16 the porosity is increased to 0.73. Compared with the previous system, the decrease in diffusivity with rate constant is to a lesser extent (i.e. the gradient is less steep), as obviously now there is a smaller amount of the catalytic zeolite phase. For $D_p/D_z < 1$, the z = 5 system falls quickly to zero, reaching zero at a lower input rate constant than for the ϕ = 0.48 system due to the fact that the initial diffusivity is lower (the gradient of diffusivity decrease in the lower porosity is greatest). This is reflected in the calculated effective reaction rate constant ($K_e = \frac{k_e a^2}{D_e}$), as given in figure 3.17(b).

Whilst for z = 0.5, the effective rate is lower for the higher porosity, the reverse is true for higher z values, the rate constant for the z=5 system being significantly higher for the higher porosity. This is a consequence of diffusion-reaction balance: the slower overall diffusion within the system means that although there is less of the catalytic

phase, the gas moves more slowly through it, or more slowly away from it, so the effect of the reaction will be greater. For the $D_p/D_z > 1$ case, the lower porosity (higher proportion of zeolite) system always has the higher rate constant for a fixed partitioning – as perhaps is more naturally expected. In this case the effective diffusivity and the zeolite volume, increase together.

Whereas the effective diffusivity might increase or decrease with partition coefficient at a given input rate constant, depending on the geometry, the bulk effective rate constant always increases with partition coefficient for a fixed porosity – as the reaction only occurs within the zeolite.

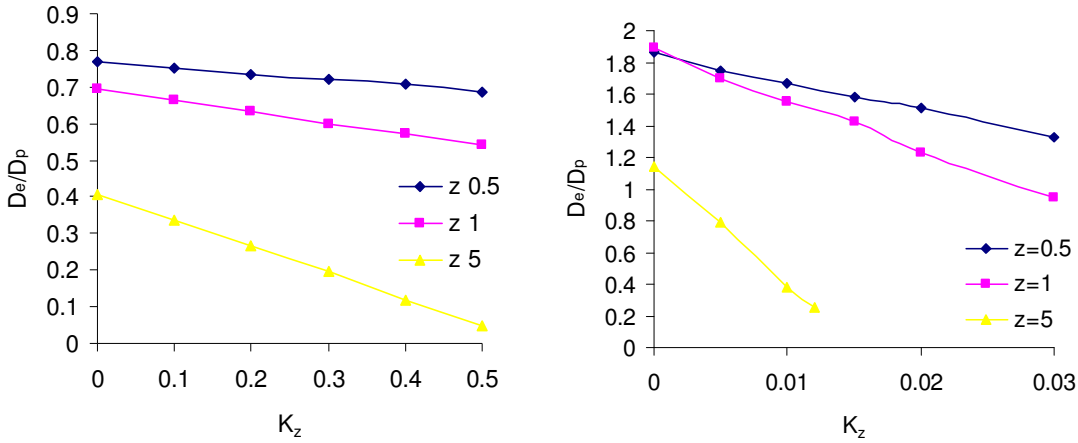

(a) (b)

Figure 3.16: Calculated effective diffusivity for the two phase system relative to the pore phase diffusivity, D_e/D_p, for a system of porosity = 0.73 for different partition coefficients ($z = n_{\mu z} / n_{\mu p}$) and ratio of diffusivities (a) D_p/D_z = 10 and (b) D_p/D_z = 0.1.

If the porosity is decreased to 0.21, as in figure 3.17, the effect of changing the partitioning, when compared to the effect of the reaction, is much reduced due to the small pore fraction. In fact the calculation fails for z = 0.5, $D_p/D_z > 1$, producing a negative effective diffusion coefficient, indicating that transport will not occur through this system. Note in all cases the diffusivity decreases more quickly where diffusion is slowest in the zeolite and the gas will reside longer in the reactive phase. This difference becomes reduced as the porosity is reduced.

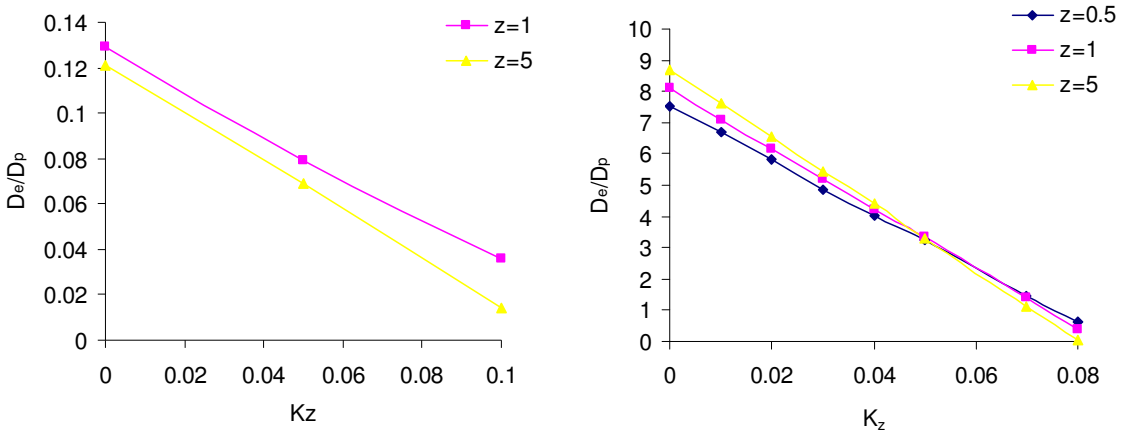

(a) (b)

Figure 3.17: Calculated effective diffusivity for the two phase system relative to the pore phase diffusivity, D_e/D_p, for a system of porosity = 0.20, where a reaction occurs within the zeolite, for different partition coefficients ($z = n_{\mu z} / n_{\mu p}$) and ratio of diffusivities (a) D_p/D_z = 10 and (b) D_p/D_z = 0.1.

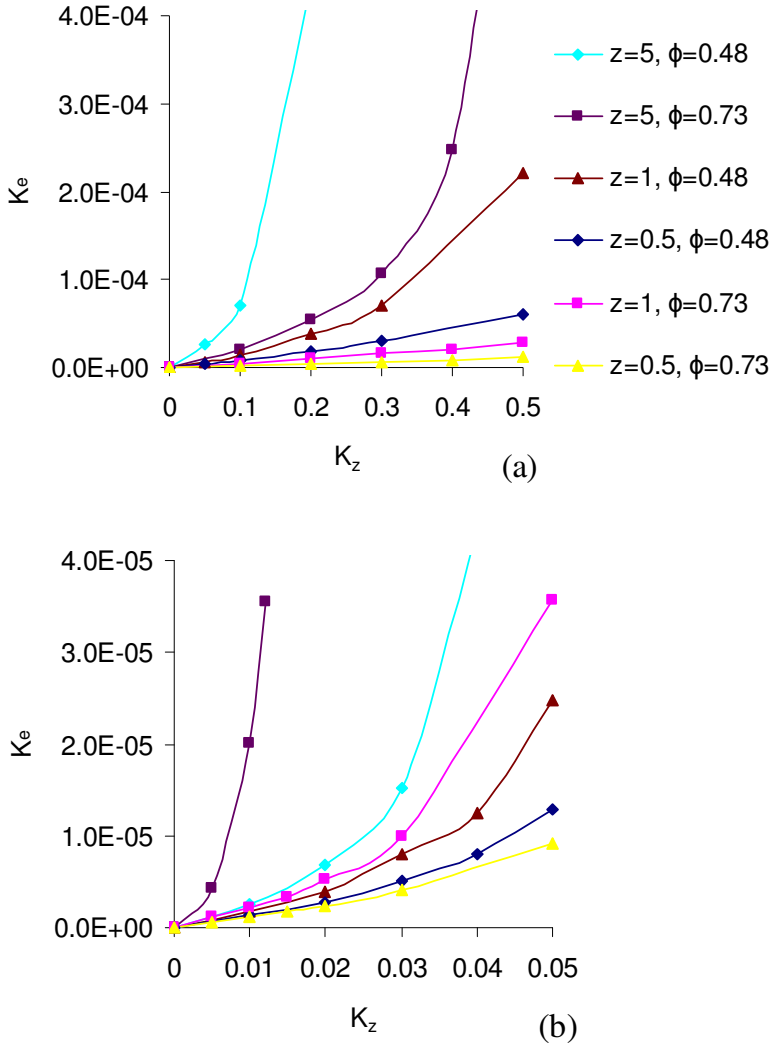

Figure 3.18: Dimensionless effective rate constant, K_e, for systems of porosity ϕ = 0.48 (just touching spheres) and ϕ = 0.73 for different partition coefficients ($z = n_{\mu z} / n_{\mu p}$) and ratio of diffusivities within the two phases (a) D_p/D_z = 10 and (b) D_p/D_z = 0.1.

As has been noted, depending on the ratio of diffusivities, the effective rate constant for a fixed partitioning may increase or decrease with porosity. Figure 3.19 further illustrates this point giving the calculated effective rate as a function of porosity. For $D_p > D_z$, figure 3.19(a), the rate constant increases monotonically as the porosity is reduced from 1 where no zeolite is present and hence the effective rate constant is zero. As has already been stated, a low z system (where $D_p > D_z$) of low (macro) porosity (essentially where the zeolite spheres are overlapping) does not maintain sufficient transport. For higher partitioning, the rate increases with porosity and the behaviour becomes almost asymptotic at about $\phi \approx 0.3$ for $z = 5$ and $\phi \approx 0.2$ for $z = 1$. Beyond

these points the gas will decompose to its products before diffusing a significant distance.

Where the gas diffuses more quickly in the zeolite phase, the rate also initially increases with decreasing porosity, however, it then reaches a maximum and thereafter decreases as observed in figure 3.19(b). The maximum becomes a more pronounced peak as the partition coefficient increases, occurring at the point where there is an optimum balance between the amount of the catalytic phase being large enough to support a significant reaction but small enough to cause the transport through the system as a whole to be slow so that it resides longer in the zeolite volume such that the reactant will decompose effectively to its products. After this point, the rate decreases despite the increase in zeolite volume due to the ability of the gas to transport through the system efficiently. However, decreasing the porosity approximately past the point where the zeolite spheres are just touching does not cause a great variation in the bulk rate constant that will be observed. Clearly if gases are distinct only in terms of the partition coefficient and behave as in figure 3.19(b), using a mid-range porosity will allow us to distinguish between them. For 3.19(c) the diffusivity in the zeolite and pore phases are equal giving behaviour intermediate between the two extreme cases.

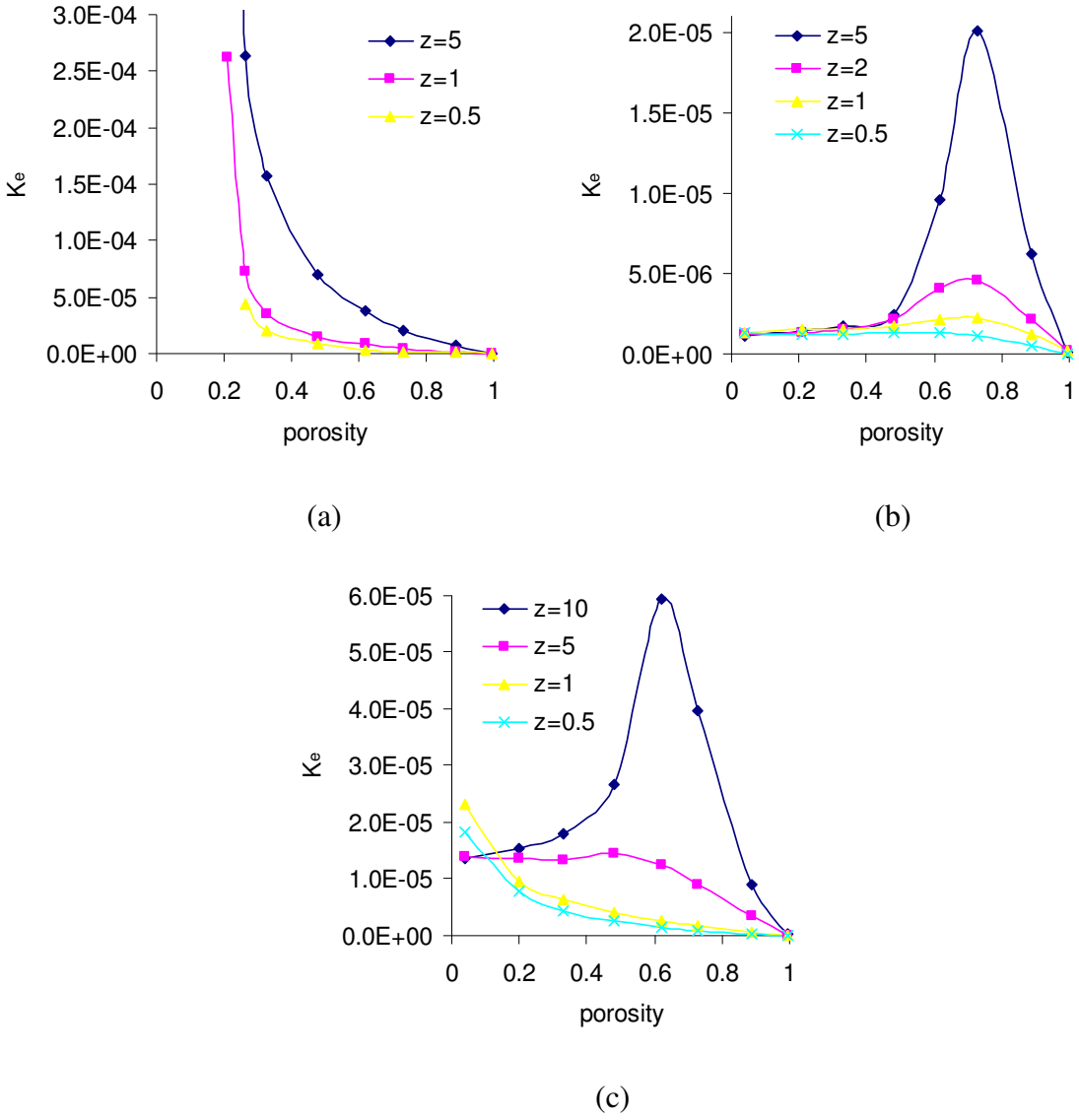

Figure 3.19: Dimensionless effective rate constant, K_e, for as a function of porosity for different partition coefficients ($z = n_{\mu z} / n_{\mu p}$) and ratio of diffusivities within the two phases (a) D_p/D_z = 10, input rate 0.1, (b) D_p/D_z = 0.1, input rate 0.01 and (c) D_p/D_z = 1, input rate 0.05.

In order to aid an understanding of the results presented above in terms of the actual macroporous zeolite transformation layer and its selective properties as applicable to gas sensing, we consider a hypothetical collection of gases, as illustrated in figure 3.20. The gases, labelled A-D, have the same pore diffusivity (D_p) and the same sensitivity with respect to the sensor layer. Each has different diffusive (D_z), reactive (K_z) and adsorbent (z) properties with respect to a hypothetical zeolite. It is assumed for simplicity that any reaction products have zero sensor sensitivity. It is now

demonstrated how the layer can be optimally manufactured to enable feasible discrimination between the different gas pairs.

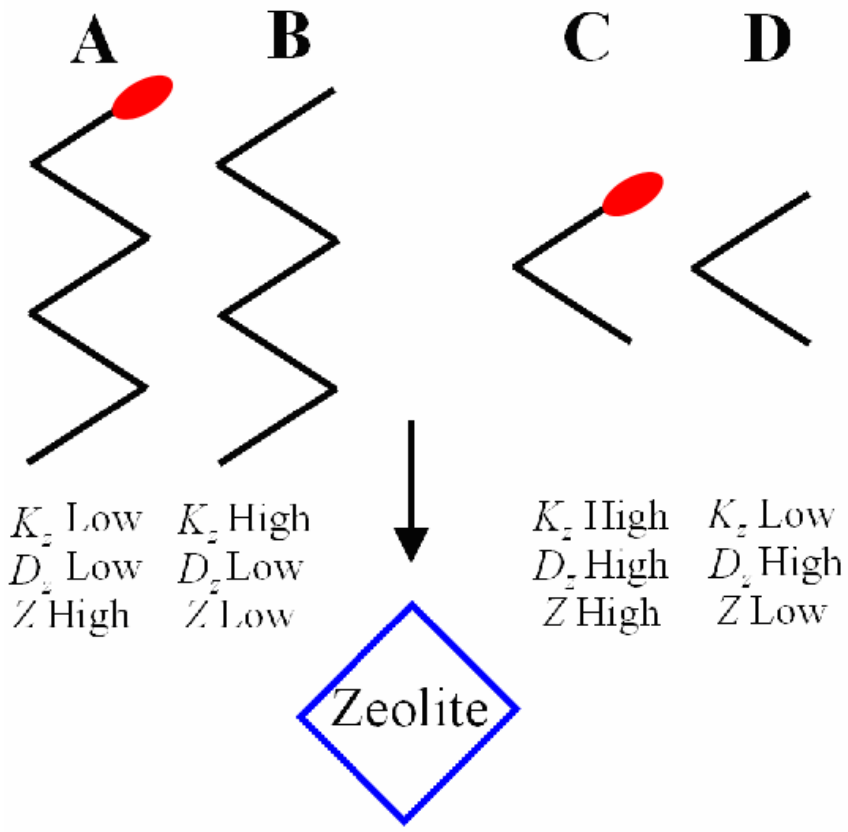

Figure 3.20: Hypothetical gas-zeolite system. 4 theoretical gases are defined by whether they react in the zeolite (K_z), how quickly they move in the zeolite (D_z) and how strongly they adsorb within the zeolite ($z = n_{\mu z} / n_{\mu p}$).

A & B: Both gases diffuse slowly within the zeolite, gas A adsorbing favourably compared to gas B which reacts within the zeolite phase. Based on these properties it is proposed, considering figure 3.17(a), that a very low porosity will prevent transport of gas B through the zeolite layer, providing that the z value is sufficiently low, such that a response will only be observed with gas A. If z is not so low that this occurs, then a low porosity would still be preferable as this will result in a very large effective rate constant (figure 3.19(a)) such that again the response to gas B will be very low as the product gas has zero sensitivity.

A & C: Gas C, like A, binds favourably within the zeolite but diffuses quickly in this phase and also reacts. Here it is likely that the two gases have similar diffusivities as

whilst A will diffuse more slowly due to its low D_z value, the reaction of gas C means that its observed diffusivity will be reduced and hence similar to that of A. Here, considering figure 3.19(b), ideally the layer design would be of the optimum porosity such that the effective rate constant of gas C becomes very large – as a result the steady state response to gas C will be low compared to A.

A & D: Gas D does not bind favourably in the zeolite such as gas A but does diffuse more quickly within it, neither gas reacts. Here distinction is only possible in terms of differences in the diffusional behaviour. For this case again, a low porosity system would be advantageous as this will cause gas A, despite its high z value, to diffuse much more slowly than gas D and hence the response time will be longer for gas A.

B & C: In comparing the two reacting gases, which are contrasting in terms of their partition functions and diffusivities, one could again aim for a low porosity. In this case gas B, which has low z / low D_z, will not pass through the layer easily. Alternatively the optimum (higher) porosity could be used where gas C, which has high z / high D_z, will react with a greater effective rate. This would be the better option if gas C decomposes very quickly to an insensitive product as the former option would just result in two zero responses whereas the latter, gas C would give a response as the effective rate will be very small (figure 3.19(a)).

B & D: In this case neither gas binds favourably within the zeolite whilst gas B moves more slowly through the zeolite and also reacts within it. In this case a very low porosity could be used to prevent gas B passing through to the sensor layer either by it decomposing quickly or not transporting through sufficiently in the first place. If B did not react and could pass through the low porosity system the gases would still be distinct in terms of their response times with B response time << D response time.

C & D: Here both gases move quickly through the zeolite phase with gas C being both higher z and reacting – here again one can optimise the porosity to give a large effective rate constant of gas C and hence a lower steady state response.

Hence, it has been demonstrated that the microstructure of the zeolite layer could be manipulated to achieve discrimination between different gases. It is clear from the

discussion, that the suitability of a particular microstructure design is crucially dependent on the relative sensitivities of the reactant and product gases. For example, for gases B and C it was discussed how using a low porosity may result in both gases giving a zero response due to the effectual decomposition of C – but this will not be the case if the product is more sensitive than the reactant. As well as the sensitivities of the gases with respect to the sensor, one also must consider the diffusion and reaction properties of the gas in the sensor which may directly alter the transport (and reaction) behaviour within the zeolite – or instead, the interpretation of what happens in the zeolite might be altered.

(3.7) Conclusion

Through the course of this chapter, the importance of the microstructure of the components of our composite sensor system (metal oxide and zeolite) has been demonstrated. Diffusion through a porous layer depends on the scale of confinement, how tortuous the system is, the porosity and finer details of the structure geometry, as well as the composition of the confining solid. Where a reaction occurs, the picture is complicated further as the rate at which a reactant decomposes also depends on these factors and the diffusivity and the rate constant are interlinked such that there will be a balance between the diffusion and reaction of gas within the system. The occurrence of a reaction will generally cause the diffusion of the reactant to be reduced, except where the system is highly tortuous and largely inaccessible to the gas, in which case a reaction at the solid-pore interface may actually aid transport by increasing the mean free path of the diffusing molecules.

Here, two distinct systems have been considered. Firstly, a system of impenetrable solid particles is used to represent the porous metal-oxide layer where a reaction may occur at the interface between the pore and an impenetrable solid phase. In this case, the diffusivity decreases as the pore volume decreases and increasing the relative surface to pore fraction (by using smaller particles) will, as expected, enhance the effective rate constant. In considering the rate constant, it is also noted that there is a subtle balance between the number of particles that can fit in the system pores (increasing with pore fraction) and the speed of diffusion away from the reactive surface region (decreasing

with increasing pore fraction) and this must be considered in the engineering of the sensor layer such that the design is optimal.

The second case considered is that of a macroporous-zeolite phase, modelled as a medium consisting of two penetrable phases such that one must now account for the diffusivities and the relative preference of the gas for the two phases. Where no reaction occurs in the zeolite phase, it is shown how differences in gas adsorption or diffusion within the zeolite particulates, can be magnified, by fine tuning the system microstructure such that there is a significant difference between the effective diffusivities of different gases through the layer. If a reaction does occur, again the microstructure can be controlled to maximise differences in the effective properties. As with the model sensor system, optimising the balance between diffusion and reaction throughout the system will be essential to achieving discrimination. For example, it is observed how the effective rate constant increases dramatically at a given porosity. Where diffusion in the zeolite phase is slow, this occurs at low porosity as the slow movement through the dominant phase means the gas quickly decomposes. Where the diffusion in the zeolite is fast, there is a balance between the slow diffusion associated with high (macro) porosity and the obvious need for an ample amount of the reactive phase such that the porosity associated with maximum rate constant is increased.

As was discussed in chapter 2, it is clear here, that the consequences of the behaviour discussed depend on how the sensor material actually interprets the presence of different gases. An issue of paramount importance is that of the relative sensitivities of different gases. Additionally we need to consider how the gas behaviour actually manifests itself as the response, i.e. will it affect the steady state response or the response time. Finally, it must also be considered how the diffusion and reaction properties of one layer affect those of the other when the separate components are combined as a composite device. These crucial issues are the topic of the next chapter.

References

[1] D.E. Williams, in: P.T. Moseley, B.C. Tolfield (Eds.) “Solid state gas sensors” Adam Hilger, Bristol (1987) chpt 5.

[2] R. Landauer, J. App. Phys., 23 (1952) 779. “The Electrical Resistance of Binary Metallic mixtures.”

[3] H.T. Davis, J. Am. Ceram. Soc. 60 (1997) 499-501. “The effective medium theory of diffusion in composite media,”

[4] V. N. Burganos, S. V. Sotirchos, AlChE J. 33 (1987) 1678-1689. “Diffusion in Pore Networks: Effective Medium Theory and Smooth Field Approximation.”

[5] M. Tather, A. Erdem-Senatalar, Chem. Eng. J. 102 (2004) 209-216. “Estimation of the effective diffusion coefficients in open zeolite coatings.”

[6] L. Zhang, N.A. Seaton, AlChE J. 38 (1992) 1816-1823. “Prediction of the Effective Diffusivity in Pore Networks Close to a Percolation Threshold.”

[7] H. Mehrer, “Diffusion in solids: fundamentals, methods, materials, diffusion-controlled processes” Vol. 155 Springer series in solid-state sciences (2007) chpt 4.

[8] D.J. Bergman, K-J Dunn, 51 (1995) 3393-3401. “Self-diffusion in a periodic porous medium: A comparison of different approaches.”

[9] J. W. Evans, M. H. Abbasi, A. Sarin, J. Chem. Phys. 72 (1980) 2967-2973. “A Monte Carlo simulation of the diffusion of gases in porous solids.”

[10] R. Valiullin, V. Skirda, 114 (2001) 452-458. “Time dependent self-diffusion coefficient of molecules in porous media.”

[11] J-L. Auriault, J. Lewandowska, Transp. Porous Media, 21 (1995) 47-70. “Non-Gaussian Diffusion Modeling in Composite Porous Media by Homogenization: Tail Effect.”

[12] J. Qian, P.N. Sen, J. Chem. Phys., 125 (2006) 194508 “Time dependent diffusion in a disordered medium with partially absorbing walls: A perturbative approach.”

[13] D.J. Bergman, K-J. Dunn, J. Chem. Phys., 102 (1995) 3041. “Self-diffusion of nuclear spins in a porous medium with a periodic microstructure.”

[14] D.J. Bergman, K. Dunn, Phys. Rev. E, 51 (1995) 3393-3401 “Self-diffusion in a periodic porous medium: A comparison of different approaches.”

[15] D.J. Bergman, K-J. Dunn, Phys. Rev. B, 50 (1994) 9153. “Theory of diffusion in a porous medium with applications to pulse-field-gradient NMR.”

[16] D. J. Bergman, K-J. Dunn, Phys. Rev. E, 51 (1995) 3401. “Self-diffusion in a periodic porous medium with interface absorption.”

[17] U. Hizi, D.J. Bergman, J. App. Phys., 87 (2000) 1704. “Molecular diffusion in periodic porous media.”

[18] J. Karger, D. Ruthven, “Diffusion in Zeolites and other Microporous Solids” Wiley, New York (1992).

[19] D. Frenkel, B. Smith, “Understanding molecular simulation: from algorithms to applications.” Elsevier, USA (1996)

[20] B. Smit, T.L.M Maesen, Chem. Rev., 108 (2008) 4123. “Molecular Simulations of Zeolites: Adsorption, Diffusion, and Shape Selectivity.”

[21] D. Dubbeldam, R.Q. Snurr, Molecular Simulation, 33 (2007) 305-323. “Recent developments in the molecular modeling of diffusion in nanoporous.”

[22] A.I. Skoulidas, D.S. Sholl, J. Phys. Chem. A 107 (2003) 10132-10141. "Molecular Dynamics Simulations of Self-Diffusivities, Corrected Diffusivities, and Transport Diffusivities of Light Gases in Four Silica Zeolites To Assess Influences of Pore Shape and Connectivity."

[23] G. Tsikoyiannis, J. Wei, J. Chem. Eng. Sci., 46 (1991) 233-253. "Diffusion and reaction in high zeolite catalysts - I. A stochastic theory."

[24] S.M. Auerbach, F. Jousse, D.P. Vercauteren, in C. R. A. Catlow, R. A. van Santen and B. Smit (Eds.) "Computer Modelling of Microporous and Mesoporous Materials" Academic Press (2004) chpt 3.

[25] E. Beerdsen, D. Dubbeldam, B. Smit, Phys. Rev. Lett 96 (2006) 044501-044504. "Understanding diffusion in nanoporous materials"

[26] D. Dubbeldam, E. Beerdsen, S. Calero, B. Smit, J. Phys. Chem. B, 110 (2006) 3164–3172 "Dynamically Corrected Transition State Theory Calculations of Self-Diffusion in Anisotropic Nanoporous Materials."

[27] E.G. Derouane, J. Andre, Chem. Phys. Lett., 137 (1987) 336-340. "A simple van der Waals model for molecule-curved surface interaction in molecular-size microporous solids."

[28] E.G. Derouane, Journal of Molecular Catalysis 134 (1998) 336-340. "Zeolites as solid solvents."

[29] G. Sastre, A. Corma, Top. Catal., 24 (2003) 7-12. "Ordinary diffusion and single file diffusion in zeolites with monodimensional channels. Benzene and n-butane in ITQ-4 and L zeolites."

[30] R. Gorring, J. Catal. 31 (1973) 13-26. "Diffusion of normal paraffins in zeolite T: Occurrence of window effect."

[31] P.B. Weisz, Pure & Appl. Chem., 52 (1980) 2091-2103. "Molecular shape selective catalysis."

[32] V. Iyengar, M. Coppens, Chem. Eng. Sci., 59 (2004) 4747–4753. "Dynamic Monte-Carlo simulations of binary self-diffusion in zeolites: effect of strong adsorption sites."

[33] D.L. Wernick, E.J. Osterhuber, J. Membrane Science, 22 (1985) 137-146. Permeation through a single crystal of Zeolite NaX."

[34] R.M. Barrer Proc. Roy. Soc. London A167 (1938) 392-420. "The sorption of polar and non-polar gases by zeolites."

[35] PN Sarma, HW Haynes, Adv. Chem. Ser., 16 (1974) 205–217. "Application of Gas Chromatography to Measurements of Diffusion in Zeolites."

[36] H Pfeifer, W Schimer, H Winkler, Adv. Chem. Ser., 38 (1973) 430–440 "Nuclear Magnetic Resonance Studies of Molecules Adsorbed on Zeolites A, X, and Y."

[37] E. Cohen de Lara, R. Kahn, F. Mezei, J. Chem. Soc. Faraday Trans. 1, 79 (1983) 1911-1920. "Determination of the intracrystalline diffusion coefficient of methane in A zeolites by means of neutron spin-echo experiments."

[38] R.M. Barrer, Trans. Faraday Soc. 37 (1941) 590-599. "Migration in crystal lattices."

[39] S. Ryu, Magnetic Resonance Imaging, 19 (2001) 411-413. "Probing pores using elementary quantum mechanics."

[40] C. Kittle, "Introduction to solid state physics" Wiley (1986) pp 169.

[41] P.P. Mitra, P. N. Sen, L.M. Schwartz, Phys. Rev. B, 47 (1993) 8565-8573. "Short-time behaviour of the diffusion coefficient as a geometrical probe of porous media."

[42] Y.M. Strelniker, D.J Bergmann, Phys. Rev. B, 50 (1994) 14001-14015. “Theory of magnetotransport in a composite medium with periodic microstructure for arbitrary magnetic fields.”

[43] W.H. Press, S.A. Teukolsky, W.T. Vetterling, B.P. Flannery, “Numerical recipes in C: the art of scientific computing”, Cambridge University Press (2002), chpt 2.3.

[44] W.H. Press, S.A. Teukolsky, W.T. Vetterling, B.P. Flannery, “Numerical recipes in C: the art of scientific computing”, Cambridge University Press (2002), chpt 2.9.

[45] W.H. Press, S.A. Teukolsky, W.T. Vetterling, B.P. Flannery, “Numerical recipes in C: the art of scientific computing”, Cambridge University Press (2002), chpt 11.2.

[46] W.H. Press, S.A. Teukolsky, W.T. Vetterling, B.P. Flannery, “Numerical recipes in C: the art of scientific computing”, Cambridge University Press (2002), chpt 11.3.

[47] D.J. Bergman, Phys. Rev. E, 55 (1997), 4233. “Diffusion eigenstates of a porous medium with interface absorption.”

[48] W.H. Press, S.A. Teukolsky, W.T. Vetterling, B.P. Flannery, “Numerical recipes in C: the art of scientific computing”, Cambridge University Press (2002), chpt 4.2.

[49] W.H. Press, S.A. Teukolsky, W.T. Vetterling, B.P. Flannery, “Numerical recipes in C: the art of scientific computing”, Cambridge University Press (2002), chpt 6.5.

[50] D.W. Lewis, D.J. Willock, C.R.A. Catlow, J.M. Thomas, G.J. Hutchings, Nature, 382 (1996) 604-606. “De novo design of structure-directing agents for the synthesis of microporous solids.”

[51] D. Gay, A.L. Rohl, J. Chem. Soc., Faraday Trans., 91 (1995) 925-936. “MARVIN: a new computer code for studying surfaces and interfaces and its application to calculating the crystal morphologies of corundum and zircon.”

[52] S. Yashonath, P. Santikary, J. Phys. Chem., 97 (1993) 13778-13787. “Sorbate properties and cage-to-cage diffusion of argon in NaCaA: A molecular dynamics study.”

Chapter 4: Macroscopic modelling

(4.1) Introduction

We have now considered how the properties of the microstructure may influence the transport of gas, both through an ideal porous layer of one impenetrable phase, at the surface of which a reaction may occur (representing the sensor) and through a system consisting of two penetrable phases, in which bulk, phase-dependent reactions may occur (representing the zeolite overlayer). Such changes now need to be interpreted in terms of the sensor response.

Simultaneous diffusion and reaction of a gas through the porous sensor layer results in the formation of a spatially and temporally dependent concentration gradient over the thickness of the layer. A zeolite transformation layer can be used to transform the gas profile incident upon the sensing layer in a manner that depends on the diffusion-reaction competition throughout the zeolite porous layer. The zeolite layer will ultimately obstruct the gas such that an increase in response time is expected – to an extent dependent on the particular gas-zeolite combination, as was discussed in chapters 2 and 3. The zeolite may also catalyse a reaction, such that a more or less sensitive, a more or less reactive, or faster or slower diffusing gas hits the sensor layer.

Here we turn to a simple macroscopic model for gas transport through a two phase system consisting of adjacent, homogeneous sensing and transforming layers characterised by effective diffusion and rate coefficients, as discussed in previous chapters. The response of the sensor layer has then been calculated as a function of these effective parameters by modelling the electric field established within the layer when a voltage is applied via two electrodes and how this varies (due to the variation of surface charge density) on the introduction of the test gas.

It is also noted that the potential to discriminate between different gases can be enhanced, exploiting the variable concentration, by making suitable macroscopic design choices such as layer thickness and electrode positioning. Here results are presented to probe the dependency of response on these additional variables and how this may be interpreted to discriminate between different gases as defined by their diffusion-reaction properties and their sensitivities.

(4.2) Theory

(4.2.1) Model Overview

As illustrated in figure 4.1(a), the analyte gas stream, considered in one-dimension, is modelled to diffuse through two macroscopically homogenous layers. The gas concentration, C_0, incident at $x = h_s + h_z$ is assumed to be constant during the injection time or "on-pulse" and to fall instantaneously to zero during the subsequent "off-pulse".

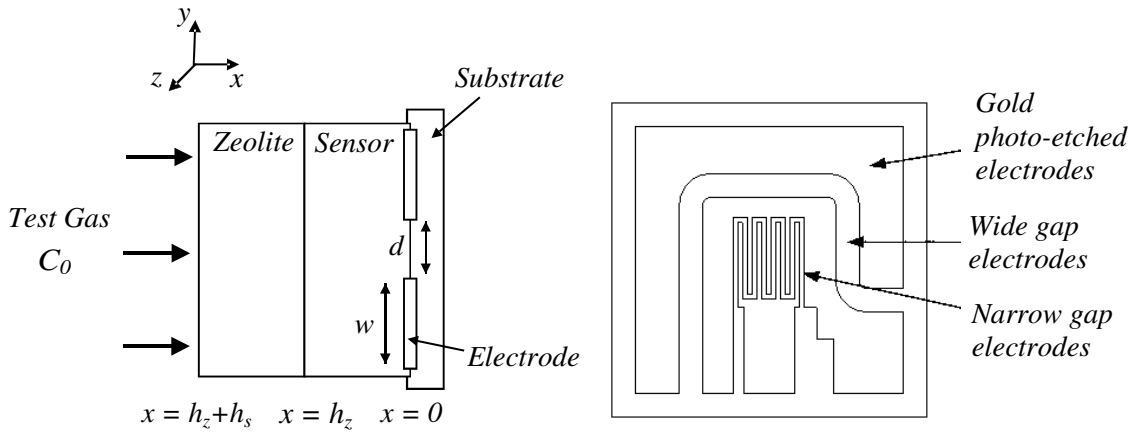

Figure 4.1: (a) Model composite gas sensor system setup. (b) Typical interdigitated electrode structure used for a multi-electrode device.

Two coplanar electrodes are positioned at the base of the sensing layer with separation d and width w, they are assumed thin compared to the thickness of the layer, h_s, and long in the z-direction. A constant voltage, V, is applied across the electrodes and a current is therefore established through the sensing layer. There is assumed to be zero electric field density within the zeolite layer.

In figure 4.1(b) an example of an actual practical electrode design is illustrated (which would then be placed at the based of the sensing layer).

(4.2.2) Calculating the response I

The response can be calculated by firstly calculating the current that flows between the two electrodes. Following Ohm's law, the conductance, G, is proportional to the current, i, where a fixed voltage, V, is applied such that the change in conductance is given by: $\Delta G(t) = \frac{\Delta i(t)}{V}$.

The current density is proportional to the electric field, E, such that $J = \sigma E$ where σ is the conductivity. Integrating the current density over the area of the plane bisecting the electrodes gives the current flowing between them:

$$i(t) = \int J \cdot ds = b\int_0^{h_s} J dx$$

The second equality requires that the electrodes are long in the z-direction with length b >> w (see figure 4.1(a)).

The electrical conductivity of the semiconductor is given by $\sigma = e(n\mu_e + p\mu_h)$ where μ_e and μ_h are the electron and hole mobilities respectively, e is the elementary charge and n and p are the electron and hole concentrations respectively. This is simplified by the assumption that conductivity depends only on electrons for an n-type semiconductor or holes for a p-type semiconductor. Hence, for the example of an n-type semiconductor, the current is given by:

$$i(t) = \mu_e eb\int_0^{h_s} nEdx \qquad \text{Equation 4.1}$$

On the introduction of a reducing gas, the conductivity of the n-type sensor will increase and, assuming a simple linear relation between carrier concentration and the incoming gas concentration, C, will follow

$$\sigma = \sigma_0[1 + A_g C(x,t)]$$

Where σ_0 is the baseline conductivity (i.e. the conductivity when the test gas is not present) and A_g is the sensitivity (also referred to as the response coefficient). For a p-type material, or if the gas is an oxidising agent, then there will be a decrease in conductivity or alternatively, as it will be considered here, an increase in resistivity, ρ: $\rho = \rho_0[1 + A_g C(x,t)]$, where ρ_0 is the baseline resistivity.

Reintroduced is the empirical form for response, equation 2.1: $G = A_g C_g^{\beta}$. Here the response exponent, β, is assumed to be 1 which although, as discussed in chapter 2, is often not the case, serves to reflect the underlying response behaviour of an ideal system [1][2].

Considering equation 4.1 and introducing dimensionless forms (in accordance with chapter 3) which incorporate the bulk effective diffusivity of the sensor layer, D_s, and

its length, h_s. $\tau = D_s t/ h_s^2 = t/T_s$ where $T_s = h_s^2 /D_s$; $X = x/ h_s$; $\Gamma = C/ C_0$ where C_0 is the gas concentration incident on the device the expression for current becomes:

$$i(\tau) = \sigma_0 A_g b \int_0^1 \Gamma(X,\tau) EdX + \sigma_0 b \int_0^1 EdX \text{ and } \Delta i(\tau) = \sigma_0 A_g b \int_0^1 \Gamma(X,\tau) EdX$$

And therefore the change in conductance is given by:

$$\Delta G(\tau) = \frac{\sigma_0 A_g b}{V} \int_0^1 \Gamma(X,\tau) EdX \qquad \text{Equation 4.2}$$

(4.2.3) Calculating the electric field

When a voltage is applied across the electrodes, an electric field is established within the sensing layer; hence representation of the field between the two electrodes is clearly an essential part of calculating the response. A number of different approximations have been used in modelling such systems. The wide-gap or “sandwich" model [3][4] assumes the electrodes are far apart and hence that the field is uniform throughout the layer. This is equivalent to placing the two electrodes either side of the sensing layer and yields a straightforward calculation. This model is obviously limited in that the response is known to depend on the electrode separation. When the electrodes are far apart the field is indeed expected to spread out throughout the sensing layer and at large enough separation the field will be essentially uniform within the layer. However, in moving the electrodes together, the field will become more confined within the region close to the electrodes. Two key models that do incorporate electrode geometry are the semi-infinite (electrodes long in the y- and z-direction) and finite coplanar models (electrodes long in the z-direction) [5][6].

For the semi-infinite configuration, Schwartz-Christoffel conformal transformations [7] can be used to solve Laplace’s equation in order to determine the electric field bisecting the electrodes:

$$E(X,0) = \frac{V}{h_s \pi} \frac{1}{\sqrt{X^2 + d^2/4h_s^2}}$$

For the finite coplanar case this is done using the Jacobean elliptical integral conformal transformation [8] and the electric field is given by:

$$E(X,0) = \frac{V}{2A^* {h_s}^2} \frac{1}{\sqrt{([X^2 + d^2/4h_s^2][M^2X^2 + d^2/4h_s^2])}}$$

Where the geometrical modulus, M, is defined as $w/(w+2d)$ and A^* is the complete elliptical integral:

$$A^* = \frac{2}{w}\int_0^1 \frac{dt^*}{\sqrt{([1-t^{*2}][1-M^2 t^{*2}])}}$$

Figure 4.2 gives the electric field bisecting the electrodes, calculated using the two coplanar models, as a function of distance from the electrodes. This was done for different electrode spacing, the result being in agreement with what is reasoned above. At large spacing the field is seen to be nearly constant throughout the layer whereas when the spacing is reduced the field becomes concentrated within the region close to the electrodes. This is observed to a lesser extent for the semi-infinite model – which is found to be equivalent to the finite model where the electrode width is large ($w/h_s > 5$). Note that in the limit of large d/h_s the calculated response for either coplanar model is equivalent to that determined from the wide gap approximation model discussed above.

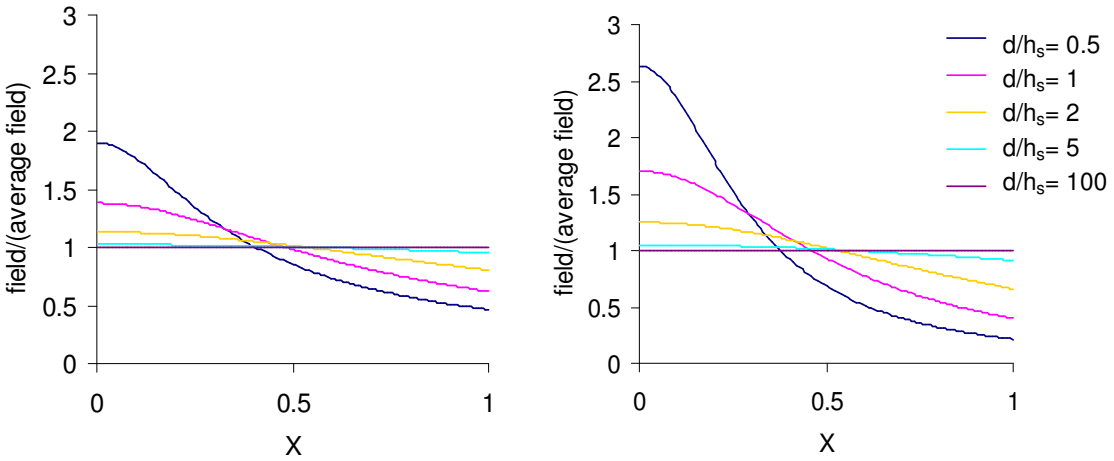

Figure 4.2: Electric field bisecting the electrodes as a function of distance from the electrodes for different separations for (a) semi-infinite and (b) finite (with width w/h_s=0.1) models.

Note the calculation time of response increases following wide gap < semi-infinite < finite. Here the finite electrode model is used to represent finite electrode separation; furthermore, for comparison of the wide and narrow gap responses, the wide gap response was calculated using the wide gap model in order to reduce computational effort.

(4.2.4) Calculating the response II

It is now possible to determine a form for the response in terms of the electrode separation relative to the thickness of the sensor layer. The result of principle interest is the fractional change in conductance $\frac{G(\tau)-G_0}{G_0}$. The forms for the two coplanar models are as follows:

(i) For the semi-infinite case:

$$\frac{[G(\tau)-G_0]}{G_0} = A_g \frac{\int_0^1 \Gamma(X,\tau)/\sqrt{((X-1)^2+d^2/4h_s^2)}dX}{\ln[1+\sqrt{(1+d^2/4h_s^2)}/[d/2h_s]]} \qquad \text{Equation 4.3}$$

Where G_0, the conductance in the carrier gas, is given by:

$$G_0 = (\frac{\sigma_0 b}{\pi})\ln\left[\frac{1+\sqrt{(1+d^2/4h_s^2)}}{d/4h_s}\right]$$

(ii) For the finite case:

Firstly the baseline response is given by:

$$G_0 = \left(\frac{\sigma_0 b}{2A^* h_s^2}\right)\int_0^1 \frac{dX}{\sqrt{([X^2+d^2/4h_s^2][M^2X^2+d^2/4h_s^2])}}$$

The change in transient gas-dependent response is given by:

$$\Delta G(\tau) = \frac{\sigma_0 A_g b}{2A^* h_s^2}\int_0^1 \frac{\Gamma(X,\tau)dX}{\sqrt{([X^2+d^2/4h_s^2][M^2X^2+d^2/4h_s^2])}}$$

And hence the fractional change in response is:

$$\frac{G(\tau)-G_0}{G_0} = A_g \frac{\int_0^1 \Gamma(X,\tau)dX/\sqrt{([X^2+d^2/4h_s^2][M^2X^2+d^2/4h_s^2])}}{\int_0^1 dX/\sqrt{([X^2+d^2/4h_s^2][M^2X^2+d^2/4h_s^2])}}$$

Equation 4.4

Alternatively one can model the fractional increase in resistance, *R*, by considering the relation between resistance and conductance: $R=\frac{1}{G}$. This is enforced for the

calculation of the current by reversing spatially the electric field bisecting the two electrodes.

As well as calculating a response transient, the fractional change in response can then be characterised by determining two key parameters; the steady state response and the response time, here defined as the time to reach 90% of the steady state response.

(4.2.4) Calculating the concentration

The concentrations of a reacting gas and its product(s) within the two layers are modelled by solving the reaction-diffusion equation, first introduced as equation 1.2 and given now in one-dimensional form as equation 4.5. Note it is also regarded that a first order reaction is generally valid in an excess of oxygen [8]. Here *r* and *p* subscripts represent reactant and product respectively:

$$\frac{\partial C_r(\vec{x},t)}{\partial t} = D_r \frac{\partial^2 C_r(\vec{x},t)}{\partial x^2} - k_r C_r(\vec{x},t) \qquad \text{Equation 4.5 (a)}$$

$$\frac{\partial C_p(\vec{x},t)}{\partial t} = D_p \frac{\partial^2 C_p(\vec{x},t)}{\partial x^2} + k_r C_r(\vec{x},t) \qquad \text{Equation 4.5 (b)}$$

It is assumed that the reactant and product do not interact [9] and hence the response from each species is calculated separately and then summed [1][2].

The ratio of sensitivities of the sensor to product and reactant is introduced as:

$R_{ag} = A_{gp}/A_{gr}$.

Before proceeding, equation 4.5 is normalised using the forms given in section 4.2.2. For the sensing layer:

$$\frac{\partial \Gamma_r}{\partial \tau} = \frac{\partial^2 \Gamma_r}{\partial X^2} - K_s \Gamma_r ; \quad \frac{\partial \Gamma_p}{\partial \tau} = \frac{\partial^2 \Gamma_p}{\partial X^2} + K_s \Gamma_r \qquad \text{Equation 4.6}$$

and for the zeolite layer:

$$\frac{\partial \Gamma_r}{\partial \tau} = \frac{D_{zr}}{D_{sr}} \frac{\partial^2 \Gamma_r}{\partial X^2} - K_z \Gamma_r ; \; \frac{\partial \Gamma_p}{\partial \tau} = \frac{D_{zp}}{D_{sr}} \frac{\partial^2 \Gamma_p}{\partial X^2} - K_z \Gamma_p$$

where $K_s = k_s T_s$ and $K_z = (k_z/k_s)K_s = k_z T_s$

To solve, the boundary conditions are $\Gamma_r(0) = 1$ and $\frac{\partial \Gamma_r(1)}{\partial X} = 0$ for the reactant and $\Gamma_p(0) = 0$ and $\frac{\partial \Gamma_p(1)}{\partial X} = 0$ for the product. At $\tau = 0$ there is zero gas concentration within the device.

The analytical solution of the steady state form of equation 4.6 for the reactant species within the sensor layer, where $h_z = 0$, is given by [3]:

$$\Gamma(X) = \frac{\cosh((1-X)\sqrt{K_s})}{\cosh(\sqrt{K_s})} \qquad \text{Equation 4.7}$$

When $h_z \neq 0$ and also in order to solve the time-dependent case, a numerical method for finding the concentration must be employed. The method used here is the standard explicit Euler method [10] in which the recurrence relation 4.8 is solved to give the concentration:

$$\Gamma_i(\tau + \Delta\tau) = \Gamma_i(\tau) + \lambda(\Gamma_{i-1}(\tau) - 2\Gamma_i(\tau) + \Gamma_{i+1}(\tau)) - K\Delta\tau\Gamma_i(\tau) \qquad \text{Equation 4.8}$$

And for which the following condition must hold for the calculation to be numerically stable:

$$\lambda \leq \frac{1}{2} \text{ where } \lambda = \frac{\Delta\tau}{\Delta X^2} \qquad \text{Equation 4.9}$$

(4.2.5) Outline of computational procedure

The reaction-diffusion code (on CD) was written to compute the electric field, concentration, current density, steady state response, response time and response transient of a two-phase model sensor system as described above.

The program process is represented as a flow chart in figure 4.3. Input options and function descriptions are also described within an example input file.

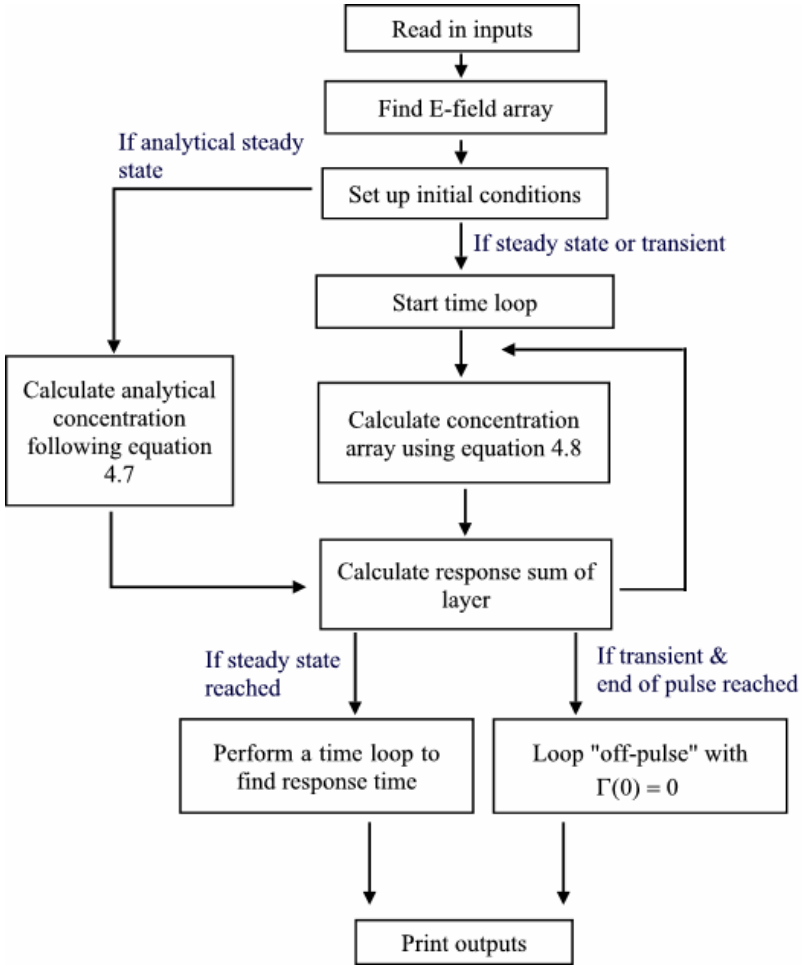

Figure 4.3: Flow chart to represent the computational process for calculating the diffusion-reaction dependent response following the method of finite differences.

In order to perform the numerical integration necessary to evaluate equation 4.4 (i.e. of the denominator of the form for the finite-coplanar response model), Simpson's rule [11] for numerical integration is used. Additionally to find the electric field (as in figure 4.2) the elliptic integral must be evaluated: $A^* = \frac{2}{w}\int_0^1 \frac{dt^*}{\sqrt{([1-t^{*2}][1-M^2 t^{*2}])}}$

This has the form of a complete elliptic integral of the first kind and can hence be calculated by evaluating the following series expansion:

$$A^* = \frac{\pi}{2}\left\{1+\left(\frac{1}{2}\right)^2 M^2 + \left(\frac{1\cdot 3}{2\cdot 4}\right)^2 M^4 + \cdots + \left[\frac{(2n-1)!!}{(2n)!!}\right]^2 M^{2n} + \cdots\right\}$$

For the other geometries, the response expressions can be evaluated straightforwardly, where the necessary inputs are supplied from the input file. The steady state response, in

the numerical case, is identified by comparing the responses calculated over several successive time steps. An example input file is given below:

```
# anything after hash ignored

# chose electrode geometry. Geometry options are wide_gap,
semi_infinite (response is solved following equation 4.3) or
finite (response is solved following equation 4.4)
geometry finite

# chose calculation type. Calculation options are transient
(finds the response transient) steady_state (steady state and
response time are calculated via analytical computation of the
concentration (equation 7.8))) and non_analytical_ss (steady
state and response time are calculated via numerical computation
of the concentration (equation 7.8))
calculation_type non_analytical_ss

# chose concentration calculation method. Options are cra_nic
(Crank-Nicolson method) or euler (Euler method, as in equation
7.8)
conc_method euler

# set β value i.e. the response exponent (equation 2.1)
beta 1

# define zeolite length as a fraction of total length (h_s)
fraction_zeolite 0.5

# set electrode parameters i.e. gap (d) and width (w) relative
to h_s
gap 0.5
width 0.1

#set space and time steps
dx 0.008
dt 1e-6

# define diffusion and reaction parameters for up to 3 gases.
These are dimensionless diffusivity within the zeolite layer
(dz) and dimensionless rate constant in sensor (ks) and zeolite
(kz) layers. Also the initial concentration (cmax) within the
layer and the gas sensitivity are required. Gas number 2 is the
product gas of gas number 1. If a 3 gas scheme is to be
considered (as indicated by non-zero rate for gas 3), gas 3 is
the product gas of gas 2. (Note the zeolite diffusivity is
normalised by the sensor diffusivity.)
gas_number one
dz 1
kz 0
ks 0
cmax 1
sensitivity 0

gas_number two
cmax 0
sensitivity 1

gas_number three
```

```
dz 1
kz 0
ks 0
cmax 0
sensitivity 0

# If want to monitor concentration at a certain point, set
height
height 10

# define total (dimensionless) time (time) and time of on-pulse
(pre_) and off-pulse (pulse)
time 25
pre_ 0
pulse 25

# chose whether calculate increase in resistance (resist) or
conductance (conduct)
res_cond resist
```

Figure 4.4: Example input file.

Note using the wide gap and semi-infinite approximations, the computation times range from about 1-5 minutes. Calculations using the finite coplanar electrode geometry may take as much as an hour for a composite, narrow spacing system on a 4GB processor.

(4.3) Results

(4.3.1) Discussion of model accuracy

Before proceeding there are several points worth making about the accuracy of the method employed here. Firstly it is noted that once a steady state is reached a non-reacting gas will give zero gradient in concentration throughout the thickness of the device. The response should therefore not be dependent on the electrode spacing – this can then be used as a test of accuracy of the calculation of the steady state response. For this purpose the concentration was calculated using the analytical expression equation 4.7 on wide and narrow electrode spacing and the percentage error was calculated by comparing the actual difference in concentrations to the expected zero concentration.

As shown in figure 4.5, the percentage error was seen to increase as the electrode separation was decreased and the semi-infinite system error was lower than that of the finite system as one would expect as the calculation is less involved. However, there is clearly greater approximation with the assumption that the electrodes are infinitely long – this results in the extent to which varying the electrode separation varies the response

being reduced (as seen in figure 4.2). The actual electrodes will form a more dipole-like field and hence the finite coplanar model is a better similitude (as a suitably low percentage error can be achieved).

For calculating the steady state response it is advantageous to use as small a space interval, ΔX, as possible to reduce truncation errors. This is also the conclusion from investigation of the calculation of the concentration (this is indeed a first order method) for which the analytical and numerical concentrations were compared.

Another point to note is that the formulation of equation 4.8 implies that the diffusion and reaction terms are decoupled – which is not in fact realistic. This will lead to inaccuracy of the calculation if the change in concentration within the set time interval is too large. This implies that a small time step, $\Delta\tau$, is also beneficial – and this is in fact also a requirement of numerical stability as in equation 4.9. However, it was found that reducing $\Delta\tau$ much below $5\text{x}10^{-7}$ actually led to a reduction in accuracy of the calculation of response time due to the accumulation of round-off errors occurring over the large number of steps comprising the computation. One method investigated for improving the accuracy of the response time was to employ the more implicit Crank-Nicolson method [10]. However, this is not applicable where both reactant and product species are of interest (i.e. where $R_{ag} \neq 0$). Reasonable agreement was, however, found between both methods over a suitable range of parameters of interest here for the R_{ag}=0 case. A possible alternative would be to use the Rudolph method [12] which is a matrix solving based approach, although this is not considered here to be a worthwhile task.

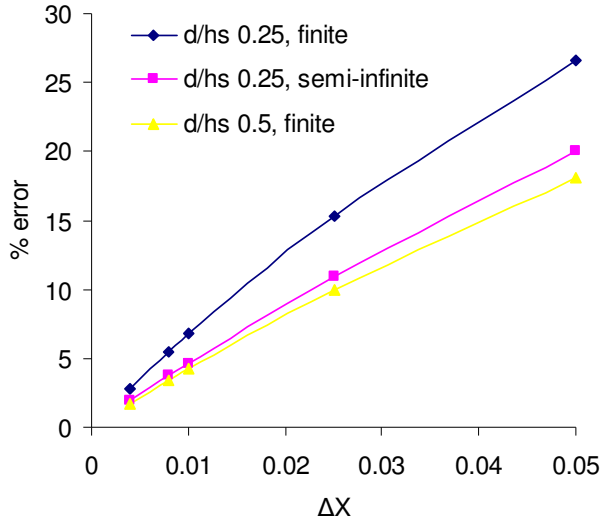

Figure 4.5: Percentage error of difference in steady state response non-reacting gas for wide and narrow electrode separations calculated using different approximations.

After taking into account all of the issues discussed the following calculations have been performed using $\Delta X = 8\text{x}10^{-3}$ and $\Delta\tau = 1\text{x}10^{-6}$. These gave a good agreement to the Crank-Nicolson method for the $R_{ag} = 0$ case and a percentage error of less than 2% for $d/h_s = 0.25$ and less than 1% for $d/h_s = 0.5$ for both response and concentration checks with a stable response time over the range of different parameters used. Note what is referred to as the "narrow gap" was taken to be $d/h_s = 0.5$. The wide gap approximation was used for the "wide gap" calculations.

(4.3.2) Single phase sensor

We now consider the dependecy of steady state response and the response time on the ratio of response coefficients (R_{ag}), the rate kinetics (K_s) and the electrode spacing (d/h_s) for a single phase model sensor device.

Example response transients are given in figure 4.6 for which the fractional change in response is plotted as a function of dimensionless time ($\tau = D_s t/h_s^2$). The gas stream is switched on at τ=0 and off at τ=1. Cases of the introduction of test gas giving an increase in resistance, figure 4.6(a), and an increase in conductance, figure 4.6(b), are considered. Responses have been calculated for narrow and wide electrode gaps and for the passive ($K_s = 0$) and reactive cases where the product is either more or less sensitive than the reactant which has a sensitivity of 1. Ratios of sensitivity R_{ag}=0.5 and R_{ag}=2 are considered.

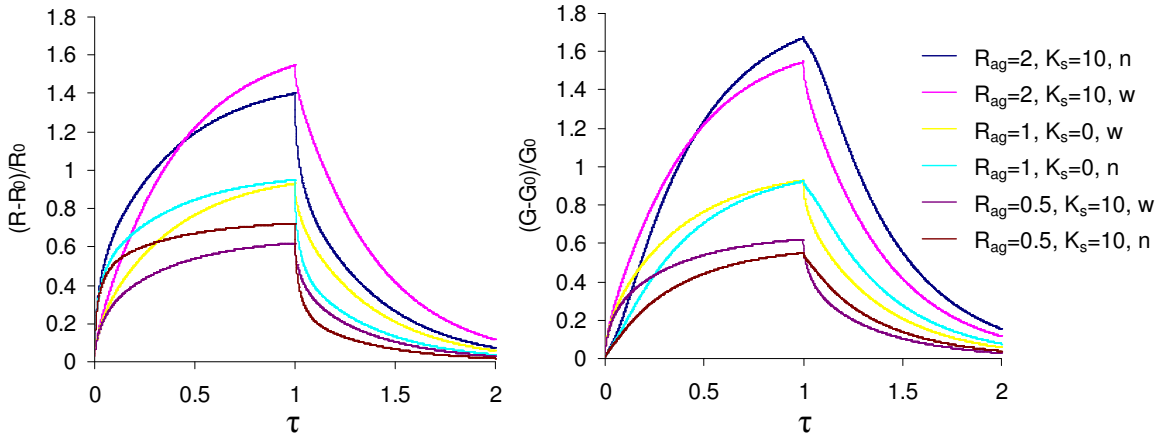

(a) (b)

Figure 4.6: Transient response as a function of dimensionless time on wide, w, and narrow, n, electrode gaps where the response is an (a) increase in resistance and (b) increase in conductance. Different sensitivities of reactant and product are shown as indicated by the ratio $R_{ag} = A_{gp}/A_{gr}$.

As is clearly expected, when the product sensitivity is less than the reactant sensitivity, R_{ag}<1, the response is reduced below that of the passive case and where the product sensitivity is higher than that of the reactant, R_{ag}>1, it is increased.

The steady state response is also modified on changing the electrode separation depending in turn on what the response output is. The behaviour is summarised in table 4.1 below and is understood with reference to figure 4.2 which shows the increase in field density in the region near the electrodes as the separation between them is decreased. Figure 4.7(b) gives the steady state gas concentration profile of reactant and product for K_s=10 and it is noted that, along as $R_{ag}\neq1$, there is effectively a gradient of sensitivity through the length of the device. As the product concentration increases on approach of the electrodes, for the narrow electrode separation this coincides with the denser region of electric field and hence the conductance change is expected to be higher for a narrow gap sensor if R_{ag}>1. For a device that gives a resistance increase, the field is effectively inverted and hence a higher response is expected on the wide gap. Converse arguments can be made for the R_{ag}<1 case.

R_{ag}	**Conductance Increase**	**Resistance Increase**
>1	G(wide)<G(narrow)	R(wide)>R(narrow)
<1	G(wide)>G(narrow)	R(wide)<R(narrow)
=1	G(wide)=G(narrow)	R(wide)=R(narrow)

Table 4.1: Summary of steady state responses on different electrode separations for different response outputs.

For R_{ag}=1, i.e. the passive case, there is variation in the response time with electrode spacing but no variation in the response reached in the long time limit – again as expected based on the earlier discussion. The variation in response time comes about as the dense field takes longer to respond than the sparse field, hence for a conductance increase the response takes longer on the narrow gap and for a resistance increase the response takes longer on the wide gap, true for all ratios of sensitivity.

Figure 4.7: Steady state concentration, as a function of the distance from the electrodes, of reactant (green) and product (grey) where the gas reacts at rate constant (a) K_s =2, (b) K_s =10 and (c) K_s =30.

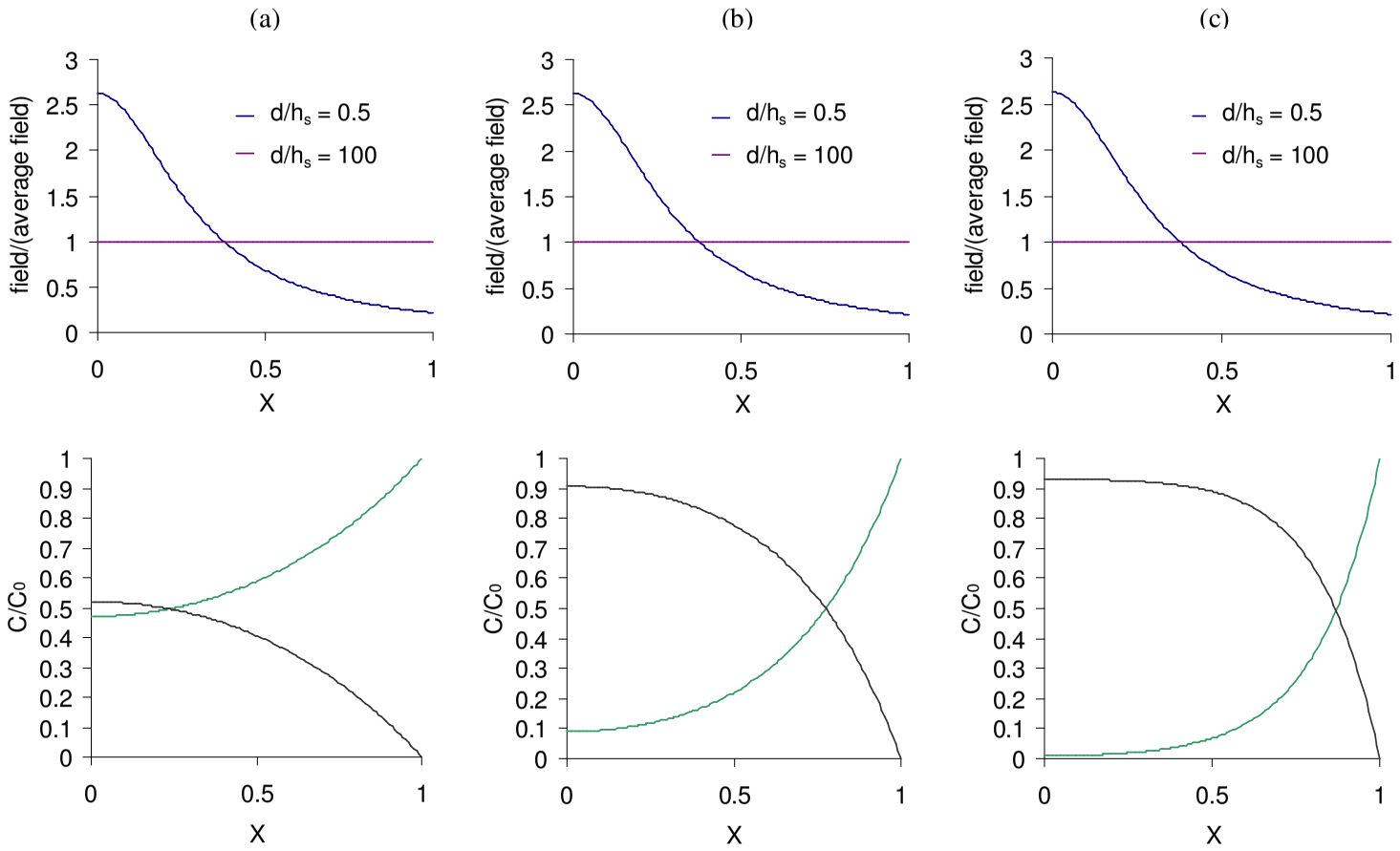

In order to clarify what has been discussed so far and probe further the different dependencies, steady state response and response time values and their differences on narrow and wide electrode spacing are plotted as functions of K_s (figure 4.8) and R_{ag} (figure 4.9).

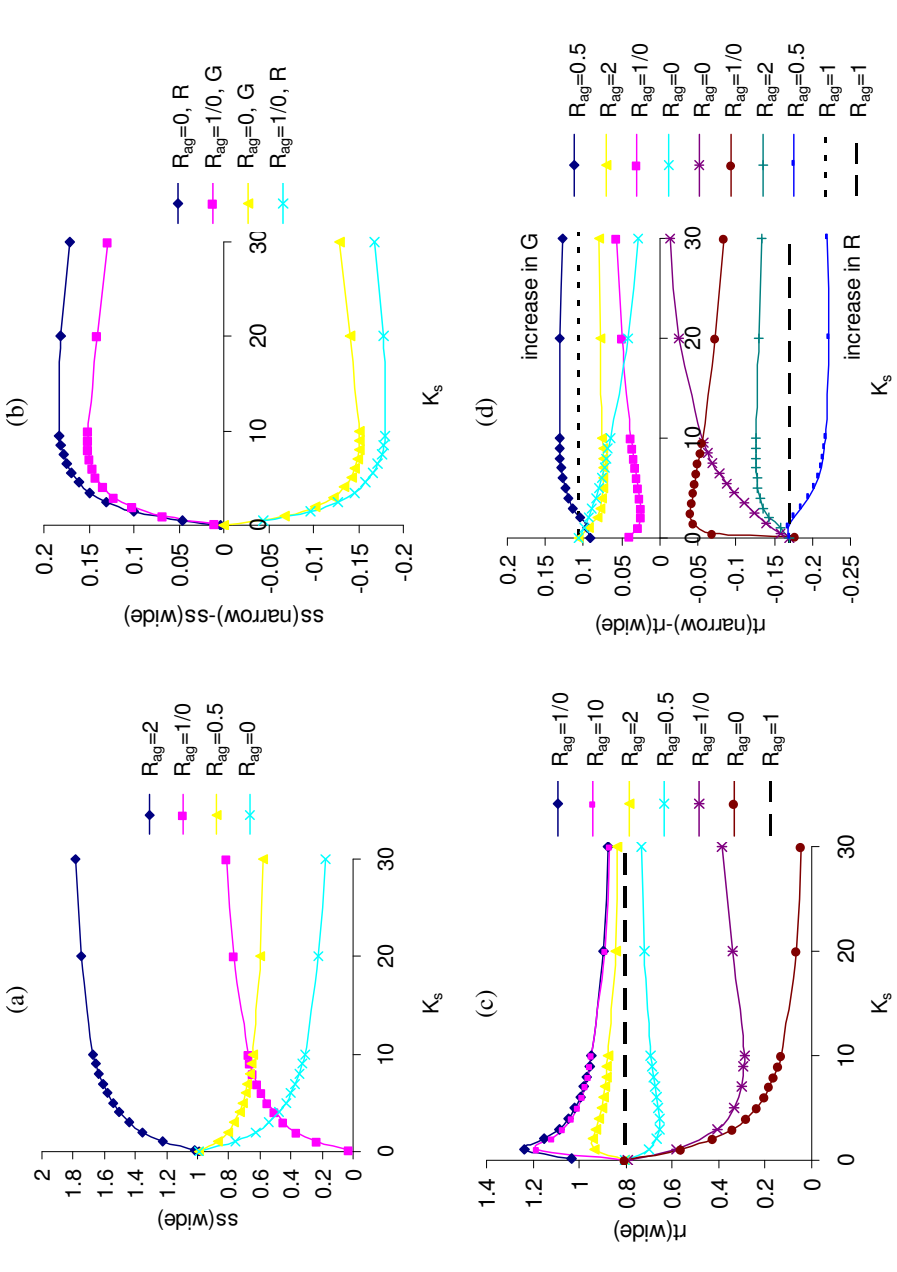

Figure 4.8: (a) steady state response calculated using the wide gap model, (b) difference in steady state response on narrow and wide electrode separations, (c) response time calculated using the wide gap model and (d) difference in response time on narrow and wide electrode separations as a function of K_s for different R_{ag} values and response outputs. ss = steady state response, rt = response time.

Figure 4. 9: (a) steady state response calculated using the wide gap model, (b) difference in steady state response on narrow and wide electrode separations, (c) response time calculated using the wide gap model and (d) difference in response time on narrow and wide electrode separations as a function of R_{ag} for different K_s and response outputs. ss = steady state response, rt = response time. The reactant sensitivity is here constant at A_{gr}=1.

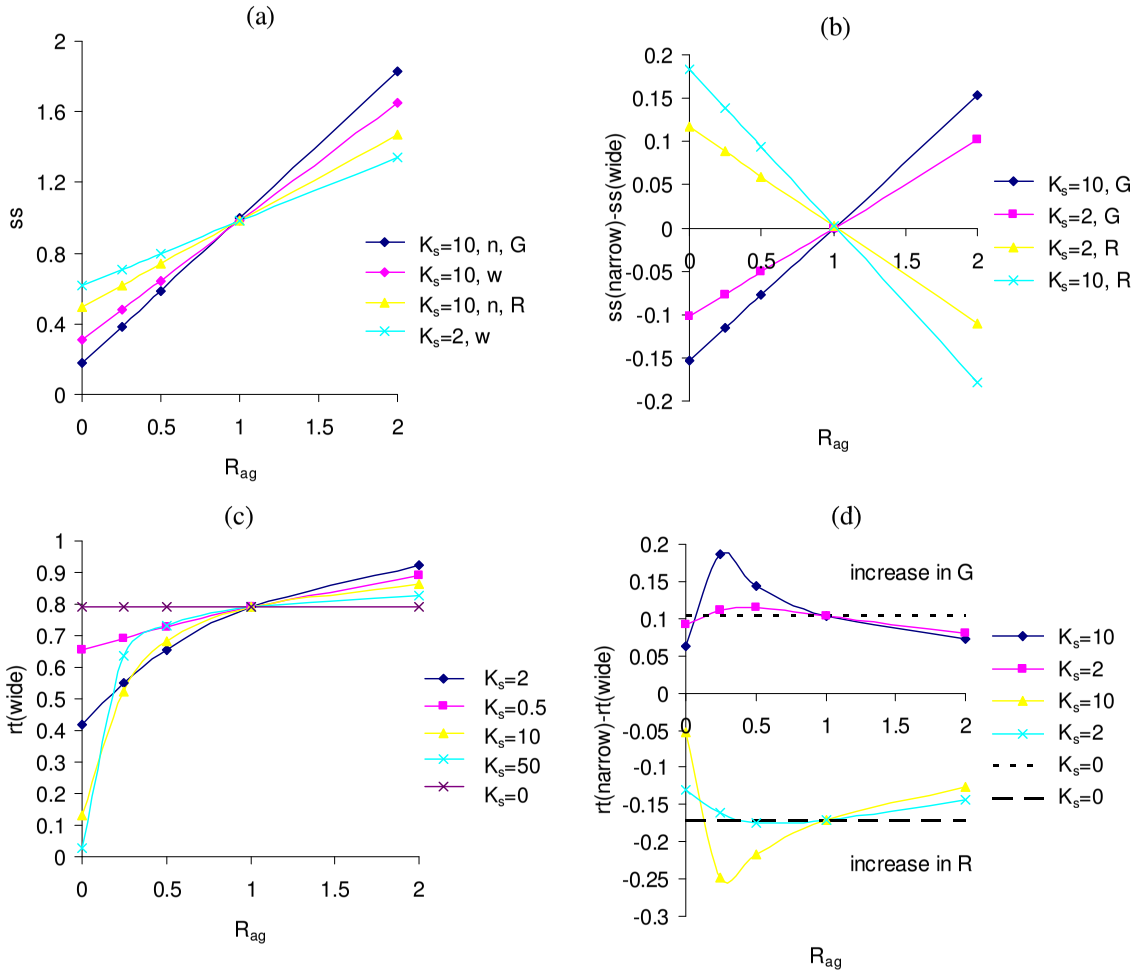

Steady State Response

As was observed from figure 4.6, figure 4.8(a) shows the steady state response (either resistance, R, or conductance, G) decreasing with rate constant for R_{ag}<1 and increasing for R_{ag}>1. The rate of this variation diminishes as K_s increases as there is a maximum (and minimum) total concentration the system can hold – this is mirrored in the real system which can hold a limited concentration of gas depending on the size of the pores of the sensor material. The steady state response depends on the total sensitivity of the reactant and product. Note the response may be divided by the total sensitivity to obtain a value that is independent of individual sensitivities. Where the reactant sensitivity is kept constant, as in figure 4.9, both the steady state response and the difference in steady state response increase linearly with R_{ag} (i.e. as the product becomes more sensitive), the slope depending on K_s, d/h_s and the response output.

Figure 4.8(b) gives the difference in steady state response for different response outputs (behaviour as given in table 4.1) as a function of K_s, the difference magnitude initially giving a sharp increase with increasing K_s and then slowly decreasing after approximately K_s=10. Considering figure 4.7, it is noted that as K_s increases, the gradient in reactant or product concentration becomes confined to the region near the point of gas release and approaches uniformity closer to the electrodes. Consequently there will be less variation in response on the two electrode separations for larger K_s. The K_s value for which the maximum (in magnitude) occurs depends on the two values for electrode spacing chosen – this point is further illustrated in figure 4.10 which gives the steady state response as a function of both K_s and the electrode spacing. An example is considered, indicated by the dashed lines marked on figure 4.10(a), of how two gases are distinct in terms of the difference in steady state response on different electrode spacing with a narrow spacing d/h_s=0.5 but not if this is increased to d/h_s=1 or decreased to d/h_s=0.25.

Figure 4.10(b) shows how the response variation with electrode spacing and rate constant may depend on the sensitivity ratio. In (b) the ratio of sensitivities is R_{ag}=2 and the total sensitivity is 1.5 whereas in (a) R_{ag} is very large and the total sensitivity is 1. The steady state response reached over the K_s range is similar in each case. The contours have the same direction for both examples, i.e. the steady state response

increases with increasing K_s and decreasing electrode spacing in both cases. However, the variation is less for (b) with both K_s and d/h_s. Comparing these two plots it is observed that there will be instances where two different gases – for example gas 1: K_s=25, R_{ag}=1/0; gas 2: K_s=7, R_{ag}=2 – will give both the same steady state response and the same difference in steady state response on a narrow and wide spacing – here there will be a need for further analysis in order to discriminate between the gases.

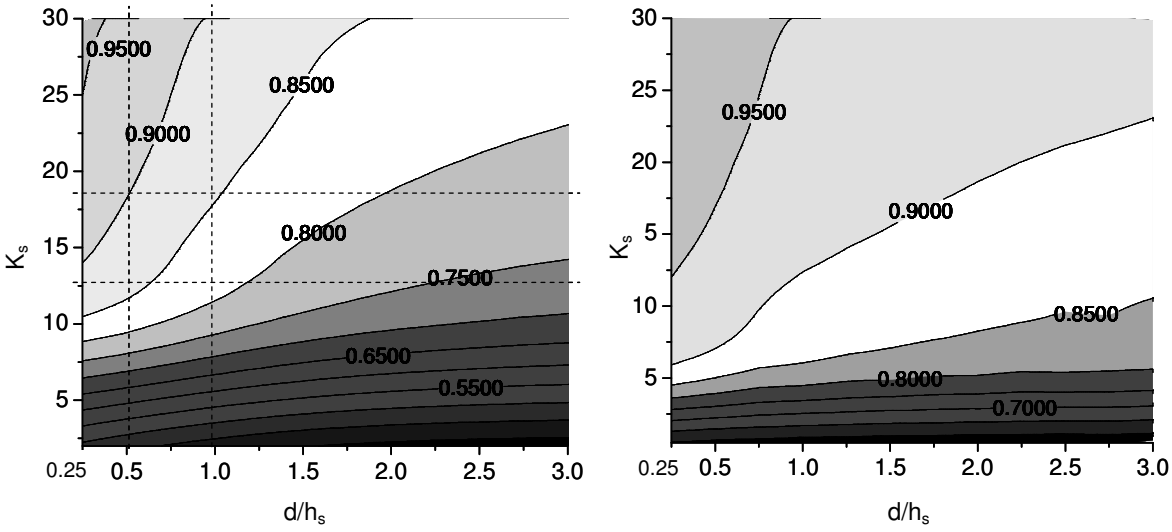

Figure 4.10: Contour plot giving the steady state response as a function of the electrode gap d/h_s and dimensionless rate constant K_s with (a) R_{ag}=1/0 and (b) R_{ag} = 2 (where A_{gr}=0.5 and A_{gp}=1). Contours are lines of constant $(G-G_0)/G_0$.

Response Times

The response time is independent of the individual sensitivities of the reactant and product depending only on, and increasing with, the ratio R_{ag}. From figure 4.8(c) and figure 4.9(c) it is observed that for R_{ag}>1 the response time tends to the passive case (R_{ag}=1) response time for large K_s and where the reaction is to an entirely insensitive product (R_{ag}=0) it tends to zero, as one would expect. For 0<R_{ag}<1 the response time behaviour is intermediate between the R_{ag}=0 and R_{ag}=1 cases, initially decreasing with K_s, as in the R_{ag}=0 case, but then increasing to the R_{ag}=1 case, such that there is a minimum in response time with K_s depending on R_{ag} (and the electrode separation). Another point to note is where an entirely insensitive reactant coverts to a sensitive product (R_{ag} very large) at a low rate. At K_s=0 there is no response and hence zero response time such that the calculation yields an immediate sharp increase of response

time where K_s is small but finite, giving a maximum from which the response time decreases to the R_{ag}=1 response time as K_s thereafter increases. The R_{ag}>1 response time is always greater than the R_{ag}<1 response time as the region of high concentration of sensitive gas, to which the sensor takes longer to respond, is established after the time of gas release in the former case and at the point of gas release for the later case.

Figure 4.8(d) gives the difference in response time on wide and narrow separations as a function of K_s. As has been discussed for figure 4.6, for a conductance increase there is a slower response on the narrow separation whereas for a resistance increase there is a faster response on the narrow gap. Considering the magnitude of the response time difference, the same trends for the two response outputs, in terms of R_{ag} and K_s, are observed. Similarly to the response time itself, for large K_s the response time difference for the R_{ag}=0 case tends to zero difference whilst the large R_{ag} case tends to the R_{ag}=1 difference and extrema in the variation with K_s for $0<R_{ag}<1$ and R_{ag} large occur at the same points. Considering figure 4.9(d), one observes that there is a maximum in difference in response time on the two different electrode spacing with R_{ag}, which again will depend on the values for electrode separation chosen.

Figure 4.11 further illustrates this somewhat complex behaviour giving the response time as a function both of the electrode spacing and the rate constant for two different sensitivity ratios. Figure 4.11(a) gives the case of large R_{ag}, where the reactant is insensitive, it is observed that where K_s is less than around 10, there is little change in the response time with electrode spacing (compared to the amount the response time changes with K_s). Using response time measurements on different spacing is more likely to be useful to distinguish between two gases of high K_s. This analysis is very sensitive to R_{ag}: for R_{ag}=2 (total sensitivity 0.5), as in figure 4.11(b), for low K_s there is slower variation with K_s and greater variation with d/h_s than in the large R_{ag} case (total sensitivity 1). We can compare this to figure 4.10 which gives the steady state response for the same systems. Where in fact the R_{ag}=2 case has little variation in steady state response on different separations with low K_s, response time variation is significant. Returning to the two theoretical gases discussed for the steady state contours (gas 1: K_s=25, R_{ag}=1/0; gas 2: K_s=7, R_{ag}=2), if the response times on different separations are also taken into account we see it would now be possible to discriminate between them.

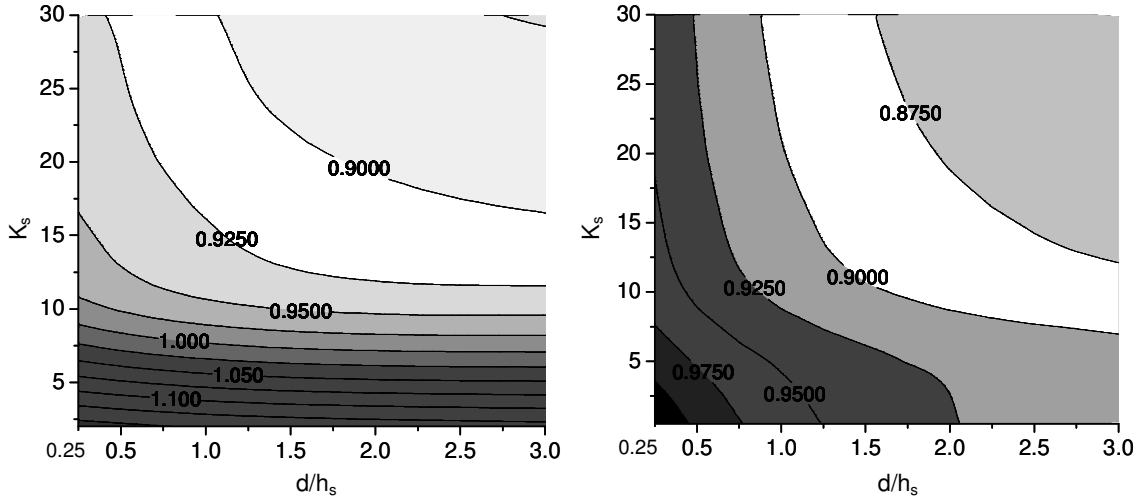

(a) (b)

Figure 4.11: Contour plots giving the response time as a function of the electrode gap d/h_s and dimensionless rate constant K_s with (a) R_{ag} = 1/0 and (b) R_{ag} = 2 (where A_{gr}=0.5 and A_{gp}=1). Contours are of constant $(G-G_0)/G_0$.

(4.4.3) Inclusion of a zeolite over-layer

The response can be further modified with the introduction of a zeolite over-layer. The presence of the over-layer alters the concentration profile within the sensing layer by altering the gas concentrations incident upon it at a given time. As has been discussed, the zeolite may have two key roles as part of the sensor system; to act as a diffusive barrier and to modify the constituents of the gas stream via catalytic activity.

Figure 4.12 gives the response, here a resistance increase, of a composite device where no reaction occurs in the zeolite and it acts in the first sense – as a diffusive barrier. The response times are increased in all cases with the inclusion of the zeolite, as expected, as the gas has a further distance to diffuse. Such behaviour has been observed experimentally [13]. A characteristic timescale, T_z, can be defined for the zeolite layer, as with the sensor layer, as $T_z = h_z^2 / D_z$. The composite device will have a characteristic timescale dependent on both that of the zeolite and sensor layer with an effective diffusion coefficient which will be dominated by whichever layer the gas diffuses most slowly in.

Figure 4.12(a) gives the response where no reaction occurs within the sensor layer; here the only effect of the zeolite is to slow the response and therefore the steady state response reached will be the same as the sensor only system but the response reached

within the measurement time period may be reduced. In figure 4.12(b) and (c) a reaction (K_s=10) occurs within the sensor with R_{ag}=0.5 and R_{ag}=2 respectively. In these instances, although no reaction occurs within the zeolite, the presence of the additional layer actually promotes the reaction that occurs in the sensing layer as the product is effectively removed as it passes into the zeolite layer. Concentration profiles for systems with different thicknesses of zeolite overlayer are given in figure 4.13. The concentration of the product is seen to reach an increasingly higher value in the sensing layer as the length of the zeolite phase is extended. A second conclusion that can be drawn from consideration of figure 4.13 is that, as the electrodes are assumed to probe only the sensing layer, any difference in response on varying electrode separation will be reduced on the addition of the zeolite layer. This is as shown in figure 4.15.

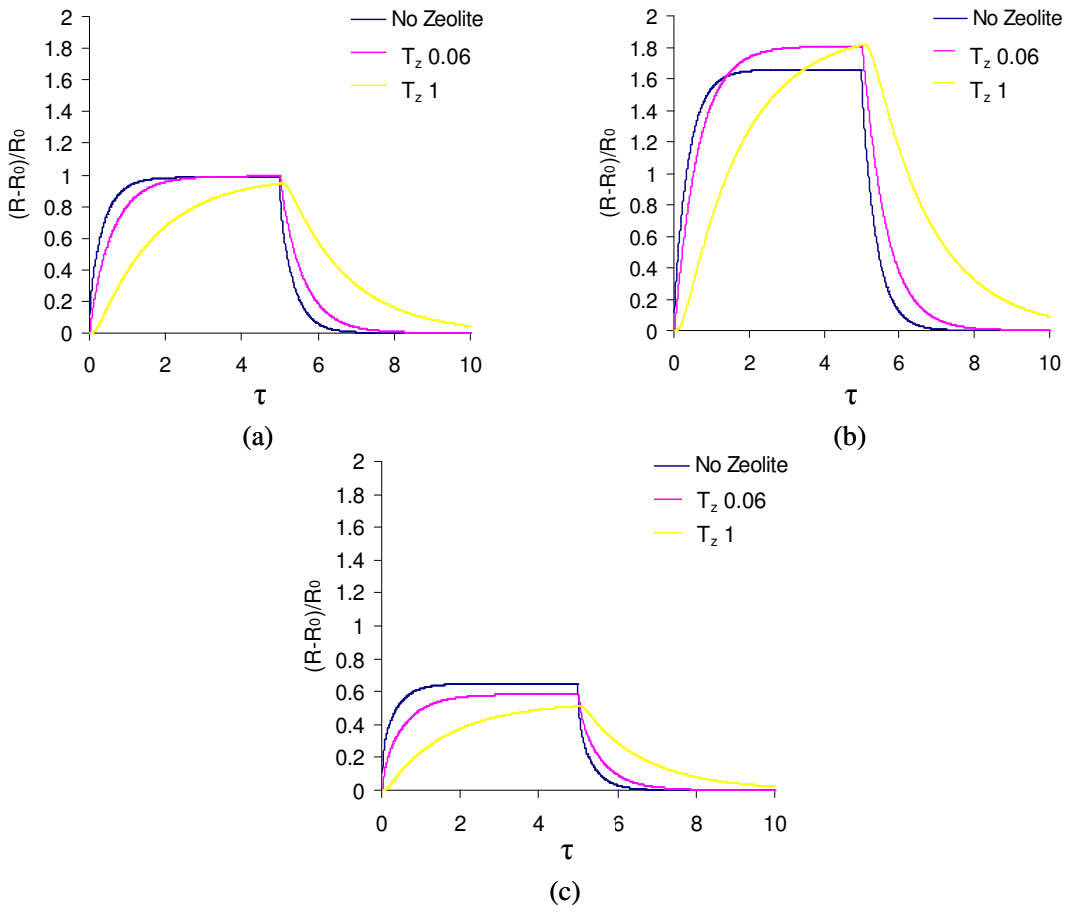

Figure 4.12: Fractional change in resistance (on wide gap) as a function of dimensionless time for composite sensor with dimensionless rate constant (a) K_s = 0, (b) K_s = 10, R_{ag} = 0.5 and (c) K_s = 10, R_{ag} = 2 (where $R_{ag} = A_{gp}/A_{gr}$).

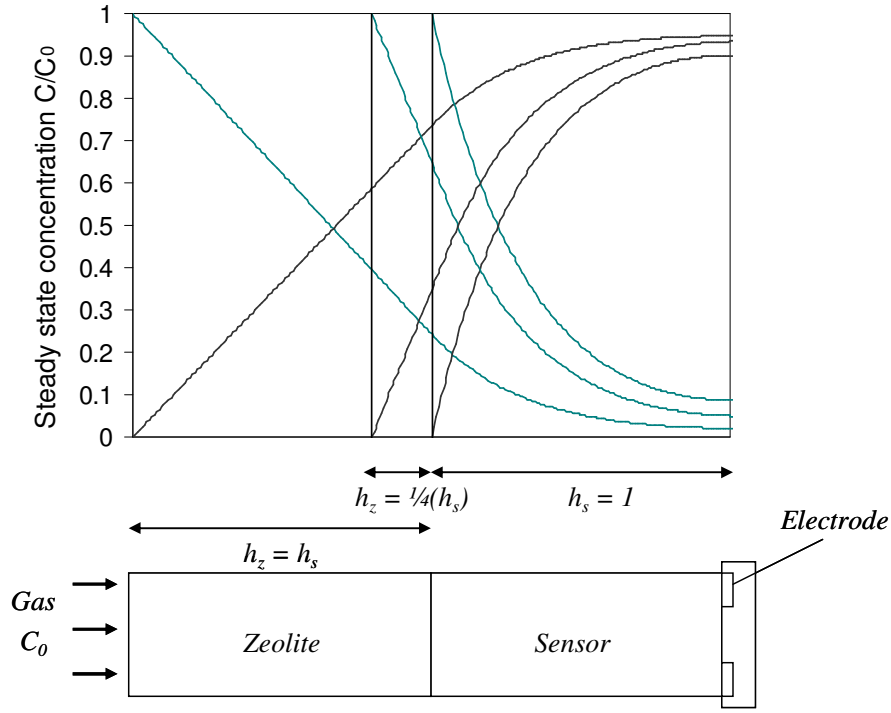

Figure 4.13: Steady state concentration of reactant (green) and product (grey) for a system with dimensionless rate constant K_s = 10 with zeolite overlayer of different thicknesses with K_s = 0.

Figure 4.14 and figure 4.15 demonstrate the simplest extension of the model to include the occurrence of a reaction within the zeolite layer, considering the two gas scheme where the same reaction occurs in both layers. Note the response again is modelled as a resistance increase. As with the sensor layer, the zeolite may enhance or diminish the response dependent on R_{ag}. The nature of the calculation determines the natural normalisation of the rate constant in the zeolite to be $K_z=k_zT_s$. However, as with K_s, the steady state response reached depends on K_zT_z, independent of the individual values of K_z and T_z – i.e. if the residence time of the gas in the zeolite is long then the gas reacts over a long time. The extent to which the response time is increased depends on the time constant T_z as seen above (unless otherwise stated, $T_z = T_s$).

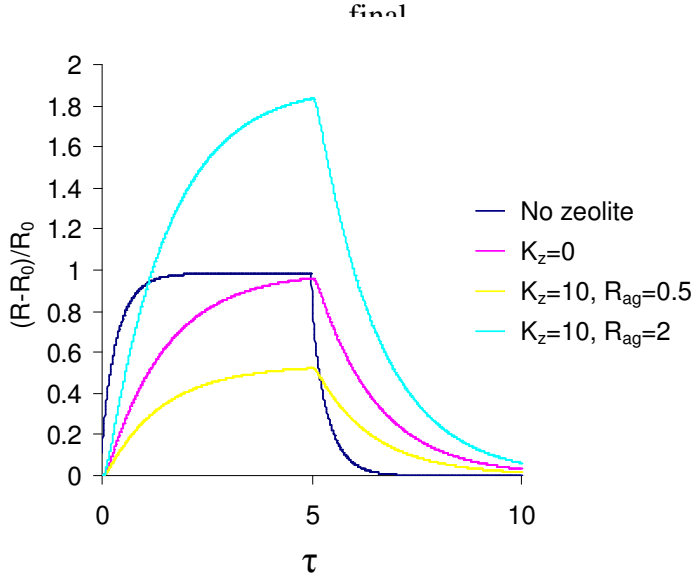

Figure 4.14: Fractional change in resistance (on wide gap) as a function of dimensionless time for composite sensor for different K_z where K_s = 0.

The extent to which the response is enhanced depends not only on K_z but also on K_s as there is a limit to the response that can be reached for a given sensitivity as discussed above; this is illustrated in figure 4.15(a). The difference in steady state response on wide and narrow spacing (figure 4.15(b)), as discussed above, is less than for the sensor only system and is reduced even further when a reaction occurs in the zeolite as, due to the use of the simple two gas scheme, the effect of the zeolite reaction is to move the region of steepest gradient in concentration further into the zeolite where the current does not probe.

Figure 4.15(c) and (d) give the response times on a wide gap system and the differences in response time on wide and narrow electrode spacing respectively. As has been discussed, response times are increased (where R_{ag} is constant) on the introduction of the zeolite layer. As with the sensor only system, as either K_s or K_z increases, the R_{ag}=0 case will tend to zero response time whereas the large R_{ag} case tends to the response time of the passive case (for the composite device). As with the difference in steady state response on different electrode separations, the difference in response time is reduced on the addition of the zeolite, the same effect being observed as for the response time in that with increasing K_s and K_z the difference in response time for R_{ag} = 0 tends to zero and for $R_{ag} > 1$ it tends to the R_{ag} = 1 difference.

Figure 4.15(a) steady state response calculated using the wide gap model, (b) difference in steady state response on narrow and wide electrode separations, (c) response time calculated using the wide gap model and (d) difference in response time on narrow and wide electrode separations as a function of K_s for different R_{ag} values and response outputs for single layer and composite model sensors of different K_z (Unless stated otherwise h_z=1). ss = steady state response, rt = response time.

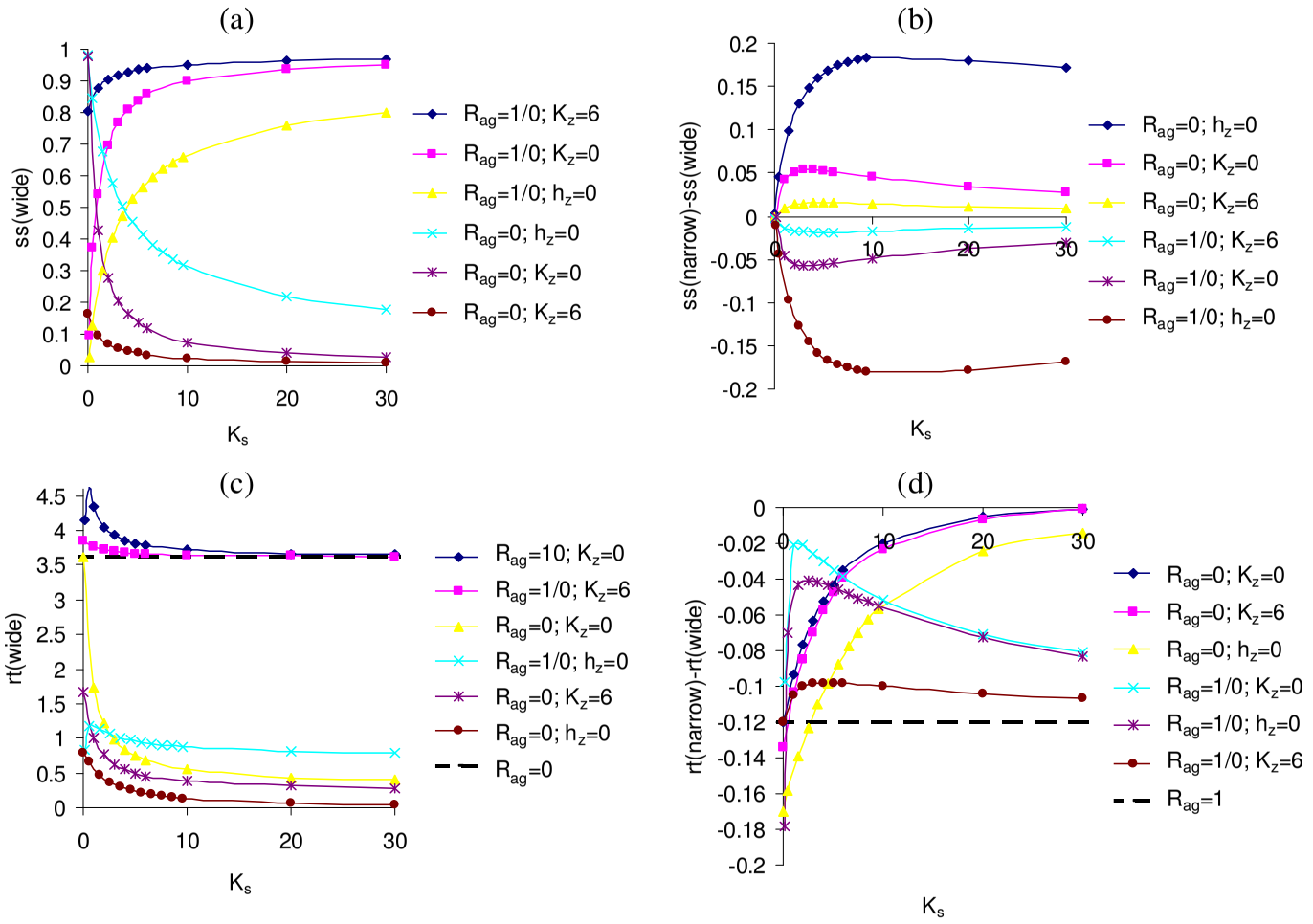

So far it has been shown how the zeolite may diminish differences in response on different electrode separations, compared to the sensor only system. Where no reaction occurs within the sensor, however, the zeolite will in fact act to produce such a difference, as illustrated in figure 4.16 where the sensor properties are kept constant, with K_s = 0, and the zeolite reactivity is varied. Figure 4.16(a) and (b) give the steady state resistance increase as functions of both K_z and the electrode separation, figure 4.16(a) gives low rate, K_z<10, and figure 4.16(b) gives higher rate, K_z>10. When K_z is low the increase in response that results from an increase in K_z is to such an extent that it dominates the behaviour and any changes on varying the electrode spacing are not apparent. This indicates that it would not be possible to distinguish between two gases of K_z within this range based on the difference in steady state responses. For larger K_z, differences over the range of spacing shown is comparable to those found on changing K_z and one would expect to be able to discriminate between gases with K_z within this range by comparing steady state response with different electrode separations. It is noted, however, that compared to the sensor only system, the variation with electrode separation diminishes more quickly, here after about d/h_s=1, with no further variation in response observed with increasing d/h_s for constant K_z. Using as small a separation as possible is more important where the zeolite is included as the gradient within the sensor layer is always of a lesser extent to the same system but without the zeolite.

The response time, figure 4.16(c), does vary significantly with electrode spacing over the whole range of K_z, here increasing as the gap size is widened. However, over the rage 20<K_z<50, the response time does not vary significantly with K_z on any one spacing and neither does the difference of response times on two spacing. Using response times for gases of high rate constant is therefore concluded not to be very useful for discrimination. However, this is the region where steady state response changes are more useful and in contrast the response time shows greater variation with electrode separation for low K_z for which the steady state response does not vary greatly.

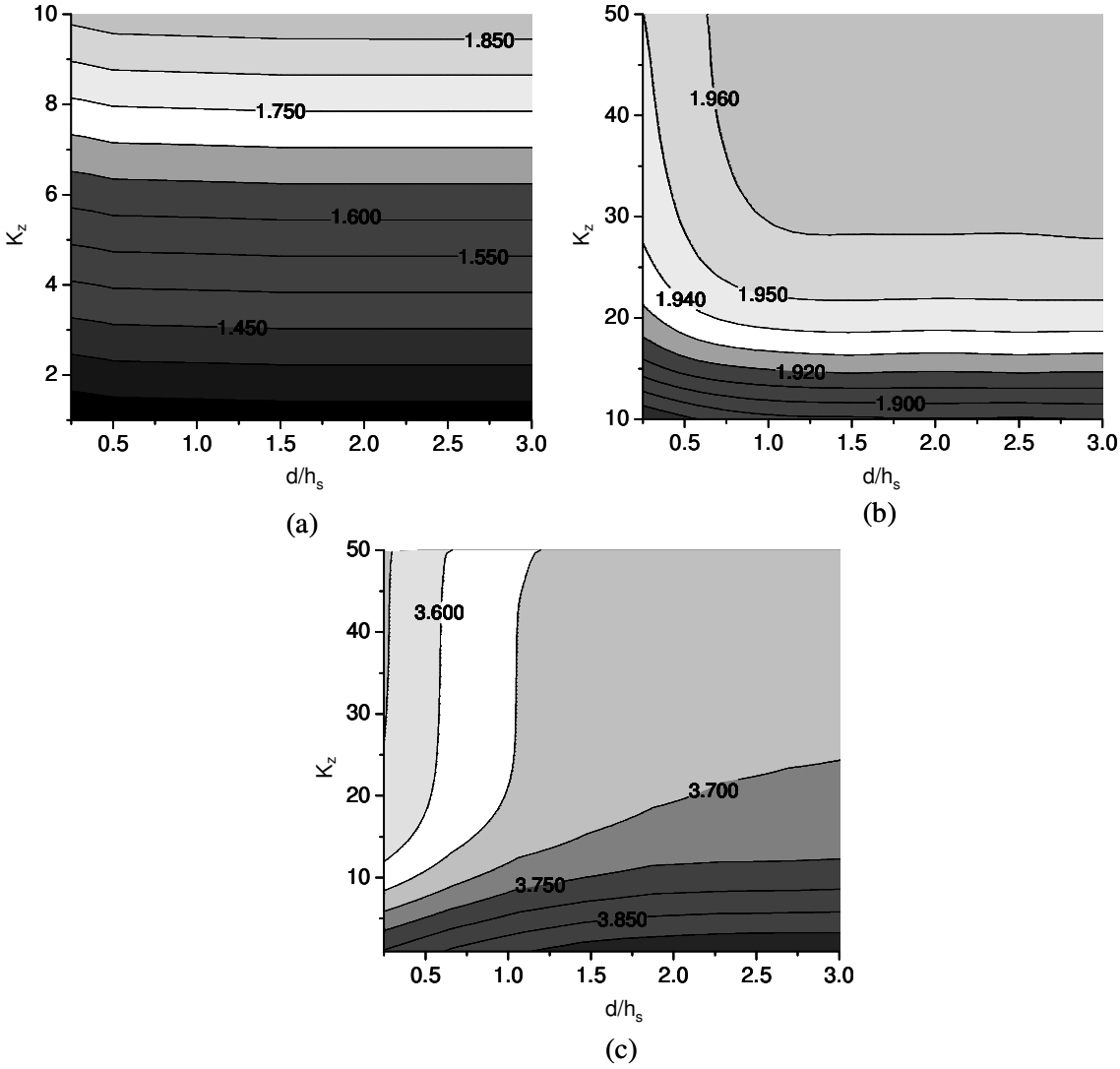

Figure 4.16: Contour diagrams – variation of (a) & (b) steady state response and (c) response time with gap and K_z for R_{ag} 2. Contours are lines of constant $(R-R_0)/R_0$.

(4.4) Conclusions

In the course of this chapter, through the use of a simple model of the composite sensor system, it has been demonstrated that the event of a porous semiconducting sensor layer responding to an influx of gas can be analysed to reveal different aspects of the nature of the gas in question. It is concluded that the results of calculations presented here, support that potentially, through both effective sensor design and effective analysis of response, a high level of discrimination between different gases can be achieved. This

behaviour is understood in terms of the balance between gas diffusion and reaction within the porous layers and the gas-specific concentration profiles that form as a result of this balance, where the rate at which these processes occur are dependent on the microstructure as discussed in the previous chapter.

Experimentally, the presence of the test gas may be observed as a resistance increase or decrease, which, following the standard characterisation and presuming that the sensor material is known to be either n-type or p-type, is indicative of the oxidising or reducing nature of the gas. The value of using different electrode spacing to measure the response, in order to further characterise the gas-type, is clear. The relative magnitudes of response on different spacing indicates the relative sensitivities of reactant and product and indeed whether a reaction occurs at all, and this is undoubtedly more instructive than simply referring to the magnitude of the response output. It has been shown how the spacing could be fine tuned to give maximum difference in response for a particular task.

It is also clear that the available discriminating power can be enhanced dramatically by monitoring the transient as well as the steady state behaviour. For a fixed sensitivity ratio the steady state response is determined by the dimensionless constant, K_s, and not by the individual values of rate constant and time constant. Hence two different gases of different rate constant and time constant but the same K_s will be indistinct in terms of their steady state response yet the response time may here be used to provide discrimination. Also if two gases have different sensitivity ratios and react at different rates, for instance, if gas one is insensitive and reacts to a sensitive product with a low rate constant and gas two is sensitive and reacts to an insensitive product with a high rate constant, then there is likely to be an overlap of their steady state responses, however, again their response times will be distinct. Also considering the response time on different electrode spacing is instructive as was demonstrated with figure 4.11.

Additionally, it has been established that a porous zeolite layer, positioned on top of the sensor layer, may perform two key roles – either acting as a diffusive barrier or catalytically modifying the gas stream. When the zeolite acts in the former sense, it is shown how both the response time and the steady state response can be modified. In this case, clearly the zeolite layer is expected to increase the response time – the

diffusivity through the zeolite layer depends on properties of the zeolite microstructure, as discussed in chapter 3, and a time constant can be assigned to the layer equal to h_z^2/D_z. The zeolite will also change the steady state response where a reaction occurs in the sensor by removing the product from the reaction region, hence acting to promote the reaction. In this role the zeolite can therefore be used to ensure gases have different response times or to enhance existing reactive differences between the gases.
If a reaction is catalysed in the zeolite, where the rate again depends on the microstructure as discussed in chapter 3, the signal may be enhanced or suppressed indicating a reaction is occurring to a more or less sensitive species.

The calculations presented here demonstrate only the occurrence of the simplest reaction scheme and hence predicts that the presence of the zeolite will cause a reduction in response differences on different electrode geometries, unless no reaction occurs in the sensor. This may not always be the case, in real systems more complex reaction schemes could occur such that the zeolite enhances response differences on variable electrode spacing. Also, here the response time is always predicted to increase on inclusion of the zeolite whereas in the real system the zeolite may give products which diffuse significantly quicker through the sensor phase than the reactant. It is noted that for high K_z, as discussed for figure 4.16, the response time does not vary greatly with either K_z of the electrode spacing and hence this is not such a grave issue. A conclusion can at least be made by elimination, on observation of the anomalous behaviour – i.e. that the product is diffusing more quickly than the reactant through the sensor. Of course, the real mechanisms of response and gas reaction are much more complex than is modelled here, however, that the diffusion and reaction balance is important is inarguably demonstrated and representing the complex systems with a simple model has the advantage of, whilst not capturing the finer details of the behaviour, being able to clearly expose the principle, underlying dependencies and predict the general scheme of the response behaviour.

References

[1] S.C. Naisbitt, K.F.E. Pratt, D.E. Williams, I.P. Parkin, Sensors and Actuators B-Chemical, 114 (2007) 969-977. “A microstructural model of semiconducting gas sensor response: The effects of sintering temperature on the response of chromium titanate (CTO) to carbon monoxide.”

[2] G. Chabanis, I. P. Parkin, Williams, D. E. Williams, Meas. Sci Technol, 14 (2003) 76-86. “A simple equivalent circuit model to represent microstructure effects on the response of semiconducting oxide-based gas sensors.”

[3] D.E. Williams, K.F.E. Pratt, J. Chem. Soc. Faraday Trans., 91 (1995) 1961-1966. “Theory of self diagnostic sensor array devices using gas-sensitive resistors.”

[4] K. Sahner, R. Moos, Phys. Chem. Chem. Phys., 9 (2007) 635-642. “Modelling of hydrocarbon sensors based on p-type semiconducting perovskites.”

[5] J.W. Gardner, Sens. Actuators, 18 (1989) 373-384. “Electrical conduction in solid-state gas sensors.”

[6] J.W. Gardner, P.N. Bartlett, K.F.E Pratt, IEE Proc.-Circuits Devices Syst., 5 (1995) 321. “Modelling of gas-sensitive conducting polymer devices.”

[7] V.I. Ivanov, M.K. Trubetskov, “Handbook of conformal mapping with computer aided visulization”, CRC Press (1995).

[8] J. Hagen, “Industrial catalysis: a practical approach”, Wiley-VCH, 2nd ed. (2006) chpt 5.

[9] D.E. Williams, K.F.E. Pratt, J. Chem. Soc., Faraday Trans., 92 (1996) 4497-4504. “Resolving combustible gas mixtures using gas sensitive resistors with arrays of electrodes.”

[10] D. Britz, ‘Digital simulation in electrochemistry’, Lect. Notes Phys. 666 Springer, Berlin Heidelberg (2005)

[11] W.H. Press, S.A. Teukolsky, W.T. Vetterling, B.P. Flannery, “Numerical recipes in C: the art of scientific computing”, Cambridge University Press (2002), chpt 4.2.

[12] M. Rudolph, J. Electroanal. Chem., 314 (1991) 13-22. “A fast implicit finite difference algorithm for the digital simulation of electrochemical processes.”

[13] M. Vilaseca, J. Coronas, A. Cirera, A. Cornet, J.R. Morante, J. Santamaria, Catalysis Today 82 (2003) 179-184. “Use of zeolite films to improve the selectivity of reactive gas sensors.”

Chapter 5: Correlation of results from diffusion models with experiment

(5.1) Introduction

In this chapter experimental results of sensor response are discussed, including for sensors of different microstructure, the response of zeolite-modified sensors and the response measured using electrodes with different separations. Both steady state and transient response, to a variety of gases, are considered. Experimental results, taken from several different sources, are presented for three different sensor materials. Chromium titanium oxide (CTO) is a p-type semiconducting material which is relatively insensitive to water and has good stability over long operating times. Tungsten trioxide (WO_3) and tin oxide (SnO_2) both are highly stable, n-type materials. SnO_2, whilst having a high sensitivity to humidity, is the most widely investigated and easily obtainable sensing metal oxide to date. The bulk of the work presented here was conducted as part of a joint experimental project funded by the EPSRC at University College London. The experimental data was collected by Ayo Afonja in the study carried out conjointly with the theoretical work and by Dominic Mann and Themis Paraskeva in previous experimental studies. Additionally, computational results were also compared with the work of M. Vilaseca et al. of the University of Zaragoza, funded by the DGICYT, Spain.

The aim of this chapter is firstly to demonstrate that these design and manufacturing issues can be successfully managed to enhance the variance of the sensor response and achieve discrimination, where it was simply not possible using the most basic device design. Secondly, we compare what has been concluded following the computational investigation to the experimental results and show that the enhanced discrimination can be understood in terms of the theory that has been presented in the course of this thesis.

(5.2) Response of CTO-SOLGEL sensors to fragrance molecules [1]

Two CTO powders of different microstructure were prepared, with a nominal composition $Cr_{1.95}Ti_{0.05}O_3$, using the sol-emulsion-gel method [2]. These are referred to as CTO-SOLGEL1, with an average particle size of 2μm, and CTO-SOLGEL2 with an average particle size of 0.7μm. The powders were screen printed onto alumina tiles supporting a gold electrode pattern which provided wide and narrow electrode spacing. The sensors where then tested with fragrance gases benzyl acetate, cineole, ethanol,

linalool and toluene. IUPAC names and molecular structures of these five molecules are given in table 5.1. Results for the steady state response on the different spacing are presented in figure 5.1.

Whilst both sensors have the same composition, their responses to a given gas are observed to be different in terms of the response magnitude and, in some cases, the magnitude and direction of difference in steady state response on the two electrode separations. This indicates that the concentration gradient that forms through the each of the devices, as a result of competitive diffusion and reaction of the gas, is different and that this is a consequence of the differences in microstructure of the two sensor preparations. It is observed also that this variation in response is gas dependent.

The smaller particle SOLGEL2 sensors have, for the most part, a lower response than the SOLGEL1 sensors. As one would presume that smaller particles will provide a larger surface area for gas interaction, apparently contrasting to what is observed, it is suggested that either the smaller particles here are more susceptible to sintering, resulting in a less accessible pore system than that of the larger particle size, or the gases react following some progressive reaction scheme. By this it is meant that there is an intermediate reaction stage for which the products have different sensitivity to the reactant and final products. If this were the case, an explanation for the observed behaviour would be that the SOLGEL2 system allows for the further stage of the reaction to be reached – a larger surface area for interaction of course is synonymous with a larger surface area for reaction (as discussed in chapter 3 with the eigenstate model).

By considering the difference in response obtained with the different electrode spacing, this matter can be resolved. The fact that for the SOLGEL2 sensors the difference in response with electrode spacing is of a similar or indeed larger magnitude (and in some instances in the opposite direction), indicates that the reaction is not occurring to a lesser extent over this sensor, since in this case the effect of changing the spacing would be reduced. This indeed illustrates the value of considering the response on different electrode spacing which enables a much more informed interpretation of the concentration profile through the device, which, as has been discussed, is gas dependent. Moreover, it provides, in essence, another route to discriminate within a sensor array.

It is proposed here that the large molecules, benzyl acetate, cineole and linalool, initially react to intermediate products with lower sensitivity than the initial reactant and then this product gas reacts to a more sensitive product. However, it is recognised that the reactant sensitivity is greater than the final product sensitivity. The reaction happens more quickly for benzyl acetate and linalool than with cineole – as indicated by the fact that cineole gives a greater response on the SOLGEL1 narrow gap in contrast to the other two. Following the discussion in chapter 4, this indicates a reaction to a less sensitive product i.e. cineole only reaches the first stage of the reaction scheme as is diffuses through the SOLGEL1 sensor. Cineole is in fact the smallest of the three molecules meaning that the sensor would appear to have a higher porosity for this molecule. As discussed in chapter 3, section 3.6.1, a lower effective rate may be observed for a higher porosity system as the fast diffusion associated with such a system results in the average time the molecule spends in the reactive region, and hence its likelihood of reacting, being reduced. However, the difference could be of chemical origin, simply being due to the gases having different surface decomposition rates.

The response patterns to ethanol and toluene are somewhat different. For ethanol the response is lower than the three aforementioned gases on both of the sensors. Moreover the response differences on the electrode geometries on the two sensors are very similar suggesting that just one reaction is occurring. It is proposed in fact that the intermediate product of the discussed reaction scheme is ethanol or similar.

Finally toluene gives a lower response on the SOLGEL1 sensor than on SOLGEL2 – this could be explained simply as being due to toluene having a lower sensitivity than the final product gas, assuming that it follows a reaction scheme of the same form.

Common name	IUPAC name	Structure
Benzyl acetate	Benzyl acetate	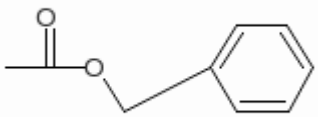
Cineole	1,3,3-trimethyl- 2-oxabicyclo[2,2,2]octane	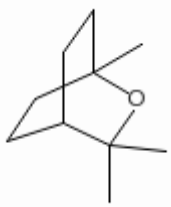

Ethanol	Ethanol	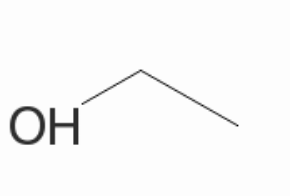
Linalool	3,7-dimethylocta-1,6-dien-3-ol	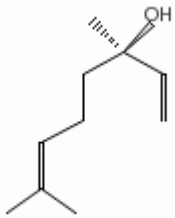
Toluene	Methylbenzene	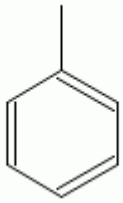

Table 5.1: IUPAC names and molecular structures of the tested fragrance molecules.

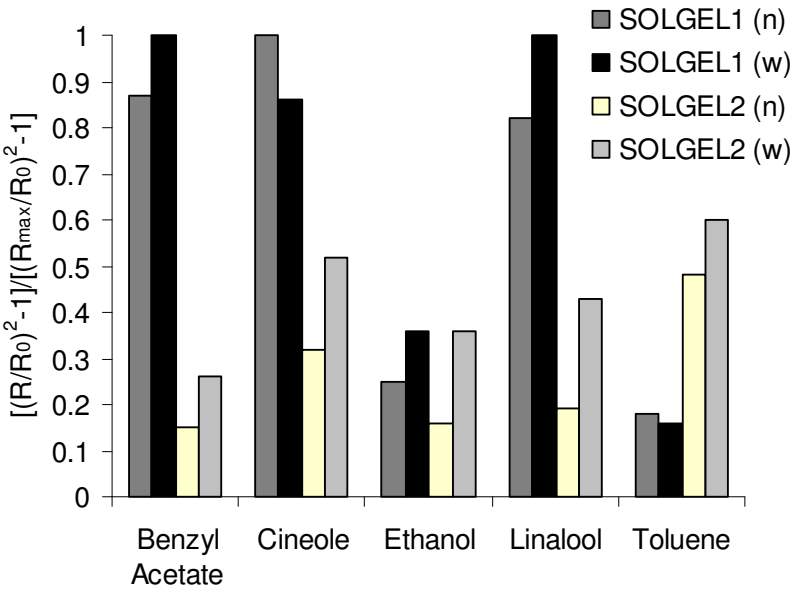

Figure 5.1: Relative amplitudes of response of CTO-SOLGEL sensors to different compounds testing at 400 °C on narrow (n) and wide (w) electrode spacing. Figure based on data taken from reference [1].

(5.3) Response of wide and narrow gap electrode sensors to alcohols and linear paraffins [3]

$Cr_{1.95}Ti_{0.05}O_3$ powder was prepared as described in [3]. The ink was screen printed using a DEK 1202 onto 2 x 2 mm alumina tiles with integral heater and a gold electrode pattern [4] that has both a narrow (40 µm) and a wide (160 µm) electrode gap – referred to as the SEMDEC electrode type pattern. This interrogates areas at the bottom and top of the CTO layer respectively to enable the determination of any gas concentration gradient evident within the material. Note the electrodes are not coplanar with the substrate, as is presumed in the models described in the previous section, but 10um above it. This is likely to result in greater confinement of the current within the narrow gap than predicted by the calculation; however, the assumption of coplanarity remains reasonable as the height is relatively small with respect to the gap between electrodes.

Zeolite Y was obtained from Zeolyst International in powder form and from this chromium exchanged zeolite Y (denoted Cr-Y-1) was prepared. The Cr-zeolite powders were also made into inks and applied on top of the CTO layer using the same process. 8 layers of CTO were printed down, to give a total thickness of 100±10 µm, followed by 4 or 8 layers of zeolite, giving zeolite layer thicknesses of 50±5 or 100±10 µm respectively. A control was also made which had no zeolite layer.
Zeolite bed GC/MS experiments were also carried out to ascertain the catalytic activity of the chromium exchanged zeolite Y [5]. The zeolite bed was housed in a tube furnace into which the analyte and carrier gas (dry air) were injected, the products then being transferred to a Markes Unity^{TM} thermal desorber via a heated transfer line. A Finnigan 4000 mass spectrometer was used to scan molecular weights in the range of 15-250amu.

Firstly, figure 5.2 shows the response on different electrode spacing of the control CTO sensor to alcohols of different chain length. Changing the electrode gap changes the response to all three alcohols, implying that there is a reaction occurring in all cases. As alcohols typically act as reducing agents and the response is greater on the wide gap electrodes, it is inferred following the discussion given in chapter 4, that the reaction gives a product to which the CTO is more sensitive than the alcohol (as CTO is a p-type material). There is no significant difference in response time on the two electrode gaps which indicates that the ratio of product sensitivity to reactant sensitivity is low and the rate constant is high (following figure 4.7(d)).

The order of sensitivity of the sensors to alcohols follows methanol > propanol > ethanol. Clearly there is some question of the greater sensitivity of propanol over ethanol. One explanation is that the product sensitivity increases with reactant chain length but that the small size of methanol (and its products) enables more effective transport through the sensor layer such that it gives the highest response (as shown in chapter 3, section 3.6.1 that diffusivity increases with effective porosity). Note the response has been linearised to remove the square root concentration dependence such that the transient response is instead directly proportional to the concentration [6].

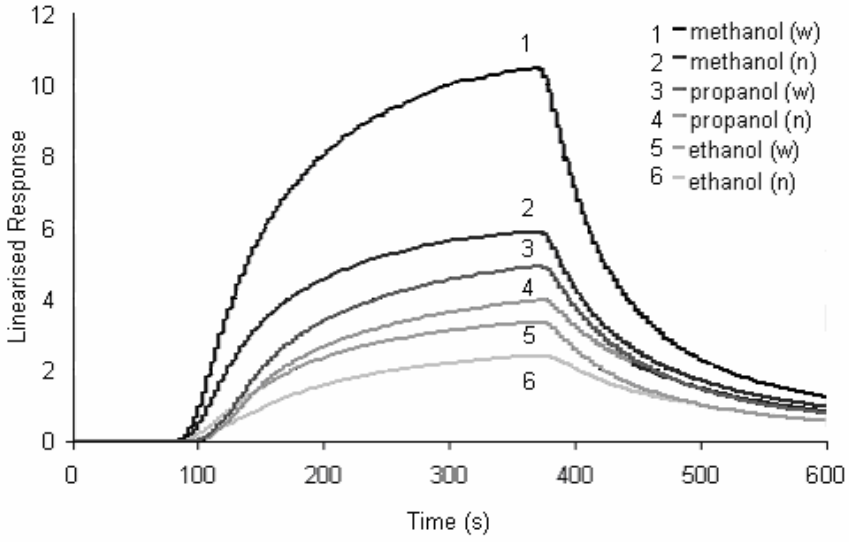

Figure 5.2: Linearised CTO response to alcohols. Sensor operating at 400°C. 300 s injection of analyte. (n) – narrow electrode gap, (w) – wide electrode gap. Figure taken from reference [3]

The sensitivity of CTO to alkanes, as shown in figure 5.3, decreases as the chain length increases following heptane > octane > nonane > decane. Little difference in response on the two electrodes is observed, the only appreciable difference being for heptane. What is noted here is that the response time increases with chain length, suggesting slower diffusion of longer chain molecules within the sensor layer (as was proposed for alkanes of different chain length in zeolites in chapter 2).

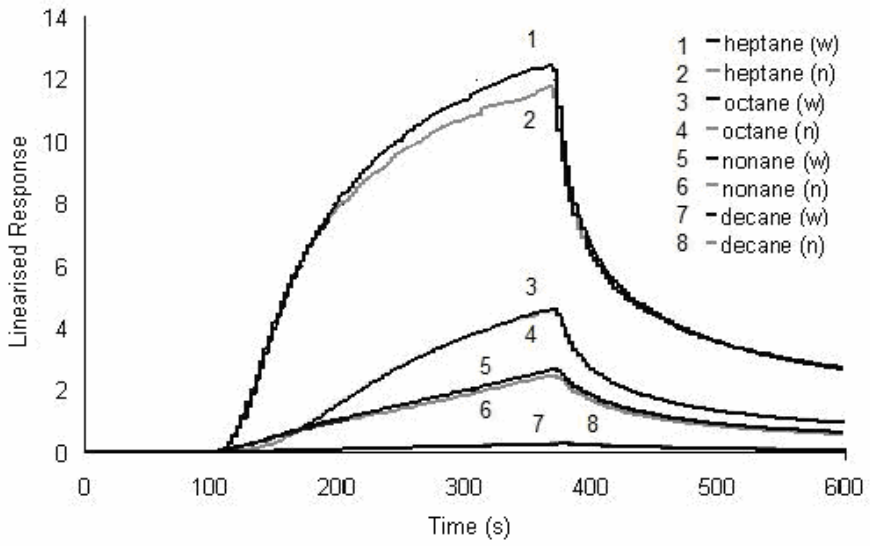

Figure 5.3: Linearised CTO response to alkane series. Sensor operating at 400°C. 300 s injection of analyte. Figure taken from reference [3]

Figures 5.4 and 5.5 show how the introduction of a zeolite layer can modify the response to alkanes, specifically here for octane and heptane on chromium exchanged zeolite Y (Cr-Y-1). From figure 5.4 for octane response, clearly a reaction is catalysed within the zeolite layer as the result of the introduction of the additional layer is to produce a difference in response on the different electrode spacing. However, some perhaps unexpected behaviour is observed in comparing the two different thicknesses of zeolite layer, as the thinner layer enhances the response yet the thicker layer diminishes it below that of the control sensor. In contrast, there is little difference on the two spacing and the response time between thick and thin zeolite overlayers.

We now consider in more detail results from GC/MS experiments performed to determine the catalytic activity of the Cr-Y-1, as summarised in table 5.2. Note CO_2, produced on full combustion, is likely to be present where water is observed but is not detected by the GC/MS. It is suggested that the primary analyte, octane, follows a progressive reaction scheme of cracking, rearrangement and finally combustion where a higher temperature (or longer diffusion length in the zeolite) enables further stages to be completed.

Temperature	Heptane	Octane
200 ^{o}C	Primary, water	Primary, pentane, butane/ methyl propane
300 ^{o}C	Primary	Primary, pentane, water, butane/ methyl propane
400 ^{o}C	Water	Primary , water

Table 5.2: Reaction products of heptane and octane with chromium exchanged zeolite Y (Cr-Y-1) from GC/MS zeolite bed at different temperatures. Products are listed in order of decreasing abundance. Based on data taken from reference [3].

From figure 5.3 it is suggested that shorter chain alkanes will give a difference in response on different electrode separations and have a higher sensitivity associated with them than longer chain molecules. For the shorter thickness of zeolite only the first stage (200^{o}C) reaction occurs and observed is an enhanced response with the wide gap spacing giving a higher response than the narrow gap. For the longer zeolite length, more of the primary analyte reacts but this leads to products to which the sensor is less sensitive, such as octane, so the overall response is reduced. Shorter chain alkanes are still being produced such that the different electrode spacings still give the same difference in response.

It should be noted that the invariant response time is not as predicted from the model presented in chapter 4, which is most likely due to the assumption in the latter, of the diffusion-reaction finite difference model where the reactant and product diffuse at the same rate. In reality the products from the zeolite (which we expect to be smaller) may diffuse much more quickly through the sensor than the analyte gas.

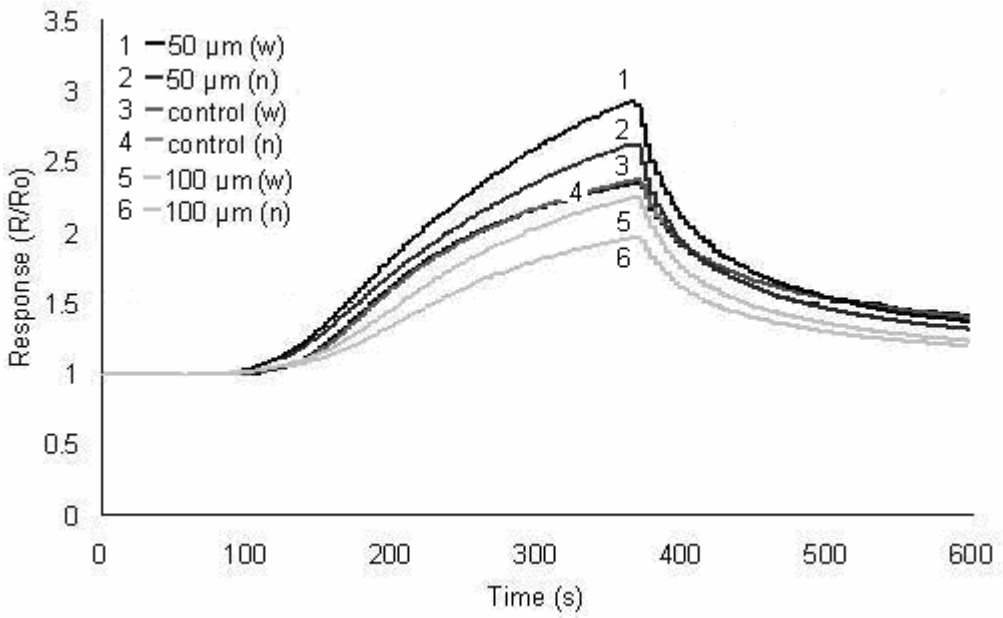

Figure 5.4: Octane response transients for Cr-Y-1 sensor array (control – CTO, 50 µm Cr-Y-1 layer on CTO, 100 µm layer on CTO) operating at 400°C. Figure taken from reference [3]

Figure 5.5 gives the response for the sensor with zeolite overlayer to heptane and octane. The response of the zeolite sensors has been normalised to the control sensor response as a reference sensor. In the case of heptane, the inclusion of both thicknesses of the zeolite layer leads to an enhanced response compared to the control with heptane as does the 50 µm layer with octane. The behaviour of octane through the different thicknesses of zeolite over-layer has been discussed above. Referring to the GC/MS results given in table 5.2, heptane does not actually appear to be reacting within the zeolite until 400°C at which point the presence of water would suggest that full combustion is occurring, the products of which CTO is not sensitive to. However, clearly this is not the case with the response being greatly enhanced, indicative of the presence of cracking products to which the GC/MS is not sensitive, such as methane.

There are also clear variations in the transient shapes, for example the initial peak in the transient between 100 and 200s for both heptane and octane. This is likely to be due to an abrupt initial influx of the primary analyte and of CTO sensitive reaction products such as methyl-propane, butane and methane at the sensing layer.

Even for these few experiments it is clear from these experiments that factors such as layer thickness and measurement time are crucial to successful sensor design.

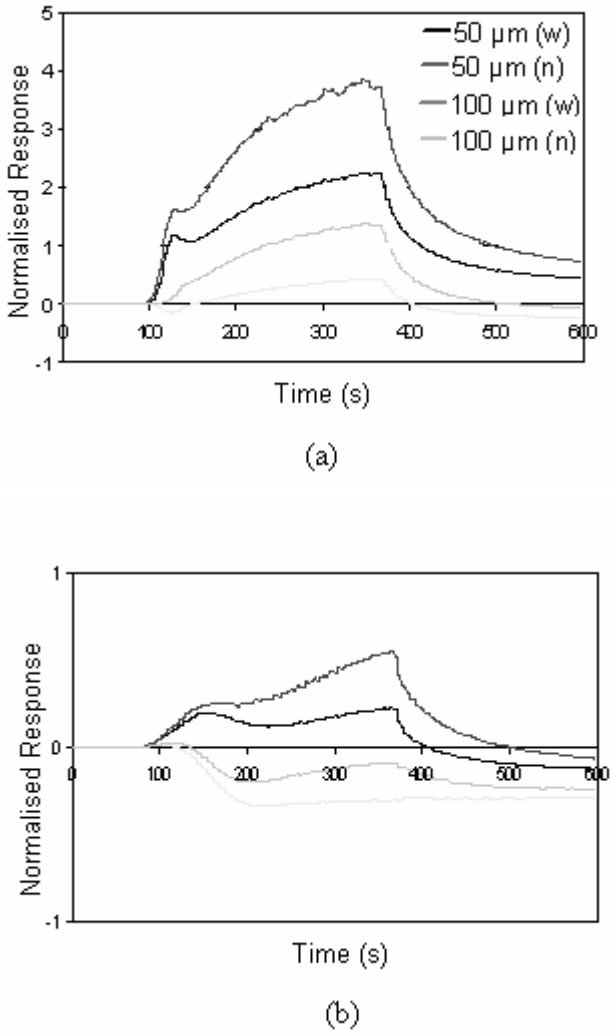

Figure 5.5: Comparison of (a) heptane and (b) octane normalised responses for Cr-zeolite Y-1 sensors operating at 400°C in the injection rig. 500 s sample injection. Figure taken from reference [3]

(5.4) Response of single electrode, zeolite-modified sensors to ethanol and carbon monoxide

Figures 5.6 and 5.7 present experimental data of n-type WO_3 and p-type CTO transient responses to carbon monoxide and ethanol [7]. The sensors consist of screen-printed layers with a total thickness of 50µm and the response was measured using a single electrode spacing. Response transients are also given for two zeolite-modified sensors, with overlays of the acidic zeolites H-A (exhibiting LTA structure) and H-ZSM-5 (exhibiting MFI structure).

In this case, the sensor response is simply referred to as an increase in response, *G*, where *G* may be a fractional increase in resistance or conductance. CTO and WO_3 give opposite responses in this respect, due to their different n- or p-type character. The response of CTO to CO is quicker than that of WO_3, whilst they have similar response times to ethanol. Considering the difference in response time to CO, it is understood that either some reaction is occurring or diffusion occurs more easily through the CTO layer (or a combination of both). Materials characterisation performed using a scanning electron microscope (SEM) shows that CTO has a more open microstructure than WO_3 [7].

The response of WO_3 to ethanol is faster than for CO whereas it is slightly slower for CTO – this can be correlated to what is observed for figure 5.2 where the alcohol is concluded to react to a more sensitive product in CTO. Because of the different n- and p-type characters of the two metal oxides, it is expected that WO_3 is less sensitive than to the product than the reactant. In figure 4.8 we see that the diffusion-reaction model predicts that there will result in a slower response for a sensitive product and a faster response for an insensitive product. That there is less of a difference in the CTO response times is not unexpected bearing in mind its more open microstructure (the effective rate constant expected to be lower for higher porosity systems).

A summary of the zeolite-modified sensor response is given in table 5.3; both gases clearly react in both of the zeolites as revealed by the difference in steady state response on addition of the zeolite layer. Here the two zeolites modify the response in the same way for each sensor-gas case but the H-A overlayer is seen to have a greater effect than the H-ZSM-5 overlayer. This result correlates to what was observed in figure 3.16(a) where, if the gas diffuses faster in the macro-porous phase than in the zeolite framework, the effective rate constant increases with decreasing porosity. It is noted from the SEM characterisation that the H-A particle size is roughly twice that of the H-ZSM-5 and they form a lower porosity system.

Considering table 5.3, it is proposed that CO reacts within the zeolites to a product that both sensor materials are less sensitive to. As has been discussed previously, the product must diffuse more quickly than the reactant in the sensor because otherwise the zeolite would be expected to increase the time of response. Ethanol on the other hand, reacts to a product to which the metal oxides have contrasting sensitivity - most likely arising from their different n- or p-type characters; it is likely in fact that the zeolite

promotes the reaction proposed to be occurring within the sensor layer. The ethanol/H-A/CTO response is significantly enhanced and the response time is also increased. The ethanol/H-A/WO_3 response time is also increased (though to a lesser extent), in agreement with what is predicted from our discussion in chapter 4.

The responses to ethanol of the two sensors are now significantly different, both in terms of steady state response and response time, demonstrating the usefulness of including the zeolite layer.

Sensor material	**Gas**	**Response modifications with zeolite overlayer**	
		Steady state response	**Response time**
CTO	CO	Diminished	No change
WO_3	CO	Diminished	No change
CTO	Ethanol	Enhanced	Increased
WO_3	Ethanol	Diminished	Increased

Table 5.3: Summary of response changes with different zeolite layers for CTO and WO_3 sensors with CO and ethanol.

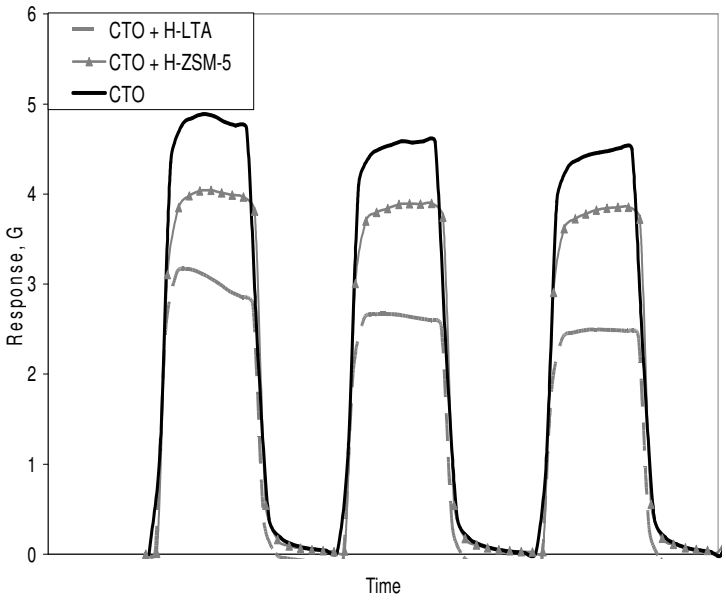

(a)

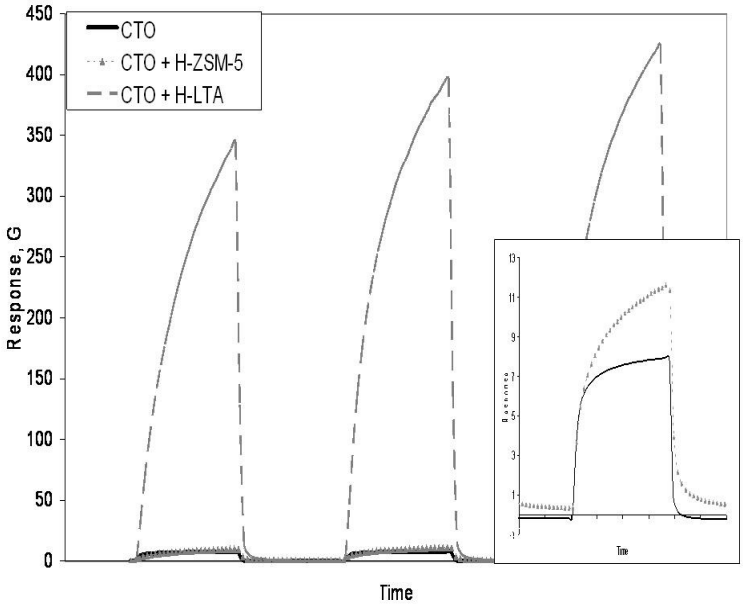

(b)

Figure 5.6: The gas response of CTO sensors to 30 minute exposures of (a) 2000 ppm carbon monoxide in dry air and (b) 28 ppm ethanol in dry air. The inset shows magnified data for CTO and CTO + H-ZSM-5 sensors.

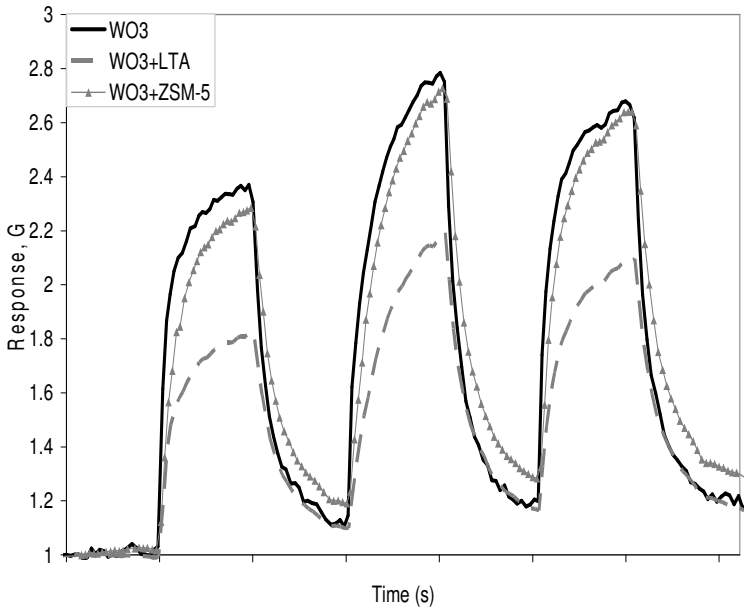

(a)

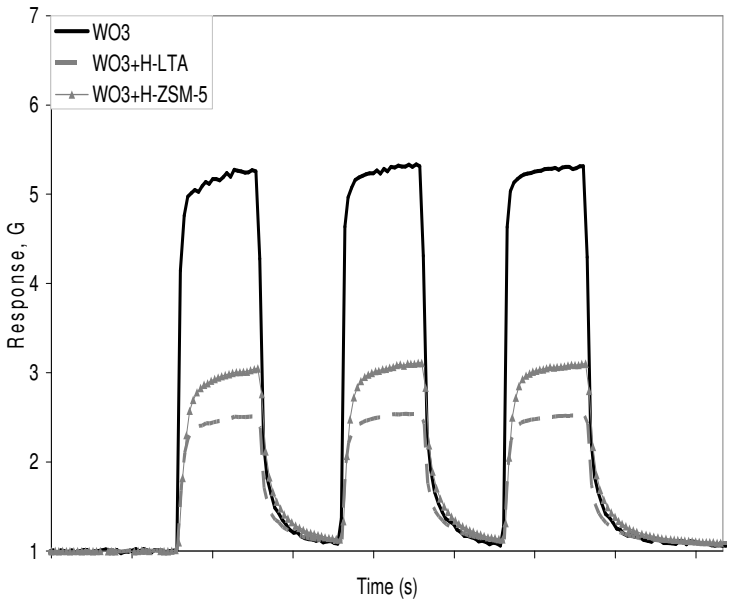

(b)

Figure 5.7: The gas response of WO_3 sensors to 30 minute exposures of (a) 2000 ppm carbon monoxide in dry air (b) 21 ppm ethanol in dry air. Figure taken from reference [7].

(5.5) Response of zeolite-modified sensors to methane and ethanol [8]

Here zeolite modified Pd-doped SnO_2 sensors have been used to detect methane and ethanol. Two over-layers are considered; siliceous MFI (silicalite) and LTA (NaA) – SEM images in [8] are presented to show that MFI has a more open microstructure than LTA. The SnO_2 sensors were again prepared by the method of screen printing and the zeolites were then hydrothermally synthesised upon the SnO_2 layer following *in situ*

seeding of the sensor surface. Response transients for control and zeolite-modified sensors are presented here as figure 5.8.

The response to methane is reduced, compared to that of the control, with the addition of either zeolite layer and is eliminated completely with zeolite LTA. The ethanol steady state response is not greatly changed, although the response time is somewhat increased. The proposed reasoning for these results is that ethanol absorbs strongly within the zeolite such that the gas transports effectively through the layer whereas methane does not. The SEM images show that the zeolite layers are of low porosity (large zeolite volume), hence the need for sufficient absorption of the gas into the zeolite phase for effective transport according with what has been discussed in the course of chapter 3. In [9] absorption rates are calculated for these two gases in zeolite Mordenite confirming that ethanol, at least in this case, absorbs more strongly than methane.

That there is a difference in the responses to methane with the different zeolites could originate from methane absorbing more strongly into MFI compared to LTA. The former is in a siliceous form and would hence be expected to preferentially adsorb non-polar molecules such as methane over polar molecules such a ethanol (see calculated dipole moments, chapter 2). The converse is expected of energetically heterogeneous LTA (NaA). Additionally, however, the observed behaviour may be a consequence of the more open microstructure of MFI which is suggested from the SEM images. With a greater pore fraction, the transport of methane through the layer is more viable. It is likely that in fact a combination of these different effects is being observed. Clearly for the distinction of these two gases, LTA in the form used here would be a more suitable choice that MFI.

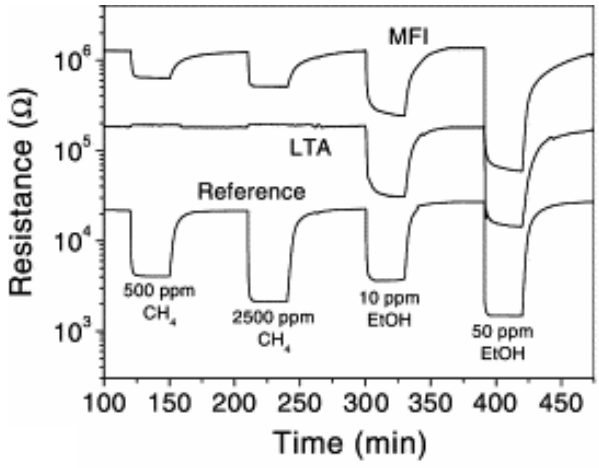

Figure 5.8: Sensor resistance as a function of the nature (methane or ethanol) and concentration of the organic compound. Testing at 350 °C and with 0% of relative humidity in the feed, for the reference (unmodified) sensor and for sensors modified with silicalite and zeolite A layers. Figure taken from reference [8].

(5.6) Conclusions

It is concluded that experimental results of sensor response validate the use of both zeolite-modification and variable electrode spacing as highly valuable methods of enhancing the discriminating potential of metal oxide gas sensors. Also validated is the relevance of the theory of gas transport and reaction, on different spatial scales, in understanding the success of these methods in sensor design.

As was proposed in chapter 3, the microstructure of the sensing metal oxide impacts the response observed, particularly where the gas reacts within the sensing layer. It has been shown how the responses of sensors of different microstructures can be compared and collated to build an identifying representation of the test gas – and this is due to the gas-specific balance between diffusion and reaction being altered on changing the microstructure. It is demonstrated that this behaviour is indicative of a variable concentration profile which, as was discussed in chapter 4, can be probed using different electrode spacing adding further dimensions to the representation of response. Using the four responses associated with different electrode spacing on two sensors of different microstructure, as in figure 5.1, offers a robust discriminatory tool for distinguishing between the gases considered.

Again, considering the zeolite layer, the experimental results agree with those hypothesised from chapter 3 in terms of the importance of details of the microstructure such as the porosity, as well how favourably a gas will absorb into the zeolite and how quickly it diffuses within it. For example, figure 5.8 shows how the choice of zeolite based on the absorptive properties and the porosity can be tuned to achieve maximum selectivity. Though clearly, as is evident from section 5.2.3, the use of a zeolite element may be largely determined by what reaction it catalyses – i.e. whether the product is more or less sensitive, with respect to the sensor, than the reactant. Understanding the reaction schemes occurring both in the zeolite and the sensor layer, has been shown to be very important to understanding the patterns in response observed, especially if the reaction consists of different stages in which case the device length and microstructure (and the operating temperature) may determine what stage is achieved.

The zeolite response times are observed experimentally, in section 5.2.2 and in part in section 5.2.3, to be faster than one would anticipate following the results presented in chapter 4. However, as was discussed in chapter 4, this is due to the fact the product and reactant diffusivities are assumed to be the same in the model whereas in reality the zeolite is catalysing a reaction in which the products move much more quickly through the sensor than the reactant. Note it was also stated in chapter 4 that the response time, at least where the rate constant in the zeolite is high, is not in fact the most instructive response parameter. Clearly the reaction scheme modelled in chapter 4 is also an oversimplification, yet despite this, and perhaps in part as a result of this, the model does provide a comprehensive foundation on which to reason the observed experimental behaviour.

On the whole good correlation has been observed between experiment and theory and clearly the diffusion and reaction of gas does underpin an understanding of the observations. The next question, of course, is can we use the theoretical basis developed to predict successful sensor design?

References

[1] T.C. Paraskeva, “Improving the performance of sensor for electronic noses using zeolites as selectivity modifiers”, Ph.D. thesis, University College London, 2004.

[2] G. Chabanis, I.P. Parkin, D.E. Williams, J. Mater. Chem., 11 (2001) 1651-1655. “Microspheres of the gas sensor material $Cr_{2-x}Ti_xO_3$ prepared by the sol–emulsion–gel route.”

[3] D.P. Mann, “Zeolite modified metal oxides for gas sensing”, Ph.D. thesis, University College London, 2005.

[4] D.E. Williams, Sens. Acuators B, 57 (1999) 1-16. “Semiconducting oxides as gas-sensitive resistors.”

[5] D. P. Mann, K. F. E. Pratt, T. Paraskeva, I. P. Parkin, D. E. Williams, IEEE Sensors journal, 7 (2007) 551-556. “Transition Metal Exchanged Zeolite Layers for Selectivity Enhancement of Metal-Oxide Semiconductor Gas Sensors.”

[6] D E Williams, K F E Pratt, J. Chem. Soc., Faraday Trans, 92 (1996) 4497-4504. “Resolving combustible gas-mixtures using gas sensitive resistors with arrays of electrodes.”

[7] R. Binions, H. Davies, A. Afonja, S. Dungey, D.W. Lewis, D.E. Williams, I.P. Parkin 156 (2009) J46-J51. “Zeolite modified discriminating gas sensors.”

[8] M. Vilaseca, J. Coronas, A. Cirera, A. Cornet, J.R. Morante, J. Santamaria, Catalysis Today 82 (2003) 179-185. “Use of zeolite films to improve the selectivity of reactive gas sensors.”

[9] O. Hugon, M. Sauvan, P. Benech, C. Pijolat, F. Lefebvre. Sens. Actuators B, 67 (2000) 235-243. “Gas separation with a zeolite filter, application to the selectivity enhancement of chemical sensors.”

Chapter 6: Conclusions and future directions

The chief objective of the work presented here was to demonstrate the use of modelling to aid the design of zeolite-modified gas sensors with the aim of improving selectivity and, in particular, to show that through understanding how the gas diffuses and reacts within the porous layers, and how this depends on different properties of the system, enhanced discrimination to different gases can be achieved. The basic sensor design is a layer of semiconducting metal oxide, at the base of which electrodes are positioned and on top of which a macroporous zeolite layer is overlaid, the zeolite crystallites themselves being microporous.

In the first part of the investigation, chapter 2, it was considered specifically how the microporous zeolite structure selectively interacts with different gases based on shape and size correlations between the molecule and the zeolite framework. For example, a somewhat trivial finding was that long chain molecules will adsorb more strongly than shorter molecules due to the increased number of framework-sorbate interactions associated with the larger molecule. It was also shown how the binding strength of hydrocarbons containing the same number of carbon atoms, increased as more linear molecules are considered as the average distance between zeolite and sorbate is reduced, an effect most prominent in zeolite frameworks containing channel structures. For small molecules (and large molecules with similar size and shape) with different functional groups, no significant difference was observed in their patterns of binding energy within different zeolite frameworks. Higher level, density functional theory (DFT) calculations were performed with an aim of determining whether the presence of ions may result in greater variation between these molecules. Whilst the fact that more polar molecules should absorb more favourably than non-polar molecules was confirmed, the simple cluster model did not offer any reliable insight into the role of the zeolite framework in this process. Additionally it was discussed that developing the calculation by using more complex clusters or embedding a cluster within a periodic system is not necessarily worthwhile, considering the highly involved process of sensor response, and hence it was concluded that these types are calculation are not well suited to this application. The restriction of focussing solely on the zeolite internal pore structure was apparent also on comparison of the force-field results with experimental response data. Whilst, on the whole, an explanation of the experimental results could be

derived from the force-field results or the other descriptors discussed. However, this involved employing different interpretations of the calculated adsorption strengths: strong adsorption was indicative sometimes of slow diffusion and in other cases of fast diffusion and in some instances, comparison of the different data sets simply highlighted that another process, namely a reaction, was dominating the response behaviour, where relative sensitivities of the sensor material to reactants and products becomes highly important. It is hence concluded that, whilst selective adsorption in zeolites certainly is crucial to their use in gas sensing, these calculations can not be used, by themselves, as a predictive tool for sensor design.

In chapter 3, the dimensions of the simulated system are increased with the development of a model representing penetrable crystallites of the zeolite compound which themselves form a confining environment. The gas may transport through the system either through the large pores or by entering the zeolite phase and passing through the micropores. The price paid for the simulation of a larger system size is the loss of the atomistic detail – the zeolite framework is now represented as a homogeneous phase and values are input for the partitioning of gas between the zeolite and pore phase, diffusion coefficients for the two phases and also a rate constant (as a reaction may now be catalysed within the zeolite phase). The effective bulk diffusion coefficient and rate constant of an ideal, periodic zeolite layer can be calculated as a function of the aforementioned parameters as well as of the microstructure. The method of finding bulk properties is also applied to a model sensor system for which the reaction is considered to occur at the surface of impenetrable solid particles.
What is observed is that for these systems is that where a reaction occurs, there is a delicate balance between diffusion of gas and its decomposition. As the rate constant increases, the effective rate constant increases, as one would expect, and the effective diffusivity generally decreases. The extent of this variation, however, in turn varies with the microstructural properties such as the porosity, and the other input properties such that it is the case that with one confining microstructure, two different gases (as defined by partition coefficient and diffusivities) will have very similar effective properties whereas with another these will be very different. It is demonstrated how the microstructure can be optimised to give a maximum difference in the effective properties between different gases. What is still overlooked here though, and is essential to providing a relevant understanding of the behaviour discussed, is an

interpretation of the effective properties in terms of the sensor response. Without understanding the relative sensitivities of products and reactants and also accounting for the macroscopic geometry, which determines over what distance the gas will competitively diffuse and react, the results here are ambiguous.

Representation of the sensor response is tackled in chapter 4 and the importance of the diffusion-reaction balance is here exemplified. The calculation proceeds by finding the concentration through two adjacent, macroscopically homogeneous layers, taking the effective diffusivity and rate constant as inputs. A dipole type field is applied to the model sensor layer and the interaction of this and the concentration is calculated to give a simple representation of sensor response. A concentration gradient forms within the device due to the simultaneous diffusion and reaction of gas and by varying the electrode spacing, the penetration depth of the electric field can be controlled offering a means to probe the concentration profile and infer the diffusion-reaction characteristics. It is discussed how rather than looking just at one aspect of response, considering the steady state response, the transient response and responses on different electrode spacing, offers a much more robust analytical technique.
Of course, as was pointed out in chapter 4, there will be instances where distinction, even when using a well considered electrode pattern, is simply not achievable. Here further engineering of the sensor layer could be used to modify the diffusion-reaction parameters as was discussed in chapter 3. Alternatively a zeolite transformation layer can be included where again, the diffusion-reaction properties are key both in terms of the zeolite as a separate entity, where, similarly to the sensor layer, concentration gradients develop due to the gas-dependent balance of the different processes, and in terms of the combined zeolite-sensor composite system, i.e. the composite device will itself have an effective diffusivity and rate constant. This point is demonstrated in chapter 4 with the observation that the steady state response as well as the transient response to a gas which reacts in the sensor layer is affected with the inclusion of zeolite layer, even when the gas does not react in the zeolite.

From what has been discussed, the importance of diffusion and reaction to selective sensor response appears undeniable. On comparison with experiment, both the validity of this conclusion, and therefore the worth of the models presented are demonstrated – although more systematic experimental investigation is needed to verify the correlation

further, particularly in considering the microstructure of the two layers. Of course the real test of the work presented here is to ascertain whether such simulation could be used to predict a successful sensor design. If we were to turn around the examples given in chapter 5 and ask whether it would have been possible to predict the occurring distinctions then, following the discussion of chapter 5, the outcome is on the whole assuring, providing sufficient information about the gas and microstructures are known. However, aspects overlooked in the model, in particular of the diffusion-reaction behaviour, but which have a bearing on the sensor response, are identified. The difference of product and reactant diffusivities is expected to be important in predicting more accurately the response time variations and the occurrence of reactions following multistage reaction schemes will obviously complicate the response patterns observed, although at least the occurrence of these anomalies could be identified.

That some prior knowledge is required of the gases between which we wish to discriminate is a point worth discussing further. In chapters 3 and 4, knowledge is assumed of the gas diffusivity and its adsorption in the zeolite as well as the rate constant. However, it has been implied that these properties are somewhat difficult to obtain with accuracy. What is integral to the larger scale model though, is that the actual system is less sensitive to the fine atomistic detail. For example, one could vary the partition coefficient by say 10% or more without significantly changing the outcome – especially if the two gases had highly contrasting diffusivities. Essentially, we can work with a less exacting idea of these properties, it being possible to extract the specific identity of a gas from a known set – where in fact the gases in the set are *known* initially in terms of a more heuristic sense. For example, we could have predicted the ethanol/methane result (section 5.2.4), given the insight into the zeolite microstructures used, based simply on the dipole moments (see table 2.2) of the test gases. What will be key is to have an idea of the different reaction schemes and reactant and product sensitivities.

In considering how one might wish to extend the work presented here, to further an understanding of sensor response dependence on diffusion and reaction and the use of zeolite layers to enhance selectivity in terms of modelling, one could propose the development of a more complex model reaction scheme involving more gas species or better representations of the different diffusivities. Additionally, we could look further

at the properties of the microstructure, at more complex geometries (as is possible with the eigenstate model) or at random rather than periodic media. However, before following such approaches the representation of other aspects of the sensor response, in particular the relation of the local conductivity to the gas concentration and the dependency of charge transfer on the microstructure, should be considered. In the work presented here, these features have been represented very simply and hence there is a question of whether improving the diffusion-reaction model will be worthwhile without paying further heed to the conduction issues? To be assured of the reliability of a more complex diffusion-reaction model, the next step in model development must be the assessment of the sensitivity of the different aspects of response. Many approaches have been taken to understanding these issues, as was discussed in chapter 1, giving vital insight into this complex field, but this said there is certainly more to be done. It is noted that diffusion and conduction are considered to be analogous transport processes – hence there is the potential to use the eigenstate model to find the conductivity of a porous system.

More generally in terms of zeolite modified gas sensors, catalytic analysis of gases in both zeolites and metal oxides would clearly be advantageous following the discussion here. Whilst zeolites have been the subject of many such studies, these have typically been carried under inappropriate conditions. Additionally, the importance and worth of exploiting the multidimensional nature of response has been demonstrated. This is in keeping with the use of sensor arrays and the concept of the electronic nose as was introduced in chapter 1. There is no doubt that the ongoing development of the e-nose design and response analysis will be central in the progress of gas sensing.

As a final thought, it is interesting to reflect on the place of computational modelling in a predominantly practically focussed research field, such as this. What has certainly been confirmed is the complexity of the sensor systems at hand. One might, therefore, expect that due to the unavoidable simplifications and assumptions made in developing a workable theoretical model that any such model will be too far from the real situation to be of benefit. However, the value of the theoretical premise is the ability to isolate aspects of the system behaviour, such as the dependency of response on gas transport or the dependency of gas transport on the confining environment, from the backdrop of a highly complex set of variables, in a manner which is simply not possible through experiment. Comparison with experiment is an essential process in order to either

confirm the importance of certain parameters or, if there is a lack of correlation, to highlight the hierarchy of sensitivities to the different processes of the final outcome and thus help to direct future studies.

Whilst it may be unlikely that successful gas sensor design may be achieved purely using theoretical methods, I believe that through the course of the investigation here, it has been demonstrated that modelling will play a crucial role in gas sensor development and will be essential in to efficient and accurate sensor design in the future.